Preparation and Characterization of Liquid Phase Exfoliated MoS$_2$ Nanosheets

by

Yushi Wei

A thesis submitted in partial fulfillment of the requirements for the degree of

Master of Science

in

Chemical Engineering

Department of Chemical and Materials Engineering

University of Alberta

Abstract

In this study, natural molybdenite mineral was exfoliated into nanosheets in organic solvents and co-solvent of 2-propanol/water with the ultimate goal to use the nanosheets as catalysts for water splitting. The exfoliated nanosheets were characterized with a variety of techniques such as UV-visible spectroscopy, SEM, EDX, TEM, AFM and XRD. Characterization of the exfoliated nanosheets showed that the nanosheets consisted predominantly of few layers and monolayer. The performance of the exfoliated nanosheets for hydrogen production were investigated through the cathodic reduction reaction in water splitting, otherwise known as hydrogen evolution reaction. A potentiostat was used to control and measure the voltage difference between the working electrode (samples immobilized on glassy carbon) and the reference electrode.

Due to the nature of the natural mineral used (97% purity by weight), high concentrations of impurities were observed in the co-solvent exfoliated nanosheets after processing. With that said, there was still noticeable improvement in the electrochemistry performance of the co-solvent exfoliated nanosheets compared to the unexfoliated material. On the contrary, the organic solvent NMP exfoliated nanosheets did not exhibit any noticeable increase in catalyst performance compared to the unexfoliated material. In addition to the noticeable increased performance in the col-solvent exfoliated nanosheets, co-solvent is advantageous to organic solvent due to low boiling point (easily evaporated), high exfoliation yield, and relative environmental friendliness compared to organic solvent. In this study, it is the first time empirical findings were used to assess the performance of co-solvent exfoliated nanosheets.

"If you're not failing, you're not pushing your limits, and if you're not not pushing

your limits, you're not maximizing your potential."

– Ray Dalio, Principles: Life and Work

Acknowledgements

Table of Contents

List of Tables

List of Figures

List of Symbols

H_{ad}	Adsorbed hydrogen
ΔG_{mix}	Change in Gibbs free energy due to mixing
ΔH_{mix}	Change in Enthalpy due to mixing
ΔS_{mix}	Change in Entropy due to mixing
T_{flake}	Thickness of dispersed flake
V_{mix}	Total volume of the mixture
φ	Volume fraction of dispersed flake
δ_m	Square root of the surface energies of dispersed flake
δ_v	Square root of the surface energies of solvent
γ_{SL}	Interfacial energy for solid-liquid
γ_{SG}	Interfacial energy for solid-gas
γ_{LG}	Interfacial energy for liquid-gas
θ_c	Equilibrium contact angle
Y_s	Surface tension
E_s	Surface energy
T	Temperature
S_s	Surface entropy
E	Energy
h	Planck's constant
f	Frequency
A	Measured absorbance
ε	Molar absorptivity constant
l	Path Length
c	Concentration of the solution

I_o	Intensity of the reference beam
I	Intensity of the sample beam
d	Characteristic spacing
n	Integral value
n	Incident wavelength
θ	Angle between lattice planes and the incident x-rays (Bragg angle)
ΔE_p	Difference between the forward and reverse peaks on the potential axis
D	Average grain size
k	Shape factor constant depending on the shape of the crystallite
β	Full width half maximum
η	Overpotential
a	Tafel slope
j	Current density
j_o	Exchange current density

List of Abbreviations

2H	Semiconducting trigonal prismatic
1T	Metallic octahedral
HER	Hydrogen Evolution Reaction
DFT	Density Functional Theory
TMD	Transition Metal Dichalcogenides
LPE	Liquid Phase Exfoliation
HSP	Hansen Solubility Parameter
XRD	X-Ray Diffraction
STM	Scanning Tunneling Microscopy
DI	Deionized Water
IPA	2-Propanol (Isopropanol)
RCF	Relative Centrifugal Force
CHP	N-cyclohexyl-2-pyrrolidone
NMP	N-methyl-2-pyrrolidone
N12P	N-dodecyl-2-pyrrolidone
N8P	N-octyl-pyrrolidone
BP	Ultrasonic Bath and Probe
TEM	Transmission Electron Microscopy
HRTEM	High-Resolution Transmission Electron Microscopy
UV-Vis	Ultraviolet-Visible Spectrophotometry
SEM	Scanning Electron Microscopy
EDX	Energy Dispersive X-ray Analyzer
AFM	Atomic Force Microscopy
PID	Proportional-Integral-Derivative

RHE	Reversible Hydrogen Electrode
RDE	Rotating Disk Electrode
LSV	Linear Sweep Voltammetry
GCE	Glassy Carbon Electrode
CV	Cyclic Voltammetry
SAED	Selected Area Electron Diffraction

Chapter 1 Introduction

1.1   Importance of Hydrogen

Hydrogen with atomic number 1, is the most abundant chemical element in the universe in its monatomic form (H)[1]. Hydrogen could be found in everyday chemical compounds such as water and hydrocarbons. However, diatomic hydrogen otherwise known as hydrogen gas (H_2) does not occur naturally in nature. Thus, processing of existing chemical compounds is required to obtain H_2 that then could be used for various applications as shown in Figure 1.1. Hydrogen is attractive as an alternative energy source to fossil fuel due to water being the only by-product during combustion with pure oxygen. It is the fuel of choice in the space industry due to its fundamental property in producing the highest combustion energy release per unit weight while simultaneously yielding the highest specific impulse – a measure of efficiency in relation to amount of propellant consumed[2]. Nitrogen oxide (NO_x) emission is commonly associated with smog, acid rain and formation of fine particles. Under certain conditions, addition of hydrogen as an additional fuel in a compression ignition engine resulted in lower NOx emission while enhancing engine power, torque compared to using diesel by itself[3]. Hydrogen peroxide, commonly used for disinfection, sterilization or preservation is made through catalysis of hydrogen and oxygen. In the upgrading of bitumen, hydrogen is used in the hydrocracker to convert bitumen into high quality crude oil. The list goes on with an ever growing list of applications for hydrogen.
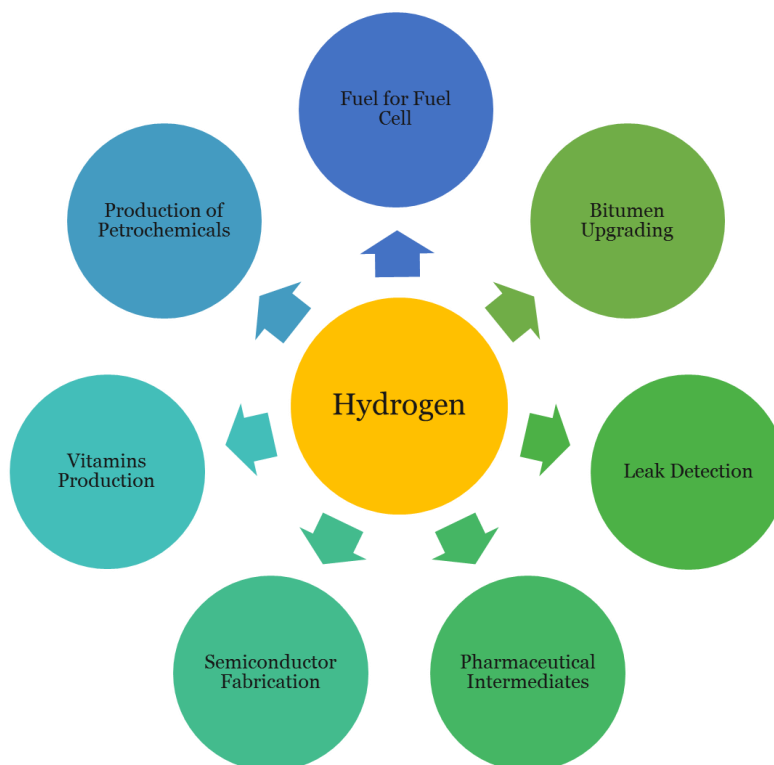
Figure 1.1 Various applications of hydrogen[1,4,5]

1.2   Steam Methane Reforming

On a commercial scale, the production of hydrogen is achieved using steam methane reforming, where methane reacts with water in a series of reactions to produce carbon dioxide and hydrogen as the final products[5].

$$CH_4 + H_2O \rightarrow CO + 3\ H_2 \tag{1-1}$$

$$CO + H_2O \rightarrow CO_2 + H_2 \tag{1-2}$$

On the commercial scale, steam methane reforming is the most economical method to produce hydrogen. However, there are severe drawbacks that may hinder the use of the as-produced hydrogen in applications that require zero or small amount of impurities. In steam methane reforming, carbon monoxide is commonly produced as by-product and trace amounts of it can exist even after the water gas shift reaction. Carbon monoxide can "poison" delicate catalysts that

are used in the manufacture of semiconductor or fuel cells by chemical bonding to the active sites which then renders the catalyst ineffective[6]. In addition, trace amounts of heavy metals are present in natural gas that will invariably carry over to the methane used for steam reforming. Even though the final concentration of hydrogen may be very close to 100%, but there may very well be trace amount of metals present that may affect the potential applications of produced hydrogen. That brings us to catalysis of water, where water is split into hydrogen and oxygen.

1.3   Hydrogen Production via Water Splitting

Production of hydrogen is possible via either electrochemical means or photocatalysis. Water splitting is attractive due to its "zero" emission status when green energy is used to as the fuel source. The products of water splitting are hydrogen and oxygen, without any additional emission, which makes it very attractive in our quest for a greener planet. Additionally, catalysis of water is the method of choice in space exploration due to the need to recycle human waste while providing sufficient oxygen for breathing. That is another topic for now, as the objective of this thesis is the production of hydrogen.

1.3.1   Photocatalysis

In the simplest term, photocatalysis water splitting is the production of hydrogen and oxygen from a photoactive suspension (photocatalysts suspended in water) upon illumination. Semiconductors with suitable band gap are desired with the minimum theoretical band gap for water splitting at 1.23V at pH = 0, which is also equivalent to 1008 nm[7]. The photo generated electrons and holes in the conduction and valence bands facilitate the redox reactions in the same manner as electrolysis. Surface area and active sites must also be considered, as the lack of active sites will result in recombination of photo generated electrons and holes.

After all the above is achieved, there still lies the final obstacle in the separation of produced hydrogen and oxygen gas as they are produced simultaneously and are about the same size. One proposed solution is the use of molecular sieves with 5 Å pore diameter as they are able

to separate oxygen and hydrogen, albeit at a cost. Whereas for electrolysis, the use of salt bridge in the electrolyte is able to separate the cathode from the anode and thus leading to separation of hydrogen and oxygen without further processing.

1.3.2 Electrolysis

Electrolysis of water is the decomposition/splitting of water into hydrogen and oxygen as the result of an electric current. Equations 1-4 and 1-5 show the oxidation anode and reduction cathode half-reactions, respectively, whereas equation 1-6 shows the overall reaction.

$$2\ H_2O(l) \rightarrow O_2(g) + 4\ H^+(aq) + 4\ e^- \tag{1-4}$$

$$2\ H^+(aq) + 2\ e^- \rightarrow H_2(g) \tag{1-5}$$

$$2\ H_2O(l) \rightarrow 2\ H_2(g) + O_2(g) \tag{1-6}$$
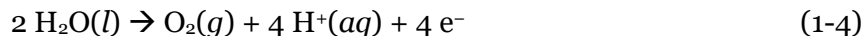
The standard potential (E^o) at 25°C to split pure water is 1.23 V, which corresponds to Gibbs free energy requirement of 237.2 kJ/mol using Nernst equation[8]. The oxidation reaction at the anode is commonly referred to as the oxygen evolution reaction (OER) whereas the reduction reaction at the cathode is known as the hydrogen evolution reaction (HER).

With either method, high purity hydrogen can be obtained. Photocatalysis involves the excitation of electrons and holes as a result of sun radiation. Compared to electrolysis, photocatalysis seems on the surface to be infinitesimally better, but the biggest disadvantage is perhaps the resulting unstable output, which is highly dependent on the weather condition. The fluctuation from photocatalysis is likewise found in solar panels or wind farms where a dire solution for energy storage is needed to address this unstable energy production problem. Our electricity grid system serves as a method to transmit stable amount of energy, it cannot store electrical energy nor handle big disturbances without causing blackouts. This is where hydrogen evolution through electrolysis of water could provide a viable method of energy storage to take advantage of the excess energy generated by the solar panels of wind farms. To cite an extreme

case, the Germans were actually being paid to use energy due to the excess generated by wind farms. Albeit this is an extreme example, wind farms are known for their inability to sell 100% of energy generated back to the grid due to the fluctuating energy generation dilemma. Hydrogen evolution through electrolysis of water can effectively take advantage of this dilemma in order to be competitive with traditional methods as the bulk of the cost associated with water splitting comes from the electricity requirement.

1.4 Hydrogen Evolution Reaction (HER)

In order to split water efficiently, both the cathodic and anodic reaction need to be catalyzed. Oxygen evolution reaction has been discussed extensively elsewhere, so this thesis will focus on the cathodic reaction, hydrogen evolution reaction[9,10]. The possible reactions for HER are shown in Table 1.1, where the pathways for HER may occur via either a Volmer-Heyrovsky mechanism or Volmer-Tafel mechanism. Both mechanisms proceed with the adsorbed hydrogen atoms (H_{ad}) at the electrode surface. Thus the dependency on the apparent standard Gibbs free energy of adsorption[11,12]. For an optimal catalyst performance, the standard Gibbs free energy of adsorption should be close to zero, indicating neither a strong nor weak hydrogen bonding[11–13].

Table 1.1 Possible reactions for HER[14]

Mechanism	Reaction
Volmer	$H^+ + e^- \rightarrow H_{ad}$
Heyrovsky	$H^+ + H_{ad} \rightarrow H_2$
Tafel	$2\ H_{ad} \rightarrow H_2$

In order to quantify the efficiency of HER catalysts, the following three parameters are used[11,12,15]:

1) Overpotential – the excess potential that must be applied to initiate a redox event, it is the difference between thermodynamically determined reduction potential and experimental observation

2) Exchange current density – describes the catalytic activity or the rate of reaction when the overpotential is zero; a larger value corresponds to faster reaction and vice versa

3) Tafel slope – provides information in regards to the rate determining steps or mechanisms at work. Tafel slopes of 120, 40 and 30 mV/dec corresponds to Volmer, Heyrovsky, and Tafel rate determining steps, respectively. The mechanisms were solved under steady state conditions without kinetic approximation.

An ideal HER catalysts should have low overpotential, high exchange current density and low Tafel slope. Precious materials such as platinum, rhodium, and palladium are the material of choice for the hydrogen evolution reaction due to their excellent electrical conductivity. At room temperature, the electrical conductivity of platinum was estimated to be 9.43×10^6 S/m compared to MoS_2 pellet at 0.1 S/m[16,17]. However, platinum is a precious metal, which makes it scare and expensive to use for commercial scale hydrogen production[18]. This thus leads to molybdenum disulfide (MoS_2), an abundant metal dichalcogenides that is commonly used as lubricant due to its low friction properties or catalyst for hydrotreating processes in petroleum refineries (removal of sulfur) when supported on alumina[19–21]. On the bulk scale, this material is not an active HER catalyst as the active sites are located at the sulfur edges[22]. Whereas on the nanoscale, MoS_2 is attractive as it exhibits significantly improved HER activity due to increased edge sites associated with catalytic activity or additional sulfur vacancies and grain boundaries in the basal plane contributing to improved performance[23,24].

1.5   Molybdenum Disulfide

Molybdenum disulfide is an inorganic compound that occurs in nature as molybdenite while MoS_2 nanosheets could be synthesized from bottom-up via chemical reactions under

hydrothermal conditions with precursors or top-down via exfoliation aided by solvents or surfactants[25–28]. On the bulk scale, MoS_2 is an inert material with properties that resemble graphite and is commonly used a lubricant due to its low fiction properties. Recent empirical findings have shown that exfoliation of the bulk MoS_2 into monolayer results in an enhancement in semiconducting properties along with a band gap transformation from an indirect band gap ~1.23 eV to a direct band gap of ~1.8 eV[21]. Band gap is an energy range where no electron states exist and it is a major determinant of solids semiconductors or insulators' electrical conductivity. Indirect band gap simply means that the electron must transfer momentum to the crystal lattice as the electron cannot jump from the valence band into the conduction band without a change in momentum. This thus results in no photon being emitted.

The two most common crystal phases for MoS_2 are the semiconducting trigonal prismatic (2H) and the metallic octahedral (1T), with the 1T phase being more conductive and metastable[29–31]. Ultraviolet-visible light spectroscopy is able to differentiate between the 2H and 1T phase as the 2H phase is emissive while the 1T phase does not have any photoluminescence properties. Semiconductors are more useful than conductors when it comes to altering the conductivity in a controlled fashion via doping – introduction of contaminants into a semiconductor crystal. In negative-doping, 5-valent dopant such as phosphorus is used due to the ability of the 5th electron to move around freely while acting as a charge carrier. Whereas in positive-doping, 3-valent dopant such as boron is used due to the extra hole available to catch an additional electron. Despite the 1T phase having denser atom configuration and higher electronic conductivity in the basal plane, it is easier to work with the semiconducting 2H phase due to its stability and ability to be modified in a controlled manner[32].

Figure 1.4 shows the sandwich arrangement of the Mo^{+4} and S^{-2} atoms. The S-Mo-S are connected via covalent bonds whereas van der Waals interactions hold together the hexagonally packed sandwich layers (interlayer spacing ~ 0.615 nm)[21]. Through density functional theory

(DFT) calculations, Tributsch and et al. have shown that the active sites are located at the edges while other research groups have used empirical studies, electrochemical measurements in combination with scanning transmission microscopy (STM) of MoS2 nanoparticles grown on Au (111) surface to demonstrate that the edge sites are indeed active while the basal plane is inert[32–34]. It is suggested that the activity of MoS_2 catalysts are closely associated with the sulfur edges, where the number of active sites and electrical contacts are crucial to the catalyst's efficiency[35,36]. In order to increase the HER efficiency, nanostructure MoS_2 on the monolayer is desired due to the increasing number of exposed sulfur edges and decrease in conductivity resistance as the activity is correlated directly with increased number of edge sites and not surface area[23,37]. Liquid phase exfoliation can exfoliate the 2H MoS_2 into few- and monolayers, with the 1H MoS_2 containing only a monolayer of S-Mo-S with lattice constant of 0.316 nm[27,38]. However, various methods are available in obtaining monolayer MoS_2. A brief summary of the various methods are discussed below.
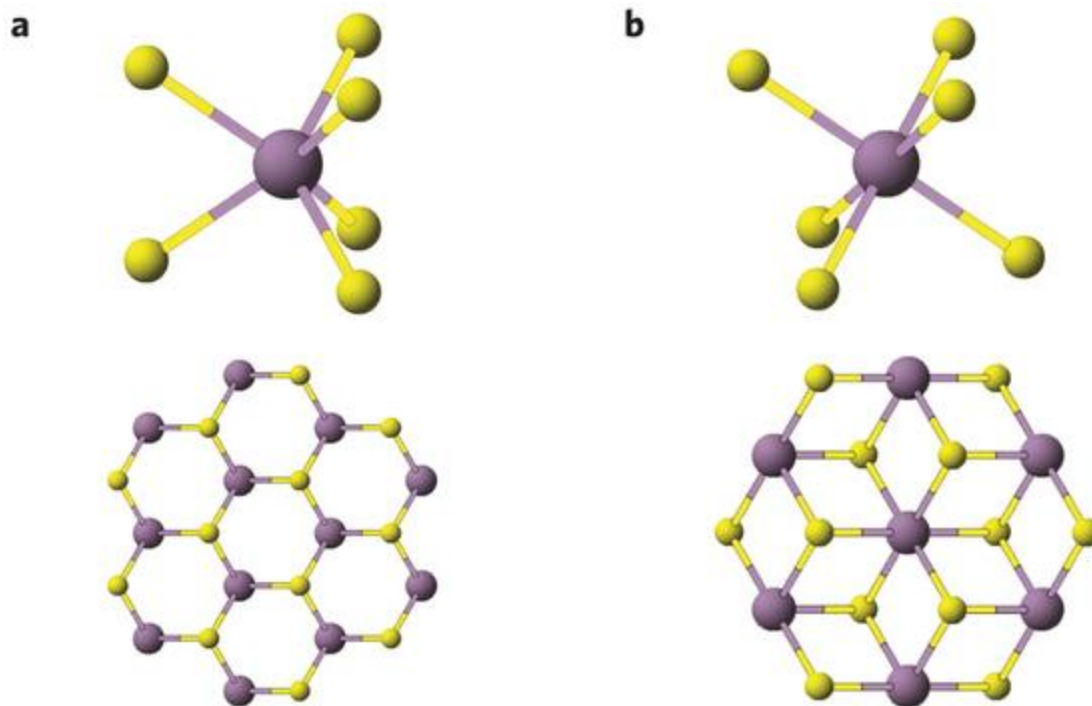
Figure 1.2 Polymorphism of MoS_2 a) trigonal prismatic (2H) b) octahedral (1T), reproduced with permission[39]

1.5.1 Mechanical and Chemical Exfoliation

In 2013, the Nobel Prize in Physics was awarded to the "Scotch tape method" to exfoliate bulk graphite into graphene[40]. This helped pave the way to fabrication of high quality 2D monolayer materials from bulk material via mechanical exfoliation, a top-down approach. Through repeated peeling of the bulk MoS_2 with the tapes, random flakes of MoS_2 are produced. The mechanically exfoliated material are typically pristine, clean and defect-free which allows it to be used in fundamental research or thickness dependent applications[26]. Whereas for practical applications, mechanical exfoliation cannot control sheet sizes or number of layers along with lack of yield[26,29]. Previous literature results demonstrated the application of few- and monolayer of MoS_2 as NO gas sensors, with superior performance from the 2-4 layers MoS_2 as the monolayer showed rapid but unstable response[26]. On the contrary, MoS_2 monolayer is an excellent photocatalysts that drives the photocatalytic water splitting reaction[41].

1.5.2 Chemical Vapor Deposition (CVD)

Chemical vapor deposition is a bottom up approach where controlled synthesis of MoS_2 is achieved with precursors such as Mo based powder, MoS2 powder, ammonium thiomolybdates $(NH_4)_2MoS_4$, MoO_3, and $MoCl_5$ deposited onto a wafer[42,43]. This method provides a high degree of control that allows the preparation of uniform continuous single film with controlled thickness as well as preparation of layered hetero structures without interfacial contamination[42]. Figure 1.5 shows a schematic diagram where MoS_2 was synthesized in a quartz tube with a single-zone furnace at atmospheric pressure[42]. In the reviewed literature, ultra-pure argon was used as the carrier gas for sulfur, sulfur powder and MoO_2 powder were used as precursors, and a boron-doped silicon wafer with a SiO_2 thermal oxidation layer was used as the substrate for the actual growth of MoS_2[42]. Factors such as the amount of source materials, distance between substrate and source material, introduction time of sulfur, temperature and pressure all contribute to the growth of M oS_2. Disadvantages of chemical vapor deposition include high temperature requirement (typically between 300°C-900°C), use of specialized precursor materials, concerns of safety when highly toxic, explosive or corrosive precursors are used, and the type of substrate that can be coated as films are typically deposited at elevated temperatures[43].
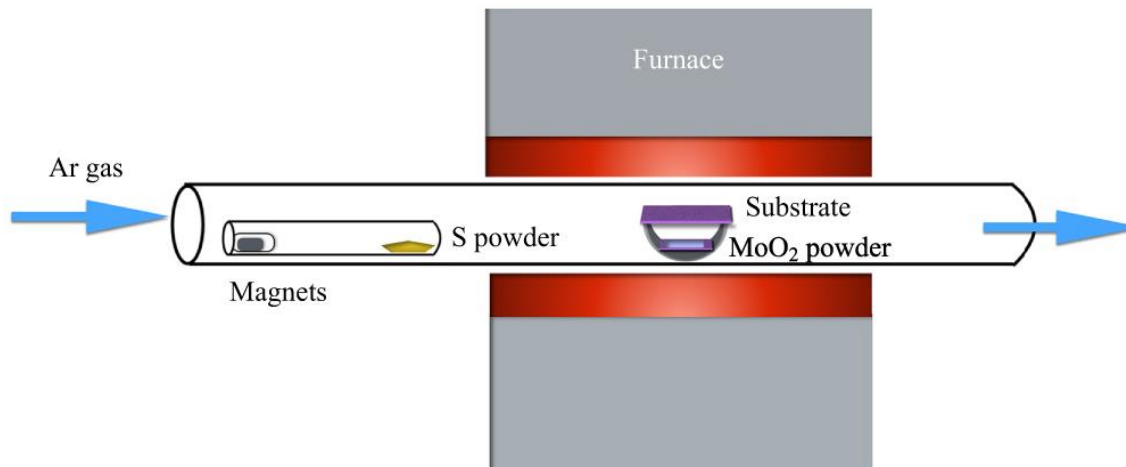
Figure 1.3 Schematic diagram of MoS$_2$ CVD growth under atmospheric pressure in a quartz tube, reproduced with permission[42]

1.5.3 Solvothermal/Hydrothermal Synthesis

Solvothermal and hydrothermal synthesis are two possible methods to produce MoS$_2$ through solution chemistry under high temperature and pressure conditions. The differentiating factor between the two methods is that the state of precursors for solvothermal method is typically non-aqueous and hydrothermal method essentially uses water as the solvent[25,27]. Sodium molybdate and thiourea are the typical sources of molybdenum and sulfur, respectively. An autoclave is typically used in the synthesis and post-annealing is used to increase purity and crystallinity[25]. Similar to chemical vapor deposition, this method offers the fine-tuning of desired shapes through temperature, concentration and reaction time controls[27]. Disadvantages associated with this method are difficulty in controlling synthesis, large particle size distribution and various layers of MoS$_2$[25,27,44].

1.5.4 Liquid Phase Exfoliation (LPE)

Pioneered by Hernadez et al. in 2008, liquid phase exfoliation in organic solvents such as N-methyl-pyrrolidone (C$_5$H$_9$NO) was first used to prepare graphene from graphite with ~ 1 wt% monolayer yield[45]. Eventually, this was applied to various transitional metal dichalcogenides, such

as MoS_2. This method uses the cavitation effect – the formation of vapor in liquid, followed by the collapse of bubbles to exfoliate the bulk material into few- and monolayers while dispersing and stabilizing the material against aggregation in organic solvent through matching of surface tension between the layered material and solvent[21,45,46].

Figure 1.6 shows the three primary criteria in order to achieve the successful exfoliation of TMDs, in this case MoS_2: 1) dispersion of to-be exfoliated material in the solvent of choice, 2) exfoliation of material and 3) stabilization of exfoliated material against re-aggregation[29,46,47]. Liquid phase exfoliation is essentially combining the top-down approach of mechanical exfoliation with the use of suitable solvent to minimize the net energy cost of exfoliation while preventing the re-aggregation of exfoliated nanosheets. Sufficient immersion of material in the dispersant reduces the contribution of London dispersion force to van der Waals attraction in adjacent layers which aids in exfoliation[37,47,48]. Exfoliation of the material is achieved by the collapse of high-intensity bubbles (cavitation effect) generated from an ultrasonic probe operating at 20 kHz and an ultrasonic bath operating at 40 kHz. The resulting cavitation effect is able to exfoliate the material into mono- or few-layers of nanosheets. Nanosheets have a tendency to re-aggregate upon exfoliation if a stabilizing agent is not present. Thus, a stabilizing agent in the form of a polymer or surfactant is typically required. An ideal solvent is one that will aid both the exfoliation process and acts as the stabilizing agent.
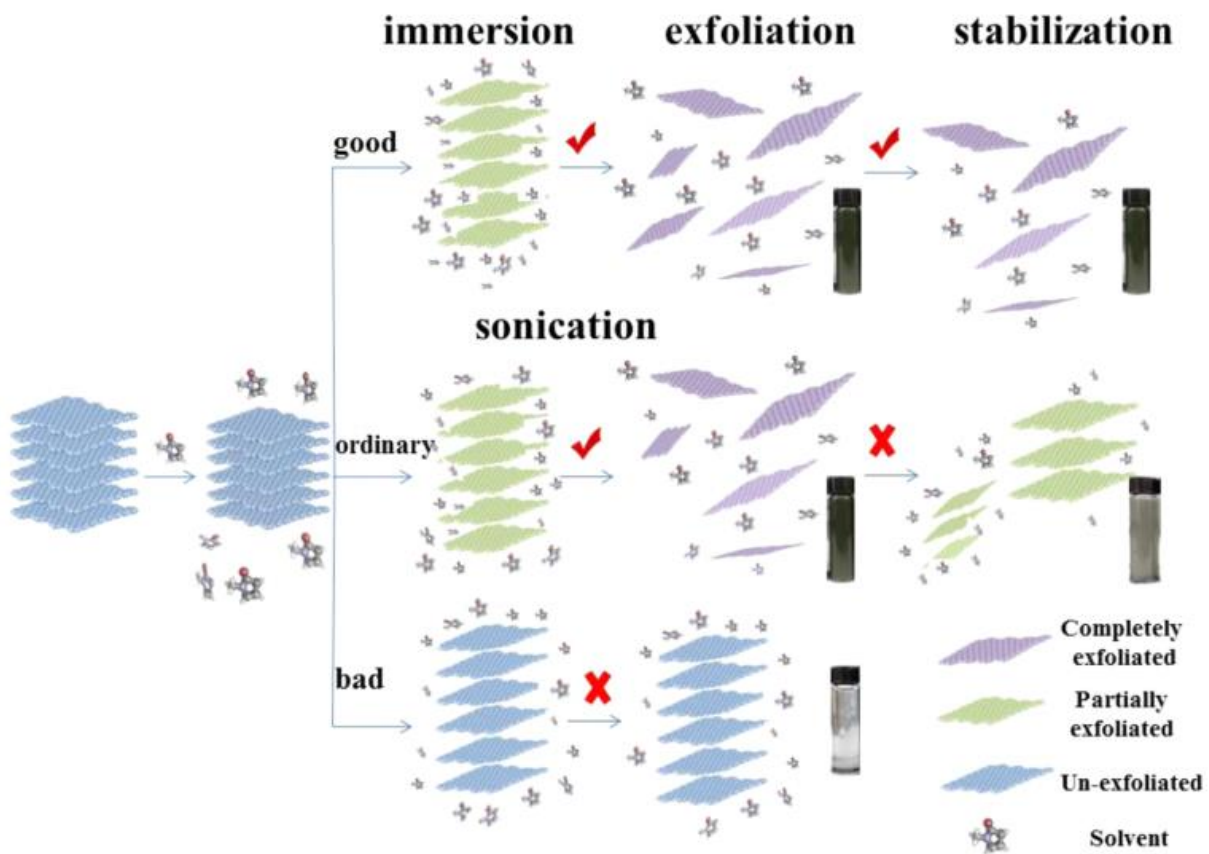
Figure 1.4 The three stages of liquid phase exfoliation with the effect of good/bad solvents, reproduced with permission[47]

Coleman et al. first discovered the exfoliation of TMDS in organic solvents that do not require polymers or surfactants as stabilizing agent by matching the surface tension of organic solvent with the surface energy of the material[29]. This ensures efficient exfoliation while simultaneously stabilizing the exfoliated material. A detailed discussion of methodology can be found in his paper[29,45].

The exfoliation process is analogous to the mixing of two materials where the energy of mixture can be best described by the change in Gibbs free energy (ΔG_{mix}) of the mixture. With two substances mixing, an increase in entropy (S) is expected along with a change in the enthalpy (H)

of the system. The Gibbs free energy of the mixture is used to describe the solubility of the two materials. Assuming isothermal condition, the equation is given as follow:

$$\Delta G_{mix} = \Delta H_{mix} - T\Delta S_{mix} \tag{1-7}$$

where ΔH_{mix} and ΔS_{mix} are the changes in enthalpy and entropy of the mixture due to mixing, respectively. In order for the process to be spontaneous (i.e. soluble), ΔG_{mix} should be less than or equal to zero. The second law of dynamics states that the entropy of an isolated system can only increase over time. Therefore, the change in enthalpy of the mixture due to mixing is the dominant term in determination of ΔG_{mix}.

From the work of Coleman et al. published in 2008, an approximately expression for the enthalpy of mixing per unit volume was derived in terms of easily obtainable solvent properties. The energy requirement for exfoliating nanosheets are as follow:

$$\frac{\Delta H_{mix}}{V_{mix}} \approx \frac{2}{T_{flake}} (\delta_m - \delta_v)^2 \varphi \tag{1-8}$$

where V_{mix} is the total volume of the mixture, T_{flake} is the thickness of the dispersed flake, φ is volume fraction of dispersed flake, δ_m and δ_v are the square root of the surface energies of dispersed flake and solvent, respectively. In order to minimize the Gibbs free energy of mixing, the enthalpy of mixing needs to be minimized. This can be achieved by minimizing the bracketed terms through matching the surface energy or alternatively surface tension of the solvent with the exfoliated material. Matching of surface energy may be the most important contribution to minimizing enthalpy of mixing, but it is equally important to pay due diligence to the other variables. In order to obtain stable flakes on the few- or monolayer size, one has to combat the increase in enthalpy as a result of decrease in the thickness of dispersed flakes. This can be achieved by careful selection of solvent. The same issue is likewise present in obtaining higher concentration of dispersed flakes. In addition, volatility of the solvent should be considered as solvents with higher volatility are easier to evaporate and thus making the solvent removal process

hassle-free. Residual solvents may contribute to the overall efficiency of the hydrogen evolution reaction or affect other applications inadvertently. Therefore, a fine balance between flake thickness, difference in surface energies of flake and solvent, and concentration of dispersed flakes need to be achieved in order to minimize the Gibbs free energy of mixing.

The above concept is derived based on Hansen solubility parameter (HSP), therefore the limitations of HSP applies equally here. HSP was developed as a way of predicting whether one material will dissolve in another to form a solution, however only three parameters are taken into consideration in HSP; they are dispersion forces (van der Waals), dipolar intermolecular (dipole moment) force and hydrogen bonding between molecules[49]. In order to predict the optimal co-solvent concentrations where organic solvent isn't used, Halim et. al had probed the liquid-solid interfacial energy through contact angle measurement in order to avoid making assumption about a material's solubility or material-solvent interactions[49].

The thermodynamic stability was determined by evaluation of the solid-liquid interfacial energy based on the Young's equation:

$$\gamma_{SL} = \gamma_{SG} - \gamma_{LG} \cos\theta_c \tag{1-9}$$

where γ_{SL}, γ_{SG}, and γ_{LG} are the interfacial energy for solid-liquid, solid-gas, and liquid-gas, respectively with θ_c being the equilibrium contact angle. Even though the interfacial energy for solid-gas is hard to measure between the solid and atmosphere, it is constant for the same material, independent of solvent used. The liquid-gas interfacial energy in a liquid is precisely the surface tension, which could be obtained readily from existing published data. The objective is to obtain a thermodynamic stable system through minimizing solid-liquid interfacial energy by maximizing the $\gamma_{LG} \cos\theta_c$ term[49]. Using this method, Halim et al. discovered that the maximum exfoliation of MoS_2 occurs in alcohol-water mixtures with surface tension in between 30-35 mJ/m^2. That will be used as a starting point to determine the optimal alcohol-water mixtures for our liquid phase exfoliation.

Perhaps the biggest advantage of liquid phase exfoliation other than the relative ease of process lies in its ability to maintain the structural and electronic integrity that are commonly associated with few- and monolayers of MoS_2. More often that or not, solvothermal/hydrothermal synthesis of MoS_2 via chemical reactions can introduce disorder and defects on the basal plane[23]. Liquid phase exfoliation (LPE) does not involve chemical reactions, nor is it air-sensitive. Combining this with a non-pyrrolidone solvent (pyrrolidone solvents are known reproductive toxins) with low boiling point such as isopropanol/water, the environmental risk of LPE is mitigated significantly.

1.6   Summary

The above literature review shows that it is possible to produce hydrogen through various methods that will significantly decrease greenhouse gas emission while contributing to a better future. The biggest challenge facing renewable energy is energy storage, hydrogen evolution reaction through electrolysis of water could be a viable solution while at the same time producing high purity hydrogen that could be used in the various applications where impurities are not tolerated, i.e. pharmaceutical, food processing, and preservation. There is no one solution fit all, as each of the synthesis methods are associated with their respective advantages and disadvantages. Thus, the synthesis methods should be selected based on the intended application(s). For the development of hydrogen evolution reaction, MoS_2 was chosen based on its relative abundance and low cost compared to noble metals. Liquid phase exfoliation was selected due to its relative ease of use, safer operation compared to the use of autoclave where high pressure and/or temperature are required and abundance of yield. Monolayer MoS_2 is desired in water splitting applications due to the increased amount of edge sites as well as significantly lower resistance compared to the few layered structure. In addition, the active sites of MoS_2 are located on the hydrophilic edge, where liquid phase exfoliation is able to increase the number of edge sites through exfoliating the bulk material into nanoscale. However, more research is required to improve the catalyst efficiency and overall yield rate while taking the

16

environmental factors into consideration. Thus, the focus of this research will be on material preparation through liquid phase exfoliation, characterization of bulk and exfoliated material, as well as a demonstration of application of catalysis via hydrogen evolution reaction.

1.7   Organization of thesis

In Chapter 1, an overview of the potential applications for molybdenum disulfide nanosheets were provided with a brief comparison of the advantages and disadvantages of synthesis methods. In Chapter 2, I will present the details of material characterization methods and experimental setup with liquid phase exfoliation using both organic solvents and co-solvent of isopropanol/water. In Chapter 3, I will discuss the experimental results for liquid phase exfoliated molybdenum disulfide nanosheets in n-methyl-pyrrolidone and co-solvent of isopropanol/water. In Chapter 4, the experimental results presented in Chapter 3 will be summarized, contributions to original knowledge will be stated and future works regarding the liquid phase exfoliation of molybdenite will be proposed.

Chapter 2 Materials and Experimental Techniques

2.1 Overview

In this chapter, molybdenum disulfide preparation, experimental setup with organic solvent and co-solvent of isopropanol/water, and characterization techniques used for the natural mineral and exfoliated material in organic solvent and co-solvent of isopropanol/water will be discussed.

2.2 Materials

2.2.1 Molybdenum (IV) Disulfide – MoS2

Natural MoS_2 mineral was obtained from the Wolfram mine located in Queensland, Australia. Prior to use, they were crushed and grinded down to less than 38 μm through ball milling and sieve. The mineral was then used as it is for experiments without further processing. The as-obtained mineral was characterized with X-ray powder diffraction (XRD). MoS_2 powder with average sizing of 6 μm and 99% assay purity was purchased from Sigma Aldrich and used as it is. This powder was used as a reference to compare the mineral to during XRD in addition to the tabulated powdered diffraction database.

2.2.2 Isopropanol/Deionized Water (DI) Co-Solvent Mixture

Based on literature results of thermodynamic stability due to solid-liquid interfacial energy and empirical trial and error, a mixture of 45/55 vol% isopropanol/DI water (18.2 MΩ·cm at 25°C) was selected as the co-solvent for the liquid phase exfoliation of MoS_2 into nanosheets[49]. An initial MoS_2 concentration of 2 mg/mL of solvent was used for all experiments involving isopropanol/water solvent. Isopropanol was purchased from Fisher Scientific and used as it is without further processing. Liquid phase exfoliation was achieved under ambient conditions. Exfoliation of MoS_2 mineral was achieved with a use of 160 W ultrasonic bath for 90 minutes followed by subsequent probe sonication at 210 W (30% * 700 W) with a ¼ inch micro-tip. Bottom will refer to the precipitated solids after centrifugation at a certain relative centrifugal

speed (RCF) whereas supernatant will refer to the top half of the solution after centrifugation. Samples were centrifuged at various speeds with the 400G RCF bottom containing unexfoliated/bulk MoS_2 and the 12800G RCF supernatant containing the desired nanosheets. The samples were then freeze-dried to remove the isopropanol (IPA)/water solvent before further electrochemical characterization.

2.2.3 Organic Solvents

There has been a wide range of estimates for the surface energy of MoS_2, varies from ~45 mJ/m² for few-layers experimentally to > 250 mJ/m² based on theoretical calculations[50,51]. However, the surface energy of edge-terminated structure is reportedly much higher in magnitude (2X) compared to the 2-D basal plane structure[51]. In a separate layer thickness wettability study, Anand et al. have discovered thinner layers contributed to higher contact angle, which in turn lead to even higher surface energy[51]. Thus, a wide spread exist in the published data for the surface energy of Mos_2 depending on layer thickness.

Table 1.1 shows the organic solvent used in the liquid phase exfoliation experiments, they were selected by matching their surface tension to the approximate value of 46.5 mN/m for the surface energy of few-layers of MoS_2. Their efficiency in the exfoliation of MoS_2 will be explored and compared in the experimental section.

Table 2.1 Organic Solvent used in the Liquid Phase Exfoliation experiment[29,51,52]

Name	Surface Tension (mN/m)
CHP (N-cyclohexyl-2-pyrrolidone)	43.2
NMP (N-methyl-2-pyrrolidone)	41.0
N12P (N-dodecyl-2-pyrrolidone)	33.8
N8P (N-octyl-pyrrolidone)	33.6

Sometimes in published work, there may be a discrepancy between surface energy and tension of the same material. This could be explained by the way the value was reported, as the surface energies of liquids are typically ~30 mN/m higher than their respective surface tension[29]. The relationship between surface energy and surface tension are shown below:

$$Y_s = E_s - TS_s \qquad\qquad (2\text{-}1)$$

where Y_s is the surface tension (Newton/m), E_s is the surface energy (Joule/m^2), T is the temperature (in Kelvin) and S_s is the surface entropy (Joule/m$^{2\cdot}$K).

2.2.4 Organic Solvent Removal through RotoVap

As mentioned previously, the removal of organic solvents after exfoliation is considered to be a very tedious task due to the high boiling points. A common method is to use a rotary evaporator to evaporate the solvent at low pressure. In this experiment, a Buchi R-210 RotoVap system was used. Figure 2.4 shows the setup with an oil bath as the boiling points of organic solvents are typically greater than 100°C. Special care must be taken while operating the RotoVap. For NMP, the RotoVap was operated temperature of 200°C for 30 minutes to evaporate off the solvent. After the evaporation process, the MoS$_2$ nanosheets are washed off the walls of the spherical flask and freeze-dried. Regardless of how well the RotoVap process is controlled, there will still be some residual solvents left after freeze-drying due to the limitation of this equipment. This is another disadvantage for organic solvent if the final application of the exfoliated material cannot tolerate traces of residual solvent (i.e. use of MoS$_2$ nanosheets to produce hydrogen for the food processing industry or pharmaceutical industry).

Figure 2.1 RotoVap experimental setup with vacuum pump and cooling water cycling system

(not shown here)

2.3 Synthesis

2.3.1 Pre-Processing with Ultrasonic Bath

A 9.5 L ultrasonic bath from Fisher Scientific with output of 160 W was used for the pre-processing of samples prior to ultrasonic probe processing. MoS_2 was mixed with organic solvents at 5:1 weight ratio before sonication in the ultrasonic bath for 1.5 hours. For the isopropanol/water solvent sample, MoS_2 was mixed in with the co-solvent at a ratio of 2 mg of MoS_2 per mL of co-solvent. Ice cubes were regularly deposited into the ultrasonic bath for temperature control. Samples pre-processed with ultrasonic bath followed by ultrasonic probe sonication (BP) were compared with probe sonication only samples. Probe sonication induces cavitation directly in the solution and henceforth able to have higher output energy with the same input, whereas ultrasonic bath waves need to pass through a fluid (commonly water) medium in the bath and the glass vial

holding the solvent. In theory, probe sonication should be able to induce a higher degree of cavitation within the liquid and thus achieving better exfoliation efficiency.

2.3.2 Liquid Phase Exfoliation

MoS_2 was exfoliated from natural mineral MoS_2 by mixing 2 mg of MoS_2 per mL of co-solvent of IPA/water and 5 mg of MoS_2 in per mL of organic solvent. A higher initial concentration was used for the organic solvent because it was initially thought that the yield would be higher with higher initial concentration. That proved to be not the case, the overall yield for the exfoliated nanosheets in organic solvent remained the same regardless of 5 mg/mL or 2 mg/mL of MoS2/organic solvent. Exfoliation was performed within a 50 mL stainless steel vial placed within an ice bath, see Figure 2.2 for experimental setup. Stainless steel vial was used as jacketed glass beakers will break during sonication. Fisher Scientific™ Model 705 Sonic Dismembrator with ¼ inch micro-tip was used throughout the liquid phase exfoliation process. MoS_2 flakes were obtained by sonication of bulk MoS_2 at 210 W (30% × 700 W) in ambient atmosphere for 45 minutes with 6s on and 2s off to prevent excessive heating that may damage the probe as well as to prevent degradation of solvent as a result of heating[53,54]. Isopropanol 99.5% was purchased from Sigma Aldrich and used without further processing along with deionized water (18.2 MΩ·cm at 25°C). All organic solvents were purchased from Sigma Aldrich and used without further processing. In order to satisfy the isothermal assumption as well as ensure safe operation, an ice bath was used during the entire exfoliation process and changed every 30 minutes to ensure the temperature of the solution is kept below 60°C as the lowest of boiling point as per the SDS. The ice bath may not be an adequate solution to satisfy the isothermal assumption due to cavitation hot spot generated by the ultrasonic probe. A sound barrier within the fume hood was used to ensure adequate sound isolation and ventilation for the ultrasonic dismembrator.

Figure 2.2 Liquid phase exfoliation experimental setup with the probe, stainless steel vial and
ice bath

2.3.3 Liquid Cascade Centrifugation

Dispersions produced from the liquid phase exfoliation was polydisperse along with the unexfoliated material. Unstable or heavier particles may eventually settle over time. However, the exfoliated nanosheets need to be isolated in order for proper characterization and application. This is achieved via centrifugation using a Sorvall™ WX80+ Ultra centrifuge with a T-865 Fixed Angle Rotor purchased from Thermo Fisher Scientific. In order to allow comparison to other centrifuges, the rotating speed will be reported in g-force (G) or RCF (relative centrifugal force) as RPM is dependent on the radius of rotation whereas g-force is directly related to gravity. The removal of un-exfoliated material is achieved via centrifugation at 400G for 1 hour and discarding the sediment. Size selection could be achieved by using liquid cascade centrifugation where increasing the rotational speeds yield decreasing nanosheet size and thickness[55]. Previous studies

have shown a broad distribution of nanosheets are observed ranging from 1-10 layers and 50 – 500 nm in length for MoS_2 samples produced from LPE[56]. This could be problematic as most applications place an emphasis on size control. In order to achieve efficient size selection, the supernatant should be decanted from the sediment as much as possible. Size selection is crucial as the exfoliated dispersions without centrifugation are typically polydisperse[55]. Albeit various applications are present for different sizes of MoS_2, the polydisperse solution will only result in inefficient utilization of resources. For example, mixing in monolayer MoS_2 with few-layers will not result in a noticeable enhancement whereas monolayer MoS_2 by itself will exhibit a direct transformation of band gap from indirect to direct[21,56]. In summary, bigger nanosheets could be used as means of mechanical reinforcement such as fillers for plastics whereas smaller nanosheets are desired for catalysis such as hydrogen evolution reaction due to its inherently large surface area[26,56,57]. At the same time, liquid cascade centrifugation dramatically decreases the amount of "waste" as size selection allows the isolation of size-specific nanosheets for its respective application.

After sonication of the samples with the sonic dismembrator, the samples were transferred directly to 30 mL centrifuge tubes. All samples were first centrifuged at 400G (2000 RPM) RCF for 1 hour to remove the un-exfoliated flakes[57]. The supernatant was collected for further processing. Subsequently, the organic solvent exfoliated nanosheets was then centrifuged at 3000G (5500 RPM) for 1 hour, with the sediment containing the larger size nanosheets. In order to obtain few/mono-layers, the organic solvent exfoliated nanosheets supernatant at 3000G was collected and centrifuged at 6000G (7700 RPM) for 1 hour. The 6000G supernatant obtained from organic solvents exfoliated nanosheets was used for further characterization. A similar procedure was used for the co-solvent of IPA/water, the only difference was the RCF speeds used. For IPA/water, RCFs of 400G, 6400G and 12800G were used, they are equivalent to 2000 RPM, 8000 RPM and 11200 RPM, respectively. A lower RPM was used for the nanosheets exfoliated in organic solvents because of initial assumptions made in regard to centrifuge. Upon centrifuging

24

the 6000G supernatant obtained from organic solvent at 12800G, no sedimentation was observed. Therefore, there seems to be a threshold RCF for samples exfoliated in organic solvents where increasing RCF beyond 6000G resulted in little or no sedimentation. The same did not apply to the co-solvent exfoliated nanosheets, as centrifuging the supernatant taken at 6400G at 12800G resulted in sedimentation and separation. This could be attributed to the much higher concentration of nanosheets present in the co-solvent environment.

2.3.4 Effect of Natural Sedimentation for Removal of Un-exfoliated Flakes

It was reported previously that natural sedimentation of sonication processed solutions was able to separate the un-exfoliated flakes from the exfoliated flakes. This hypothesis was tested out with three organic solvents and the before/after 3 days comparison is shown in Figure 2.3. In order to test the aforementioned hypothesis, the supernatant of the solutions sitting for 3 days were collected and centrifuged at 400G RCF. A time period of 3 days was arbitrarily chosen. In hindsight, 1 day should have been enough. If the separation of un-exfoliated flakes from the exfoliated flakes were complete, then there should be little or no sedimentation at 400G RCF. However, sedimentation were present for all 3 samples at 400G RCF. Thus, it is safe to conclude that natural sedimentation was not effective at complete separation of un-exfoliated flakes from the exfoliated ones. Perhaps the most obvious observation is how stable the N-dodecyl-2-pyrrolidone (N12P) exfoliated MoS_2 is compared to the other two organic solvents after 3 days. There may be natural sedimentation, but it was not noticeable enough in N12P compared to the other two organic solvents. Either way, this test showed that the exfoliation was superior in N12P or that N12P was a better solvent for the stabilization of exfoliated MoS_2. A similar observation was made for MoS_2 exfoliated in the co-solvent of alcohol and water (not shown here).
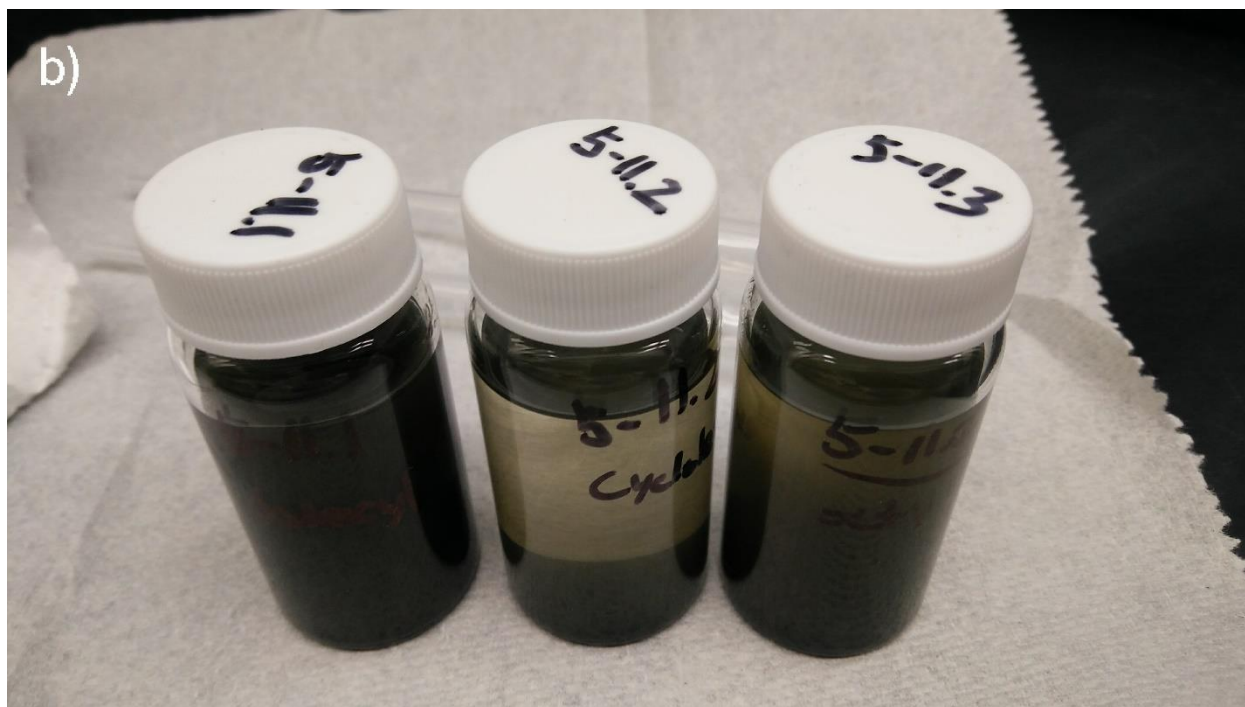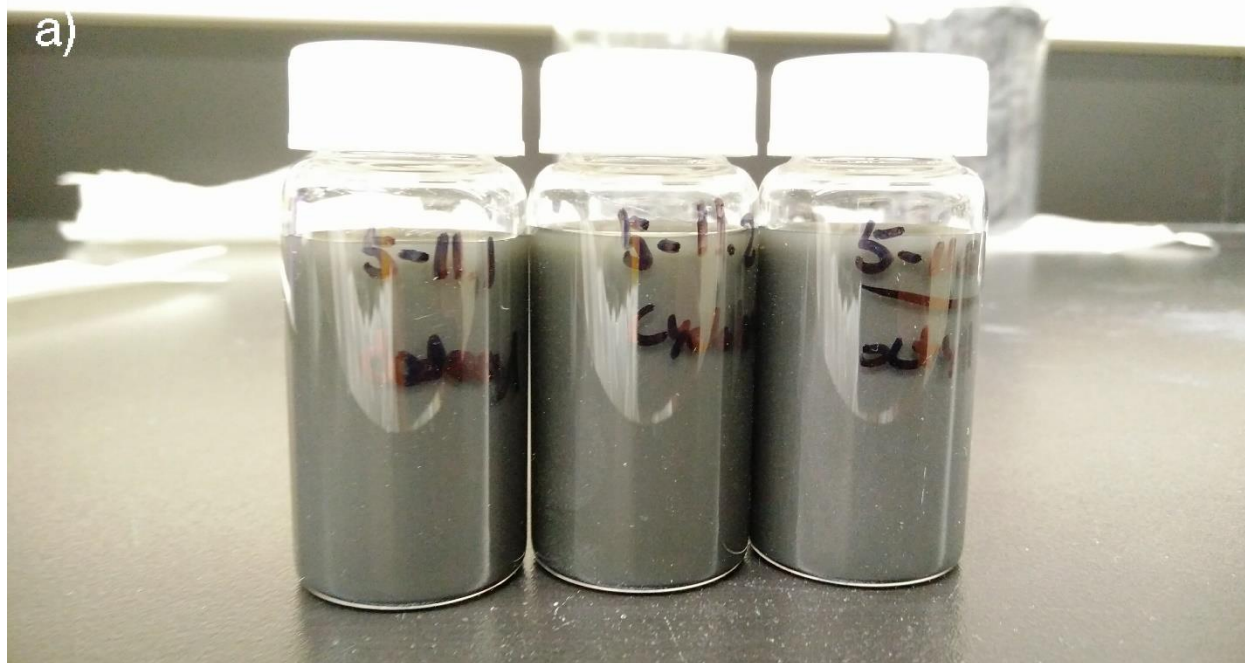
Figure 2.3 Sonicated MoS$_2$ flakes immersed in from left to right: N12P, CHP, N8P, a)

immediately after sonication b) after 3 days

2.3.5 Washing of MoS₂ Samples Obtained from Organic Solvent

It is possible to wash the organic solvent exfoliated nanosheets through repeated centrifugation at a certain G-force by re-dispersion of sediment. However, the drawbacks may outweigh the benefits. Washing is able to remove the organic solvent which makes characterization or further sample processing much easier. In addition, repeated washing with ethanol and water (more than 5 cycles) can remove the organic solvent which will lead to higher quality TEM images along with increased stability under the TEM beam. Combining washing with dialysis, it is possible to remove most of the organic solvents.

The case against washing of the nanosheets for the removal of organic solvent is primarily attributed to the concern for re-aggregation. The collapse of nanosheets structure was noticeable as the washing process requires re-dispersion of sedimentation via Fisher Scientific™ CPX Series Digital Ultrasonic Cleaning Bath (120V). As mentioned earlier, the organic solvent serves the roles of exfoliation and stabilizing agent simultaneously. By dispersing the nanosheets in water (72.8 mN/m) or ethanol (22.1 mN/m) after washing, it will lead to the re-aggregation of the nanosheets due to the difference in surface tension. Figure 2.4 shows what happened to MoS₂ nanosheets prepared by washing away the organic solvent with ethanol and water. The solution was initially stable with no precipitation after washing. After one-week, noticeable precipitation was observed. Whereas for nanosheets immersed in organic solvent, the solutions were stable after several weeks with no precipitation. This is in agreement with previous published works where it was proposed that the stability of the exfoliated material was largely attributed to the charges created during liquid phase exfoliation (i.e. dispersion stability is achieved when all of the particles have either a negative or positive charge, thus repelling each other)[29,54,57].

Figure 2.4 Precipitation of nanoparticles after 1 week in DI water, sample was the supernatant

obtained 6000G RCF (left), yellowish color solution on the far right showing the

organic solvent stabilized nanosheets compared to samples that have not been

centrifuged after 1 week (right)

2.4   Characterization Techniques

2.4.1 Ultraviolet-Visible Spectrophotometry (UV-Vis)

UV-Vis spectrophotometry is an inexpensive, convenient, non-destructive technique that can be used to identify materials based on its unique characteristic wavelength. The interaction of the incident light with the material could result in elastic scattering where there is no energy exchange, inelastic scattering where the photon exchanges energy with the sample, or absorption of the photon by the sample.

Different molecules can absorb different wavelength of light due to the difference in energy required for atoms and molecules to undergo transitions. UV-Vis is the absorption or the reflectance spectroscopy in the ultraviolet-visible region (800 - 200 nm). Photon energy (E) can be described based on the Planck-Einstein relation below.

$$E = hf \qquad\qquad (2\text{-}2)$$

where h is the Planck's constant and f is the frequency. Frequency can also be obtained by dividing the speed of light in a vacuum by wavelength. Thus, the wavelength is inversely proportional to energy. For simple molecules (low melting and boiling points), the excitation energy is greater than complex molecules[58]. Thus, photon with shorter wavelength is more desirable to be able to excite a molecule from the ground state to the excited state. On the contrary, the energy levels of complex molecules are smaller and thus require photon with longer wavelength typically in or near the UV-vis regions. The characteristic wavelengths for MoS_2 are the A1 and B1 excitons peaks located at 610 nm and 670 nm, respectively[54,59]. Equation (2-2) shows the Beer-Lambert law.

$$A = \varepsilon lc \tag{2-3}$$

where measured absorbance (A) is directly related to the molar absorptivity constant (ε), path length (l) and concentration of the solution (c)[60]. The above equation can be rearranged to determine the concentration of dispersion at a specific wavelength within the UV-vis spectrum.

In an UV-Vis spectrometer, the same light source passes through the half mirror which splits the monochromatic beam into two equal intensity beams where one beam passes through the cuvette containing the reference while the other beam passes through an identical cuvette containing the sample. Electronic detectors are then used to measure the intensity of the beams and absorbance (A) is calculated with the following equation.

$$A = \log I_0/I \tag{2-4}$$

where I_0 is the intensity of the reference beam and I is the intensity of the sample beam.

In this work, UV-Vis was conducted using UV-3600 Plus spectrophotometer by Shimadzu with resolution of 0.1 nm. Baselines using fresh solvent were conducted prior to each run. The contributions from baselines were eliminated in all experimental results by using the corresponding organic solvent as the baseline case. The UV-vis spectra was obtained in absorbance mode from 800 – 200 nm.

2.4.2 X-ray Powder Diffraction (XRD)

XRD uses x-rays to determine the diffraction pattern of a material which allows identification of components in a sample by searching and matching to an existing database[61]. It is imperative to be able to access a standard reference database, otherwise the data will be meaningless. In addition, the detection limit for mixed materials is approximately 2% of the sample[62]. Thus, XRD is unable to detect trace contaminants in natural minerals. For reference to the standard database, JADE™ is one such software that search the maintained Powder Diffraction File database of X-ray powder diffractions. For pure substance, XRD is analogous to fingerprint whereas a mixture of substances produces pattern independently of one another. Thus, this allows the determination of the crystalline components within a sample and conversion of the detected x-rays to d-spacing allows identification of the mineral due to the unique d-spacing of each mineral.

Applications such as characterization of unknown crystalline materials, unit cell dimensions, sample purity, and orientation are all possible[62]. The fundamentals behinds XRD lies in the diffraction of x-ray similar to the spacing of the planes in a crystal lattice. The interaction of monochromatic x-rays and the sample produces constructive and/or destructive interference which gives rise to a diffracted ray only when the conditions to Bragg's Law are satisfied[62].

$$2d\ sin\theta = n\lambda \tag{2-5}$$

where d is the characteristic spacing between atomic layers in a crystal, n is the integral value of the incident wavelength (λ) and θ is the angle between the lattice planes and the incident x-rays[62]. Bragg's law explains the relationship between the incident wavelength of the electromagnetic radiation to the characteristic d-spacing and the diffraction angle. Scanning through a wide range of 2θ gives rise to all possible diffraction directions due to the random orientation of the material. Subsequent conversion of the peaks to d-spacing allows the identification of the material through matching to reference database.

In this work, XRD patterns were recorded with Rigaku Ultima IV focus beam mode, at 40 kV voltage, tube current of 44 mA, 3° per minute from 5° to 95° and a slit width of 10 mm. The MoS_2 natural mineral along with aliquot at different centrifuge speeds were characterized this way.

2.4.3 Scanning Electron Microscopy (SEM)

Scanning electron microscopy (SEM) works by rastering a focused beam of electron over a sample's surface where the electron beams interact with the atoms in the sample producing various signals in regards to the sample's topography and composition when an energy dispersive X-ray analyzer (EDX) is used in conjunction[63]. For elements with atomic number $\geq$ 11, EDX's sensitivity is in the range of 0.1 to 1% composition, whereas for smaller elements (i.e. hydrogen, helium, lithium), EDX is unsuitable as some of those elements do not have a characteristic X-rays or the low energy X-rays are subject to strong absorption within the specimen[63].

In this work, a Tescan Vega-3 SEM equipped with EDX was used to study the MoS_2 natural mineral, top layer of the MoS_2 mineral after floating it in water and the exfoliated material.

2.4.4 Transmission Electron Microscopy (TEM)

As humans, the smallest resolution we can differentiate is 0.1 mm, without microscope, that is all we will ever able to see[64]. The fundamentals of electron microscopy is to use beam of electrons to image a specimen down to the atomic scale, this is made possible due to electrons being smaller than atoms. The wavelength of visible light limits the resolution of images, whereas de Broglie demonstrated wave-particle duality in electrons with wavelength significantly shorter compared to visible light. This is where TEM shines as it is able to provide high resolution 2-D picture of the sample with details about composition, morphology, crystallization, grain boundaries and other defects by transmitting beam of electrons through a specimen[64]. TEM is versatile in characterizing various materials, from the nano regime of < 1 nm - ~ 100 nm to the micrometer scale and beyond.

As the saying goes, "know the forest before you start looking at the veins in the leaves on the trees." Prior to examining the sample with TEM (i.e. veins in the leaves), the sample should be examine with visible light microscopy to get an understanding of the forest. In addition, 2-D images are harder to interpret as they do not provide us with the depth of the features. Thus, depth-sensitive techniques should be used to obtain a complete characterization.

An electron gun first supplies the electrons that travel through vacuum in the column of microscope. The electrons are focused and converted to light with electromagnetic lenses which travels through the sample[64]. Some of the electrons may scatter or disappear as a result of the density of the sample, whereas the un-scattered electrons hit a fluorescent screen at the bottom of the microscope. The darker portion of the image reflects the increased density of the sample whereas the lighter portion represents more electrons passing through. Based on the varying degree of darkness, characteristics such as morphology, texture, and relative thickness can be identified.

In this work, a 200 kV JEM-2100 and JEM-ARM200CF TEMs were used to observe the morphology of exfoliated MoS_2 nanosheets. Samples were prepared using a by pipetting 3-5 μL of solution onto carbon square mesh (CF300CUUL) and ultrathin carbon grids manufactured by Electron Microscopy Sciences and dried under vacuum prior to characterization.

2.4.5 Atomic Force Microscopy (AFM)

Atomic force microscopy (AFM), also known as scanning force microscopy (SFM) is a scanning technique that is capable of producing high resolution image on the sub-nanometer scale depending on the specific technique and tip sharpness[65,66]. It was first described by Binnig et al. in 1986 as a combination of the scanning tunneling microscope (STM) and stylus profilometer to help overcome the various limitations of existing equipment – STM only works for conductive samples in a vacuum and the stylus profilometer damages the surface of samples[67]. The highly flexible AFM allows measurements to be conducted not just in vacuum, but in air or fluid

environments with minimal sample preparation. This flexibility thus allows the imaging of polymers and biological samples in their natural state, not just in vacuum where materials could become distorted[65].

Figure 2.8 shows the basic principles of AFM. A probe with a sharp tip is mounted at the end of a cantilever where the probe and the sample move relative to each other in a raster motion, line by line[65]. The force between the sample and the tip causes the cantilever to bend and this gets translated into topography measurement for the sample. This is the fundamental behind the basic AFM technique while different variations of it have evolved it into a highly versatile and popular scientific tool. The versatility of AFM allows it to not simply image the sample on the subatomic scale, but also quantitative measurements such as elastic modulus or force curves[65,68,69].
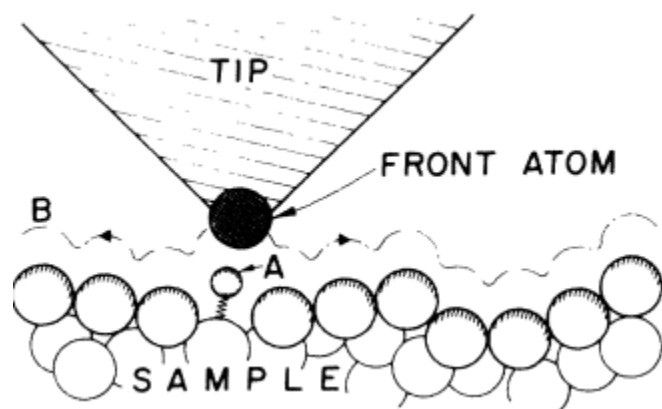
Figure 2.5 Schematic representing basic AFM operation, constant force between the sharp tip and sample was maintained while the tip moves along the contours of B adapted from Binnig et al.[67]

The original design had a STM piggy-backed onto the AFM, where the STM was used to detect deflection with extreme accuracy due to electron tunneling. However, the detection range was quite narrow and not suitable for practical purposes. Thus came the invention of an optical lever deflection method, where it uses a beam of laser to detect the deflection of cantilever[65–67]. Sometimes, a piezoelectric transducer is used to modulate the oscillation of cantilever. The beam

is reflected off the free end of the cantilever and is collected by an external displacement sensor, usually a photodiode that translates light into electrical signal[66]. As the probe raster the sample, digitization of the electrical signal happens simultaneously to produce the final AFM image. A proportional-integral-derivative (PID) feedback loop is used to monitor the system and adjust as necessary.
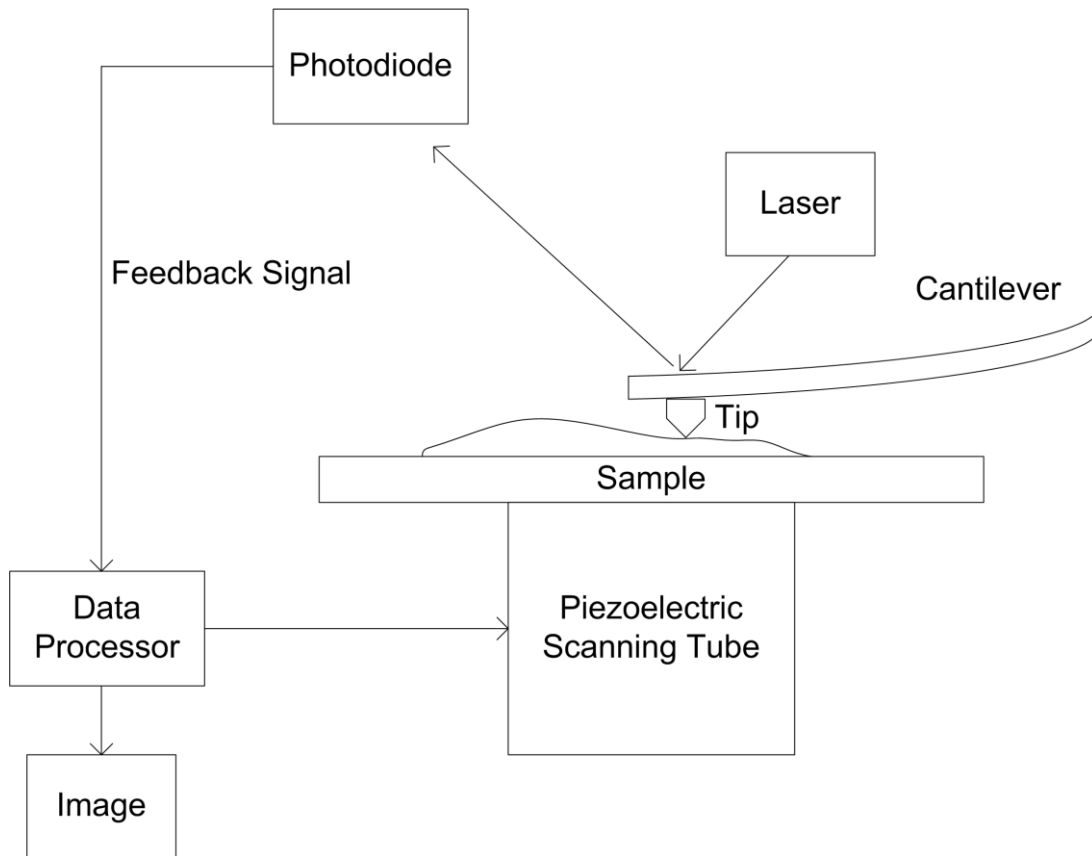
Figure 2.6 Schematic AFM setup

The specimen is typically mounted over a piezoelectric scanner with various configurations available[65]. The hollow tube scanner could be made of piezoceramic material and/or piezocrystal. The hollow tube scanner is able to extend in the x- and y-direction with the ability of distinct piezocrystal for each direction to address certain non-linearity problems such as hysteresis contributing up to 14% of uncertainty in reproduced images[65,70]. There are various imaging methods available depending on the objective and sample type. For simplicity, only three

common variations will be discussed here. Those three variations are contact mode, tapping mode, non-contact mode[65].

2.4.5.1 Contact Mode

Contact mode imaging is literally having the probe remain in contact with the sample at all times, whether as a result of constant force or variable force[65,67]. It is the simplest method and was the original mode used. On the force curve, contact mode is typically performed at a distance where the overall force interaction between the probe and sample is dominated by short-range repulsion[65]. The surface could be measured with the deflection of the cantilever or the feedback signal that is required to keep the cantilever a constant position through a feedback mechanism. In contact mode, the feedback mechanism monitors the vertical deflection whereas amplitude is monitored in tapping mode. As the cantilever is deflected, the feedback mechanism returns the cantilever to the original point, otherwise known as the set-point chosen by the experimenter[65]. The change in the deflection of cantilever is recorded as a function of the x- and y- directions and gets translated into the resulting topographical image. Contact mode can be used be image relatively flat surface in either air or liquid environment with the ease of operation. However, it has the potential to cause lateral damage to the probe or the sample due to either steep edges or adhesive or frictional forces[65,66]. For soft, easily deformable sample, dynamic modes of imaging such as tapping mode or non-contact mode should be considered.

2.4.5.2 Tapping Mode

In order to address the aforementioned drawbacks of contact mode, tapping mode or dynamic contact mode was developed. It is the most common mode used in air or liquid environment, as it is able to prevent the tip of the probe sticking to the sample while keeping the tip close enough to measure short range forces[65]. Aided by the piezoelectric transducer (other methods are possible such as magnetic field or modulated laser beam heating), the cantilever oscillates at or close to its resonant frequency[71]. The oscillation amplitude typically varies from a

couple of nm to 200 nm, which causes the probe to bounce up and down while repeatedly engage and disengage with the sample[68]. As the probe gets closer to the surface, repulsive forces such as Van der Waals, dipole-dipole interactions reduce the amplitude of oscillation. With the use of a feedback loop to maintain a constant amplitude, topographical information can be obtained[65]. The intermittent contact between the probe and the surface ultimately produces the image. Although the peak forces applied in tapping mode is greater than contact mode, the short duration actually reduces the damage to the sample surface and the tip. This thus allows the visualization of monolayer materials with proper operating parameters[72,73].

2.4.5.3 Non-Contact Mode

Non-contact mode is very similar to tapping mode, except the cantilever is oscillated at a smaller amplitude compared to tapping mode and the tip of the cantilever does not touch the sample. An identical feedback loop is used to prevent the probe from touching the surface. Theoretically, this is the best mode to use in order to obtain high quality images on the atomic scale[65]. In practice, the water layer on top of the sample may be thicker than the Van der Waals. Thus making detection almost impossible along with the possibility of tip attachment to the water layer, which will in turn degrade the image quality.

In order to prevent damaged to the sample, especially the thin nanosheets, tapping mode was used for the scans.

2.4.5.4 Equipment

In order to prepare the samples for AFM, approximately 10 µL of IPA/water co-solvent with the exfoliated material was pipetted and drop-casted onto the clean-peeled mica wafer before letting it dry under room conditions for 4 days. Once the co-solvent completely evaporates from the mica wafer, deionized water was used to rinse the surface repeatedly to wash away the excessive solvent and materials. The mica wafer is then attached to a coin sized steel plate for

characterization under the AFM. A similar procedure was used to prepare samples exfoliated with organic solvent, with the addition of letting it dry in the oven at 50°C for 4 days instead of at room temperature. Icon AFM made by Bruker and Bruker DNP-10 tip was used for the scans. The experimental setup is shown in Figure 2.7.
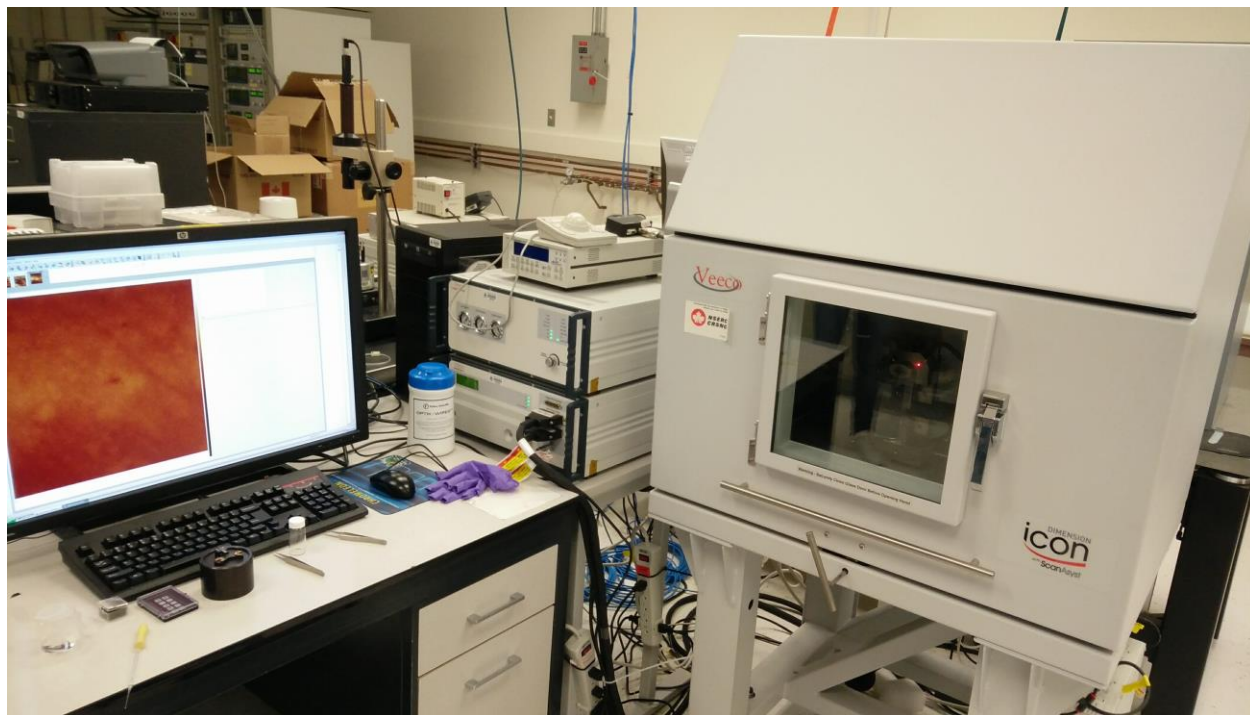
Figure 2.7 Experimental setup of Icon AFM

2.4.6 Electrochemical Measurements

The three-electrode electrochemical setup is shown in Figure 2.8 with the sample drop casted onto the glassy carbon rotating disk electrode as the working electrode, 52 mesh platinum gauze (50×75 mm, 37.5 cm²) as the counter electrode and a saturated KCl Ag/AgCl as reference electrode. A three-electrode setup with a reference electrode was used because we are only interested in the reduction half reaction of electrolysis, hydrogen evolution reaction. A reference electrode essentially standardized the other half of the cell which we are not interested in (i.e. constant potential). In the hydrogen evolution reaction experiments, a saturated Ag/AgCl

reference electrode was used and its potential with respect to the Reversible Hydrogen Electrode (RHE) is shown as follow:

Potential (V vs. RHE) = Applied Potential (V vs. Ag/AgCl) + 0.059×pH + $E^o_{Ag/AgCl}$ (2-6)

where $E^o_{Ag/AgCl}$ is 0.197 V and pH is close to zero in 0.5M H_2SO_4 electrolyte solution. Mili-Q water of 18.2 MΩ×cm at 25°C was used to dilute the concentrated sulfuric acid (H_2SO_4) into 0.5 M H_2SO_4 which was subsequently used as the electrolyte for the experiment. An acidic electrolyte such as 0.5 M H_2SO_4 was selected due to its ability to provide an abundant supply of hydronium ions (H^+) to facilitate hydrogen reduction through water electrolysis[74]. Prior to conducting any measurements, the electrolyte was purged with nitrogen for at least 30 minutes and a continuous flow of nitrogen was maintained throughout the experiments. The objective of purging with nitrogen (or any inert gas) was to ensure accurate measurement of the redox potentials of the half reactions. In addition, the presence of dissolved oxygen may contribute to the cathodic measurement due to the reduction of oxygen at negative potentials. Removal of the dissolved oxygen gas or any other gases that may cause interference was achieved through continuous purging. All electrochemical measurements were conducted at room temperature in a jacket rotating disk electrode (RDE) cell using an Autolab Potentiostat (PGSTAT302N) purchased from Metrohm Autolab B.V. with the Nova 2.0.1. software. In a potentiostat, the voltage was varied between the working electrode and the reference electrode. The resultant current between the working electrode and the counter electrode were recorded. Samples were dropped casted onto a glassy carbon electrode RDE. Linear sweep voltammetry (LSV) was conducted from 0.1 V to -0.7 V (vs. RHE) while the kinetics of the reaction was measured when RDE was set to 2,000 RPM.
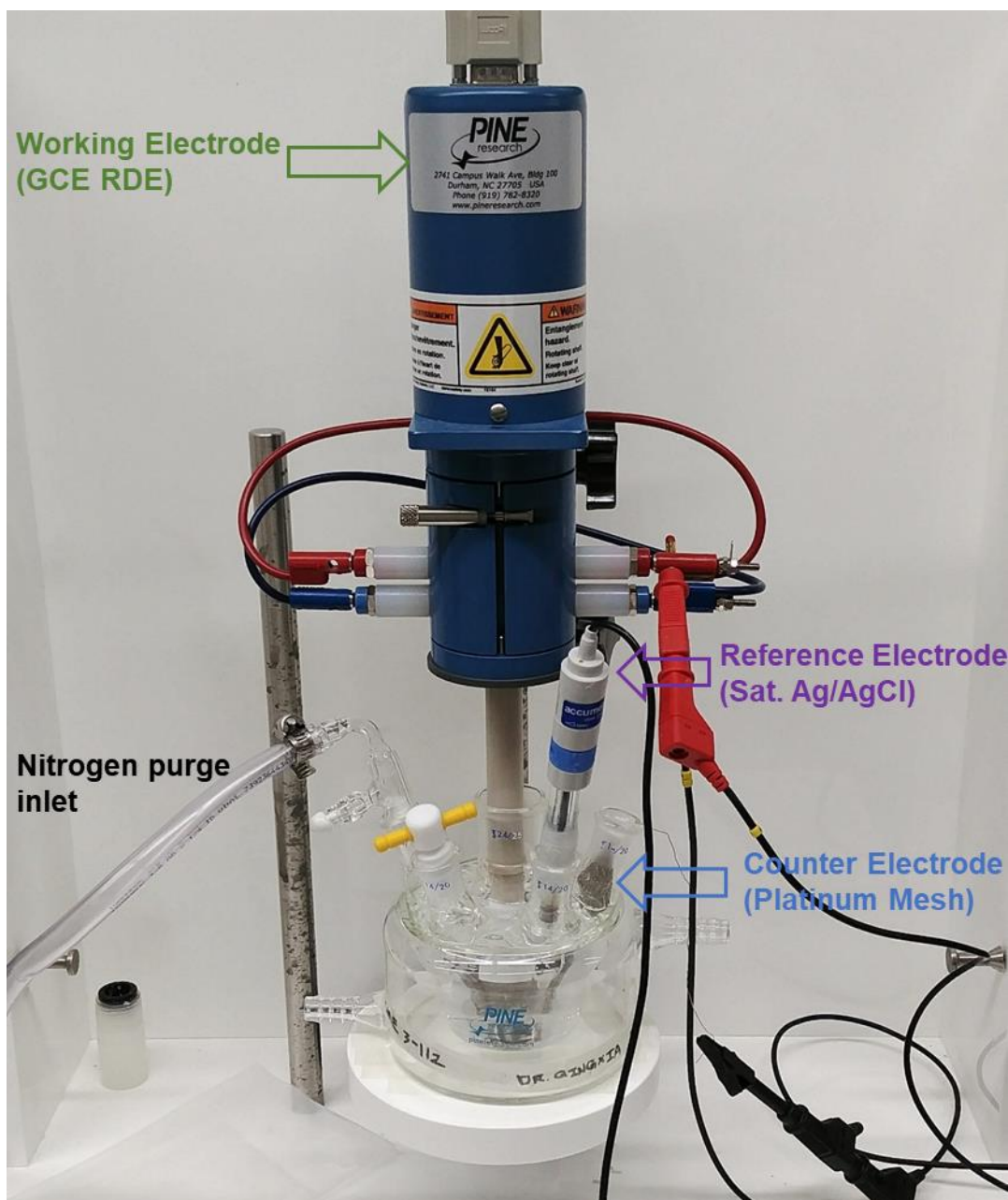
Figure 2.8 Three electrodes setup for the electrochemical scans (potentiostat not shown)

Rotating disk electrode (RDE) with ChangeDisk RDE tip and glassy carbon electrode (GCE) disk insert (5.0 mm diameter) were purchased from Pine Research. The GCE was polished with 0.05 μm alumina and fine micro cloth polishing paper purchased from Buehler. The activation of GCE was achieved by repeated cyclic voltammetry (CV) scan in degassed (continuous nitrogen purge) 0.5 M H_2SO_4 in between 1 V and -1 V at a scan rate of 50 mV/s. After good overlap was

achieved along with an approximately zero slope in the center region, the GCE was then proceeded to be tested in 1 mM ferrocyanide in 1 M KCl solution. Similar to before, the test solution of 1 mM ferrocyanide in 1 M KCl was degassed and a continuous nitrogen purge was maintained while the measurements were conducted at a scan rate of 100 mV/s in between 1 V to -0.2 V. The activation was considered complete when the ΔE_p (the difference between the forward and reverse peaks on the potential axis) was subjectively close to the reversible reaction theoretical value of $(58/p)$ mV, where p is the number of electrons involved in the redox reaction.

Samples for the electrochemistry experiments were prepared by mixing 2 mg of the material in 1 mL of 45/55 vol% 2-propanol (IPA)/DI water solution and 25 µL of Nafion D-520 with $\geq$ 1.00 meq/g exchange capacity within a 5 mL vial followed by subsequent sonication in the ultrasonic bath for 30 minutes to achieve a homogenous mixture. There should no sedimentation at the bottom of the vial. In order to drop-cast the sample onto the GCE (geometric surface area of 0.196 cm^2), the equivalent µL of the solution required to achieve effective catalyst loading of 0.13 mg/cm^2 was pipetted carefully onto the cleanly polished GCE and left to dry under room conditions for the IPA/DI water exfoliated MoS_2. For the NMP exfoliated samples, an identical procedure was used with the exception of 0.026 mg/cm^2 as the effective loading capacity. After drop-casting the sample onto the GCE, the GCE was placed in a vacuum oven at 40 °C to evaporate off the organic solvent.

In Chapter 2, the material preparation, synthesis and characterization techniques using organic solvent and co-solvent of isopropanol/water were discussed. To summarize, liquid phase exfoliation was the technique used to exfoliate the natural MoS_2 mineral in either organic solvent or co-solvent of isopropanol/water. The exfoliation process was performed in an ultrasonic bath, an ultrasonic probe, or a combination of both. Centrifugation was used to separate the exfoliated material from the unexfoliated material. The supernatant obtained at 12800G RCF was lyophilized before further characterization.

Chapter 3 Results and Discussion

3.1 Overview

This chapter is split into three sections. The first section contains a brief discussion around the material characteristic of the MoS_2 mineral. The second section will primarily focus on the as-exfoliated MoS_2 nanosheets using the co-solvent of IPA/water after liquid cascade centrifugation as well as that of the natural mineral MoS_2. In the third section, exfoliation of natural mineral MoS_2 with organic solvents, primarily n-methyl-2-pyrrolidone (NMP) will be discussed. In both sections, the materials were characterized using the experimental methods that were discussed in Chapter 2. The objectives were to determine i) whether there was a change in composition of the exfoliated material after processing; ii) thickness of the exfoliated MoS_2 nanosheets; and iii) the hydrogen evolution reaction performance via electrochemistry experiments.

3.2 MoS₂ Mineral Analysis

3.2.1 X-Ray Powder Diffraction

Figure 3.1 shows the XRD pattern of the MoS_2 mineral powder prior to liquid phase exfoliation with their corresponding Miller indices. The MoS_2 mineral was used as it is without further treatment, the XRD data presented above is the raw data without any noise removal or curve smoothing. The Miller indices [(002), (100), (101), etc.] were obtained by comparing the experimental results with the supplied ICDD Powder Diffraction File database (Powder Diffraction File #37-1492) along with the *a*-spacing lattice constant. There was a good match of the MoS_2 mineral pattern with the as-provided MoS_2 2H phase reference data[75]. No peak broadening was observed, thus confirming the crystallinity of the material. Figure 3.2 shows the XRD data of MoS_2 powder purchased from Sigma Aldrich, the peaks are identical to what was observed in the mineral MoS_2 with slight variations in peak intensities. This is expected as the Aldrich MoS_2 is synthesized from chemical vapor deposition with molybdenum and sulfur precursors whereas the natural MoS_2 mineral will have trace amounts of impurities. It is

important to keep in mind XRD by itself cannot identify the chemical elements present in the material, in addition to the 2% detection limit for materials. Thus, there could be trace levels of contaminants within the mineral even though the above XRD pattern shows a good match to the 2H MoS$_2$.
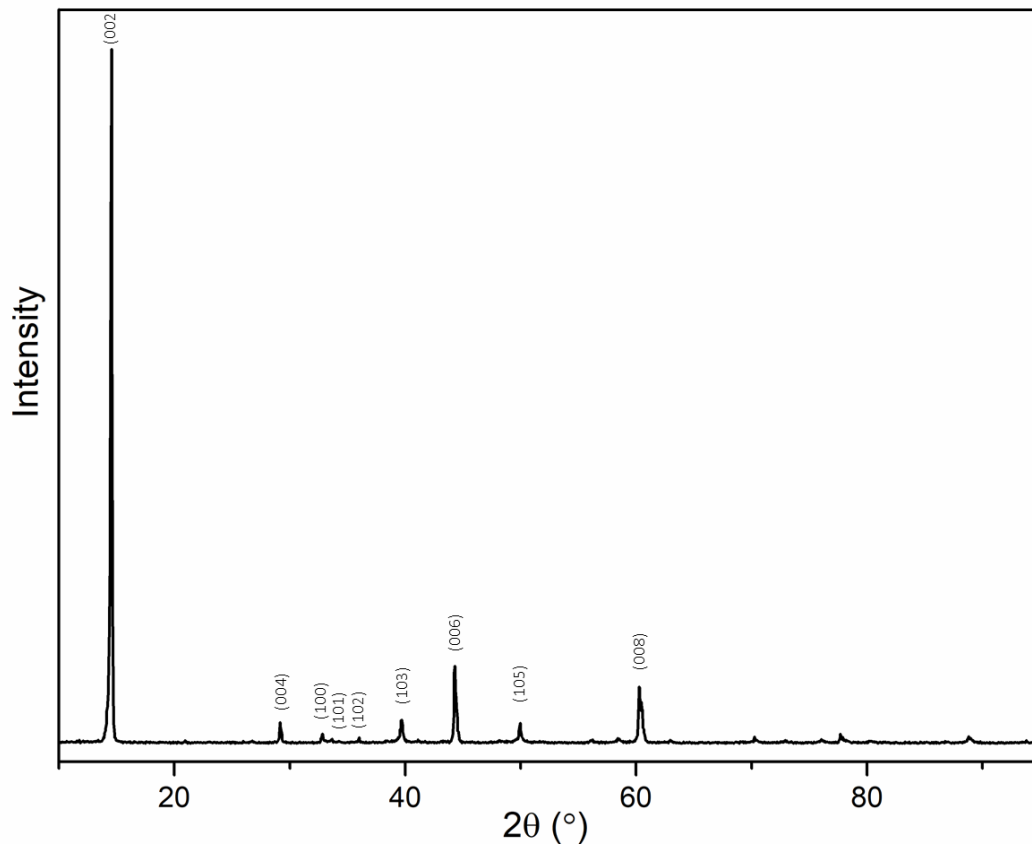
Figure 3.1 XRD pattern of bulk phase MoS$_2$ mineral with Miller indices shown
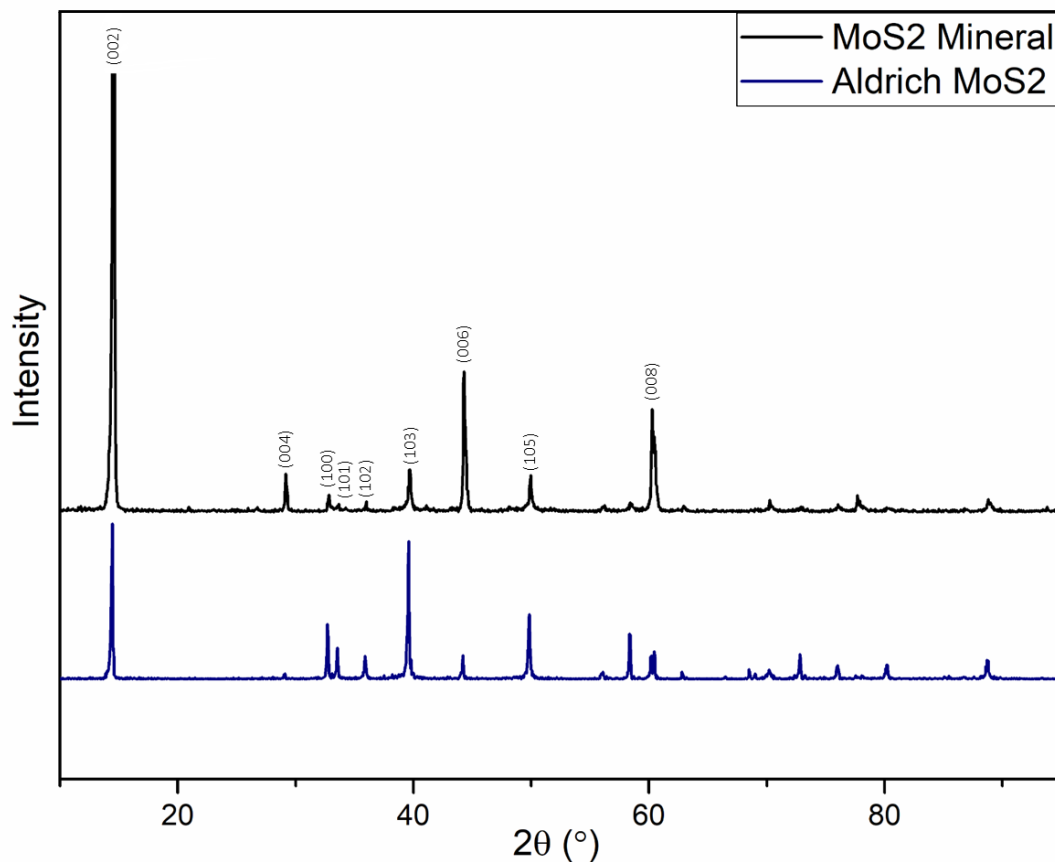
Figure 3.2 XRD comparison of MoS$_2$ purchased from Aldrich to natural MoS$_2$ mineral

3.2.2 Optical Microscope

Figure 3.3 shows the optical microscopy images collected for the top layer of MoS$_2$ purchased from Sigma-Aldrich when dispersed in water, MoS$_2$ mineral sample and the top layer MoS$_2$ mineral sample when dispersed in DI water. A fluorescence filter was applied to bring out the contrast between the natural mineral and the unknown source of contaminants. In the Aldrich sample, it was clear everything was uniform without any outliers, this is expected as the sample purchased from Sigma-Aldrich was about 99% purity. However, in the natural MoS$_2$ mineral that was used as the starting material for all the subsequent experiments, there appears to be various rectangular shape of unknown material (only one view is shown here, but they are present in any random selection of view). In order to gain a better look at this, the MoS$_2$ mineral and the Aldrich

sample were both dispersed in DI water with the top layer collected. A freeze dryer was used to remove the water. The top layer Aldrich sample was identical to the original sample with uniform particles. Whereas the collected top layer for MoS_2 mineral looked completely different. Figure 3.4 provides an optical microscope with fluorescence filter view of the top layer for MoS_2 mineral. It was clear that there are abundant amount of needle-like structures within the sample. The same observation was made under the transmission electron microscope for the samples that was processed with bath and probe ultra-sonication followed by liquid cascade centrifuge, except the needle-like structure was much smaller, on the scale of approximately 100 nm compared to the hundreds of microns here. Likewise, scanning electron microscope with energy dispersive X-ray identified the needle-like structures to be predominantly of sulfur, calcium and molybdenum.
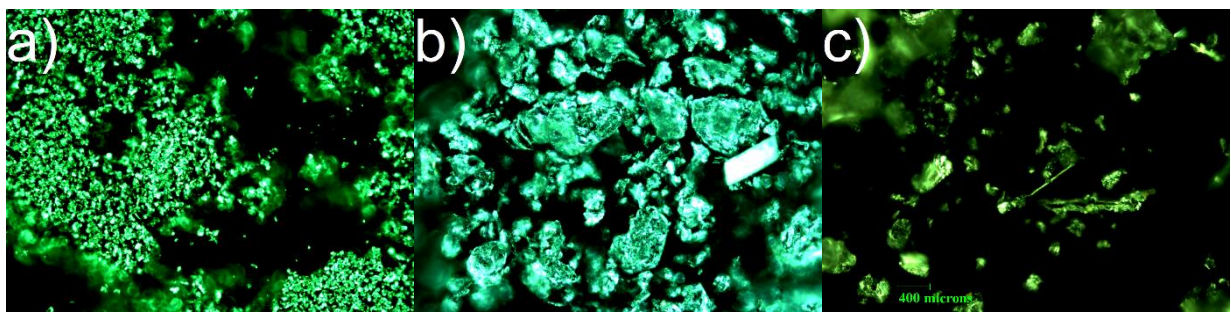
Figure 3.3 Optical images at 20X magnification of a) top layer Aldrich MoS_2 b) MoS_2 mineral and c) top layer MoS_2 mineral with a fluorescence filter for contrast enhancement, scale bar is the same for all images

Figure 3.4 Top layer of MoS_2 mineral where the needle like shapes were suspected to be

contaminants (primarily calcium)

3.2.3 Scanning Electron Microscopy (SEM)

Scanning electron microscopy (SEM) with energy dispersive X-ray (EDX) was used for elemental analysis of the MoS_2 natural mineral and the top layer of MoS_2 mineral after floating it in water. The top layer of MoS_2 mineral was selected because that is where the impurities are suspected to reside. The NMP exfoliated sample wasn't tested under SEM EDX due to the low yield rate from liquid phase exfoliation. The top layer of MoS_2 mineral should provide an objective characterization of the needle-like structures that was shown under the optical microscopy. Figure 3.5 and 3.6 show the SEM image for the natural MoS_2 mineral and top layer, respectively. The corresponding points and area analysis of the elemental compositions are shown in Table 3.1 with oxygen removed. In the natural MoS_2 mineral, the composition are obtained from EDX mapping with a S/Mo atomic ratio of 2.06, which is a good match to the theoretical value of 2. However, the impurities/contaminants make up approximately 3 wt% of the entire sample. Therefore, it could be said that the natural MoS_2 mineral is 97% pure by weight. However, point analysis of the needle-like structures actually showed excess amount of calcium atoms present. The weight

percentage of calcium present in the needle-like structures from point analysis are actually more 5 times higher compared to the area analysis. Even though molybdenum was present, calcium was the dominating atom behind sulfur. This thus resulted in a skewed S/Mo ratio of 4.35. Therefore, the needle-like structures observed under optical microscopy and within the TEM after exfoliation are actually not pure MoS_2, rather MoS_2 containing contaminants primarily made up of calcium.
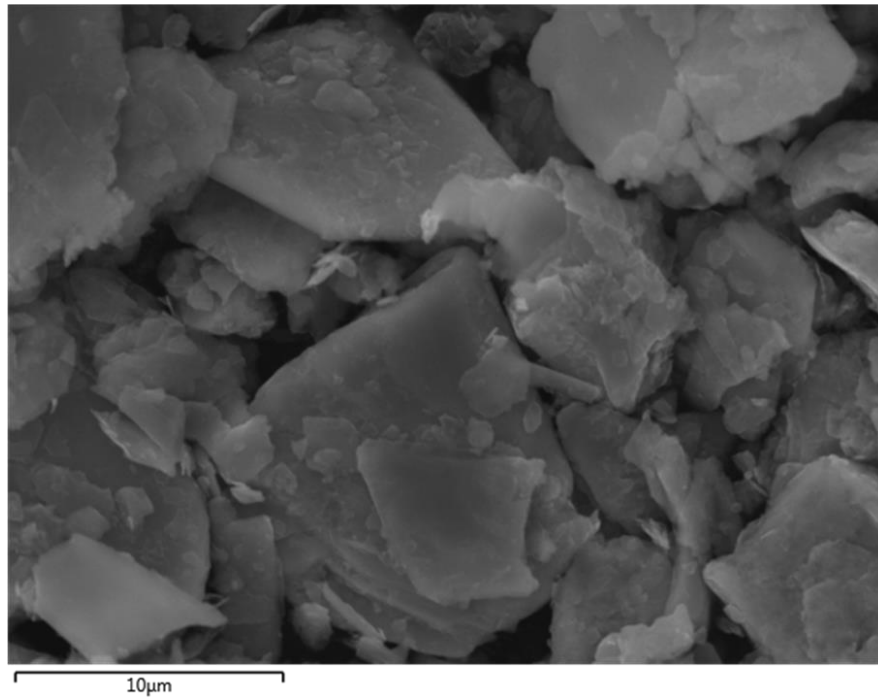
Figure 3.5 SEM of natural MoS_2 mineral
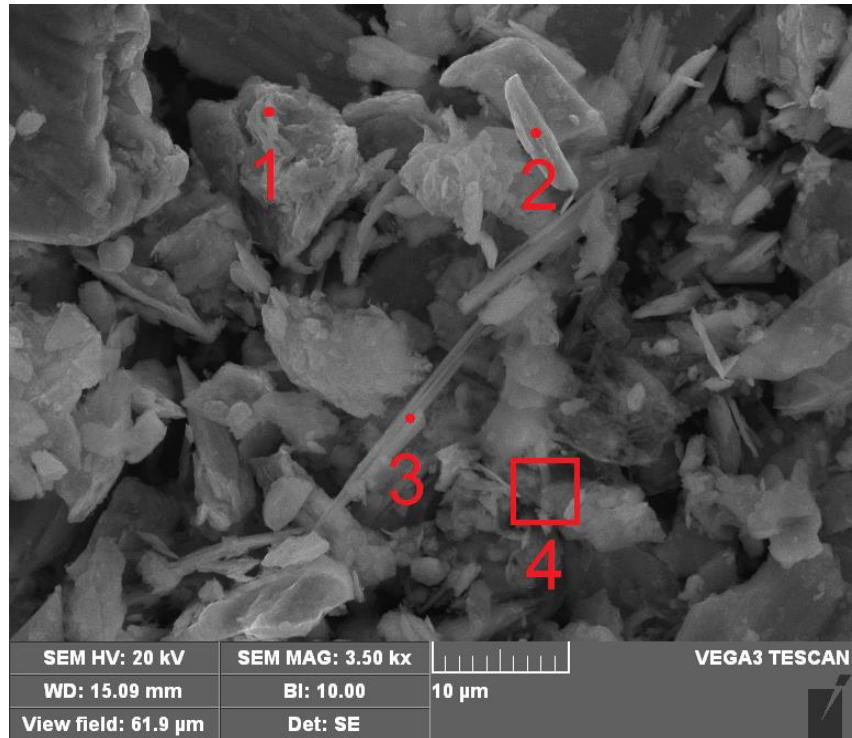
Figure 3.6 SEM of the collected top layer MoS_2 mineral

Table 3.1 Elemental analysis of points, area and EDX mapping displayed as atomic percentages

	Point 1	Point 2	Point 3	Area 4	Natural MoS_2 Mineral
Al	-	3.06	2.32	4.80	0.52
Si	-	6.20	3.09	7.63	0.87
S	63.18	57.00	50.50	50.86	65.00
Cl	-	-	7.03	3.06	0.36
K	-	-	-	1.75	0.10
Ca	-	-	22.53	3.91	0.10
Fe	3.03	8.04	2.93	4.41	1.49
Mo	33.79	25.70	11.60	23.58	31.56
S/Mo	**1.87**	**2.22**	**4.35**	**2.16**	**2.06**

3.3   Isopropanol (IPA)/Water Exfoliation

MoS_2 nanosheets were obtained from liquid phase exfoliation of MoS_2 mineral in a 45 vol% IPA/DI water (18.2 MΩ·cm at 25°C) mixture. Centrifugation was used to separate the nanosheets from the unexfoliated material. The removal of the solvent was achieved by subsequent freeze-drying of the 12800G RCF supernatant. The supernatant at 12800G RCF was selected because that is where the material with the lowest density should reside along with thinner MoS_2 being associated with higher centrifugation speed[76]. Residual solvent will not affect electrochemistry performance as an identical mixture was used to prepare the nanosheets for the electrochemistry experiments. In the following sections, the exfoliated nanosheets are characterized with UV-vis, HR/TEM, AFM and SEM with EDX mapping while demonstration of a potential application is shown through the hydrogen evolution reaction.

3.3.1   Hydrogen Evolution Reaction

Prior to proceeding any further, the terms overpotential and onset potential should be clarified in case of any confusion. Overpotential at 10 mA/cm^{2} will be used to compare the HER catalysts activities as this is the current density expected to achieve 12.3% efficiency in solar to hydrogen conversion equipment that is expected to be cost competitive[13]. Onset potential is where a sharp increase in the reduction current is experienced, otherwise known as the starting point of reactions. This can be determined by reading off the semi-log Tafel plots, where overpotential is plotted as a function current density. The inflection point between the linear portions of the Tafel plots and the non-linear portion could be used as an indicator of onset potential. In order to obtain the Tafel slope and exchange current density, the linear portion of the Tafel plot is fitted to the Tafel equation[77].

$$\eta = a \log (j/j_o) \tag{3-1}$$

where η is the overpotential, a is the Tafel slope, j is the current density, and j_o is the exchange current density. The above equation can be expressed in the linear form of $y = mx + b$.

$$\eta = a \log (j) - \log (j_o) \tag{3-2}$$

The linear form of the Tafel equation is then fitted to the linear portion of the Tafel plot in order to obtain Tafel slope and exchange current density – the rate of oxidation and reduction at equilibrium, which serves as a good indicator of activity[35,38,48]. With that said, both the overpotential and onset potential will be used in conjunction with metrics such as Tafel slope and exchange current density to benchmark the performance of HER catalysts.

The ability of natural MoS_2 mineral exfoliated nanosheets to catalyze HER was assessed in a nitrogen-saturated 0.5 M H_2SO_4 electrolyte. The reported data here are uncompensated for Ohmic and mass-transport overpotentials. The mass-transport limitations should not be a factor here as the working electrode is very small with respect to the electrolyte. Ohmic losses are somewhat mitigated by minimizing the distance between the working electrode and the reference electrode. Under a cathodic current, the true potential of the working electrode is actually less negative than the specified potential, this will translate in a lower overpotential value in general. Thus, the experimental results can be viewed as "worst case scenario" in a sense.

The criteria used for assessment was made based on overpotential – the difference between applied potential and standard potential at 10 mA/cm^{2} and Tafel slope. The onset potential is also used for comparison, albeit not as accurate as it is more subjective. Catalyst loading on the electrode plays a key role empirically on overpotential and current density, as higher loadings correlate with lower overpotential for non-noble element[78]. For the empirical data obtained below, a catalyst loading of 0.13 mg/cm^{2} was used. Figure 3.7 show the linear sweep voltammetry (LSV) curves for the exfoliated MoS_2 nanosheets compared to the unexfoliated mineral and platinum wire. The Tafel plot is shown in Figure 3.8 and a summary table of the onset potential, overpotential and Tafel slopes is shown in Table 3.2. A noticeable enhancement in the catalyst performance is observed as the onset potential, overpotential and Tafel slope of the exfoliated MoS_2 nanosheets all decreased for the better compared to the unexfoliated material.

For the exfoliated MoS_2 nanosheets, a Tafel slope of 112 mV/dec and an exchange current density of 3 µA/cm² were obtained, which is comparable to literature results[48,79]. By definition, Tafel slope is able to tell us the amount of increase in overpotential is required to increase the reaction rate by a factor, a smaller value is advantageous for practical applications. It is possible to deduce the mechanism and rate-limiting step by matching Tafel slope to the Volmer-Heyrovsky-Tafel equations, but the calculations may contain some degree of uncertainty as the assumptions made do not universally hold[15,80]. The proposed mechanisms for HER in acidic solutions are as follow[14,35]:

Volmer (120 mV/dec): $\qquad$ $H^+ + e^- \rightarrow H_{ad}$ $\qquad$ (3-3)

Heyrovsky (40 mV/dec): $\qquad$ $H^+ + H_{ad} \rightarrow H_2$ $\qquad$ (3-4)

Tafel (30 mV/dec): $\qquad$ $H_{ad} + H_{ad} \rightarrow H_2$ $\qquad$ (3-5)
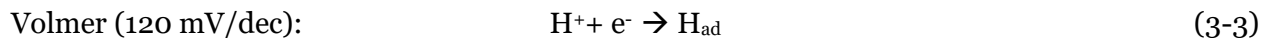
The two possible mechanisms are Volmer-Heyrovsky, where a fast discharging step in (3-3) is proceeded by a slow desorption in (3-4) which results in a Tafel slope of 40 mV/dec; and Tafel-Volmer where a similar fast discharging step in (3-3) is proceeded by a slow combination reaction in (3-5) which results in a Tafel slope of 30 mV/dec. However, in this experiment, the obtained Tafel slope do not match with the standard values for the rate-determining step. The 112 mV/dec Tafel slope for the exfoliated MoS_2 nanosheets suggests that the HER reaction proceeds through a Volmer-Heyrovsky mechanism, where the Volmer reaction is the rate determining step with low surface hydrogen coverage (can be close to zero) due to fast consumption of adsorbed hydrogen followed by subsequent desorption of hydrogen[15,38,81]. The basal plane of MoS_2 is catalytically inert whereas the catalytic activity is commonly associated with sulfur edges[82]. The optimum binding energy for the intermediate happens when the adsorbed hydrogen bonds neither too tightly or loosely[82,83]. From literature, DFT calculations have shown that the fractional coverage of adsorbed hydrogen is ¼ on MoS_2 edge sites, this is in favor of the Volmer-Heyrovsky mechanism[82,83]. If Volmer reaction is indeed the rate determining step, then the kinetic rate constant would be

dependent on the applied potential as this is an electron transfer step[15]. On the contrary, if the surface coverage of protons is quite high, it is also possible that Heyrovsky reaction is the rate determining step.
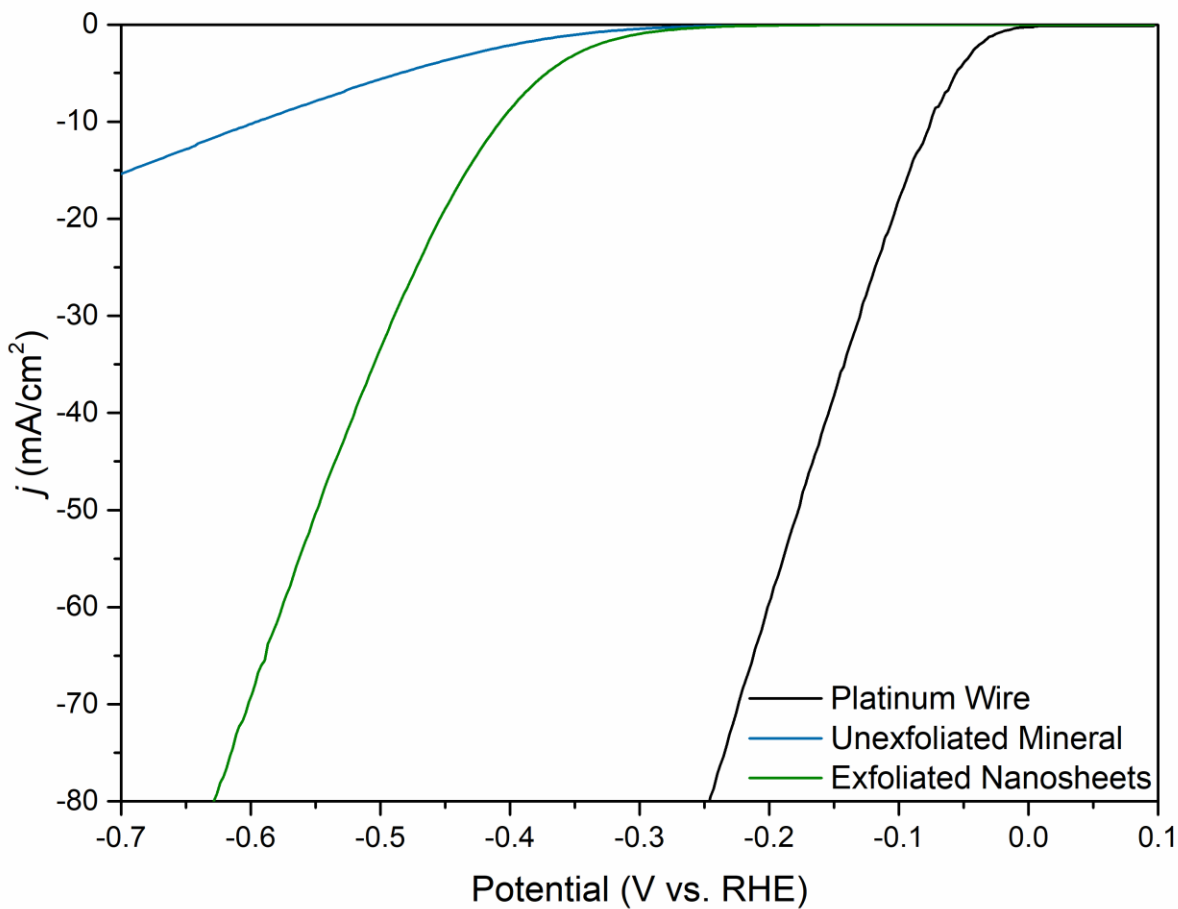
Figure 3.7 LSV comparison of unexfoliated mineral, exfoliated MoS_2 nanosheets against

platinum wire
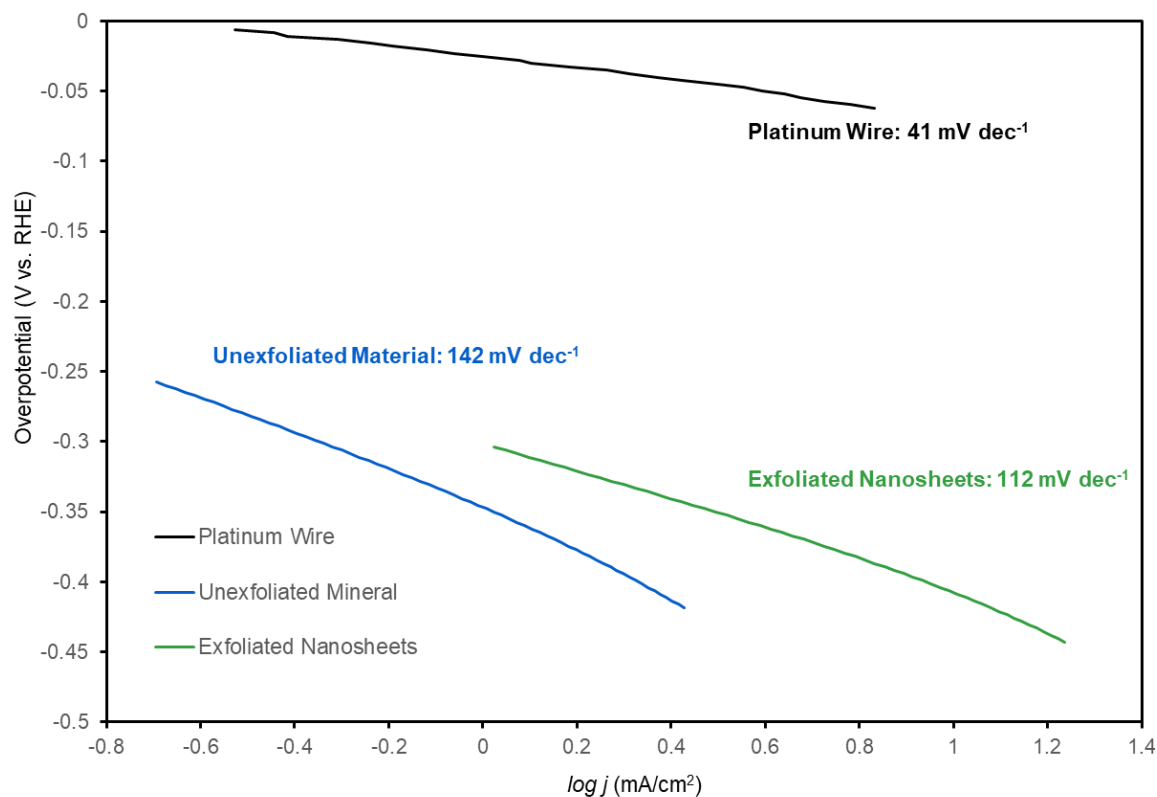
Figure 3.8 Tafel plots of unexfoliated MoS$_2$ versus exfoliated MoS$_2$ nanosheets

Table 3.2 Tafel slope, Onset potential and Overpotential (vs. RHE) Summary

	Onset potential [mV]	Overpotential (at 10 mA/cm²) [mV]	Tafel Slope [mV/dec]
Platinum wire	-13	-77	41
Unexfoliated	-258	-595	142
MoS$_2$ nanosheets	-201	-407	112

One of the concerns facing non-noble metal catalysts is the possibility of corrosion when used as HER catalysts in acidic media. In order to evaluate the long term stability of the catalyst, a continuous scan of 400 runs was conducted. Figure 3.9 shows the polarization curve with a scan rate of 50 mV/s with very good stability of the catalyst. The overpotential at 10 mA/cm² and onset

potential have shifted by -5 mV and -7 mV, respectively. The shifts are negligible as Figure 3.10

shows the Tafel plots, where the Tafel slope remained the same after 400 runs. Since Tafel slope

is obtained by fitting the linear portion of the semi-log Tafel plots with a first order linear equation,

there is naturally some degree of uncertainty. The R-squared value can provide us with how good

of a fit the linear equation is to the data. However, using a different linear portion of data with 50%

overlap to the as-obtained data, a difference of 0.005 in R-squared was obtained in the fit. This

subsequently resulted in a shift of Tafel slope to 98 mV/dec vs. 112 mV/dec, equivalent to 13%

difference. In turn, the exchange current density also decreased by a factor of 3. To conclude, the

Tafel slope and exchange current density are highly subjective depending on which linear portion

of the data was used. In this experiment, the liquid phase exfoliated MoS_2 nanosheets

demonstrated an increase in Tafel slope from the unexfoliated material, with good stability after

400 runs and an exchange current density of 3 $\mu A/cm^2$. The hydrogen evolution reaction in this

thesis was hypothesized to proceed through a Volmer-Heyrovsky mechanism where the Volmer

reaction is the rate determining step. This was in line with previous literature results. Albeit the

overpotential, Tafel slope and exchange current density are all higher than the HER benchmark

platinum wire, there was definitely a noticeable enhancement compared to the unexfoliated MoS_2

mineral.
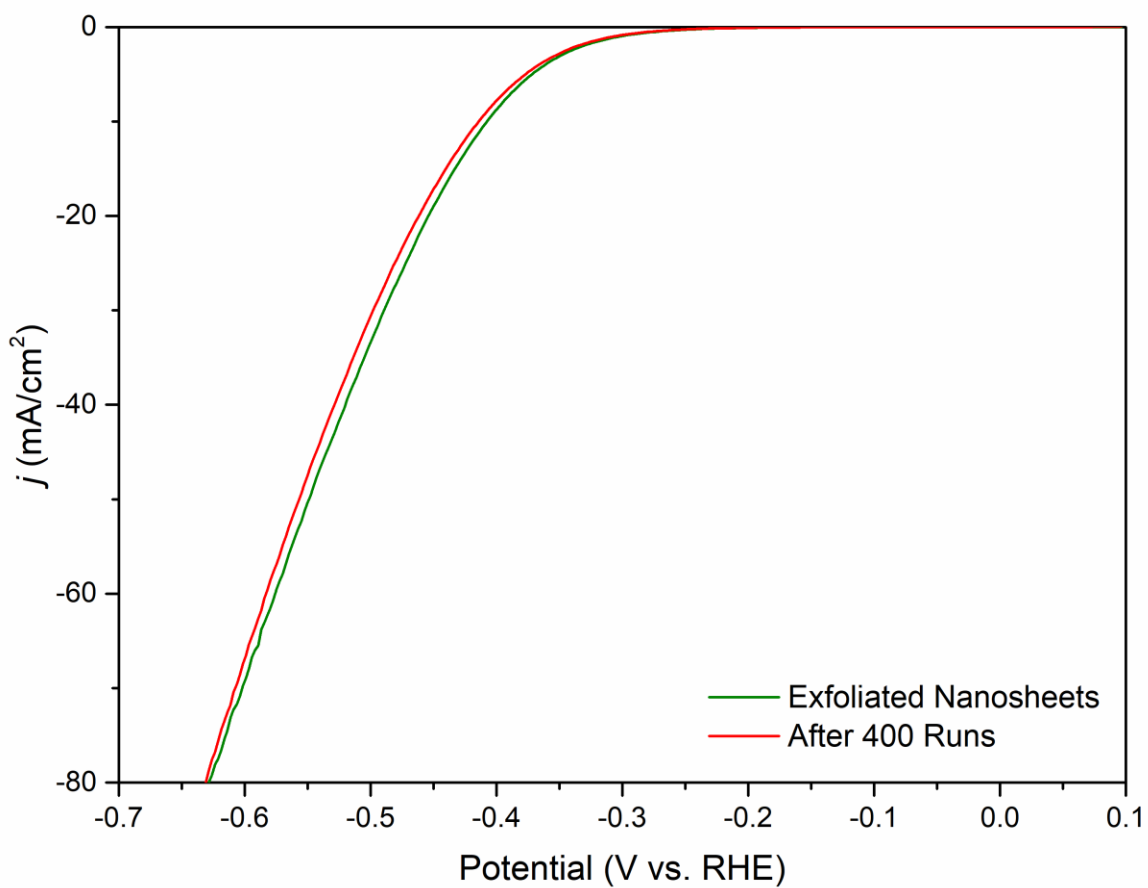
Figure 3.9 Polarization curves demonstrating stability of the exfoliated MoS_2 nanosheets after

400 runs
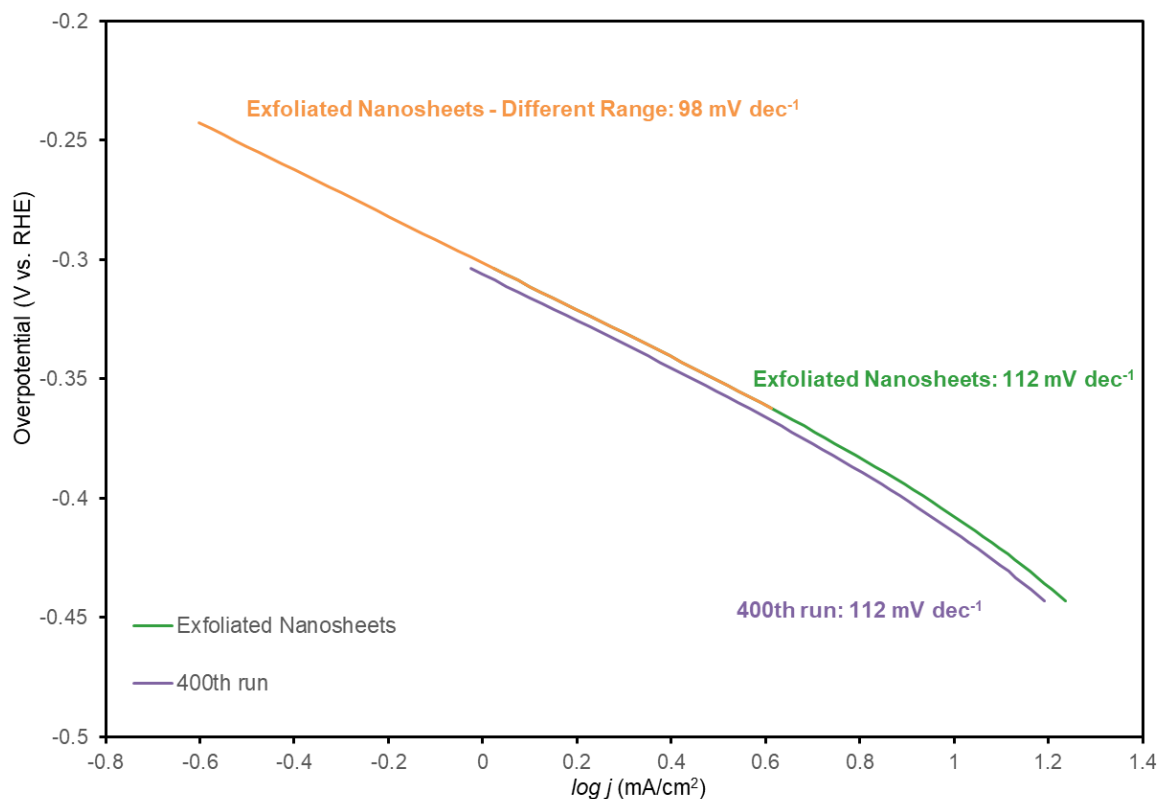
Figure 3.10 Tafel plot for the exfoliated MoS2 nanosheets

3.3.2 Atomic Force Microscopy (AFM)

In order to determine the height of the exfoliated MoS_2 nanosheets, tapping mode AFM was used to determine the heights of the drop-casted MoS_2 nanosheets immobilized on mica. For comparison purposes, the height benchmark for one layer of MoS_2 is approximately 0.615 nm, with n multiples of that signifies n number of layers[84,85]. A cut-off mark of 0.5 nm was used, anything below 0.5 nm was not counted in the statistical height count. When the height difference was not a multiple of 0.615 nm, a cut-off of 0.3 nm plus the next fewest layer was used. For example, if for some reason the height measurement is 0.9 nm that would be categorized under monolayer whereas 1.0 nm would be categorized under two layers and so on. A possible reason for the deviation from the theoretical value of 0.615 nm could be an implication of adsorbents on its surface, thus resulting in higher thickness than theoretical[84,85]. Figure 3.11 shows the AFM

results along with a blank mica sample while Figure 3.12 shows the statistical count of the equivalent number of layers by hand. For the blank mica sample, the surface is relatively smooth. It can be seen that the majority of the nanosheets falls within the monolayer and few layers region (~90%) with monolayer consisting of 60% of the total count. The obtained equivalent layer counts was obtained by manual counting of height in three areas of identical size (3.8 by 3.8 μm).
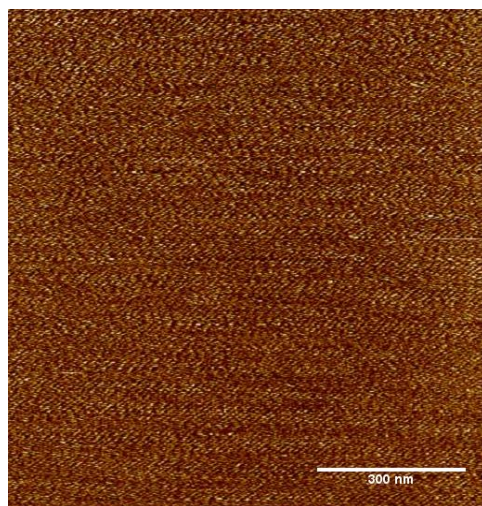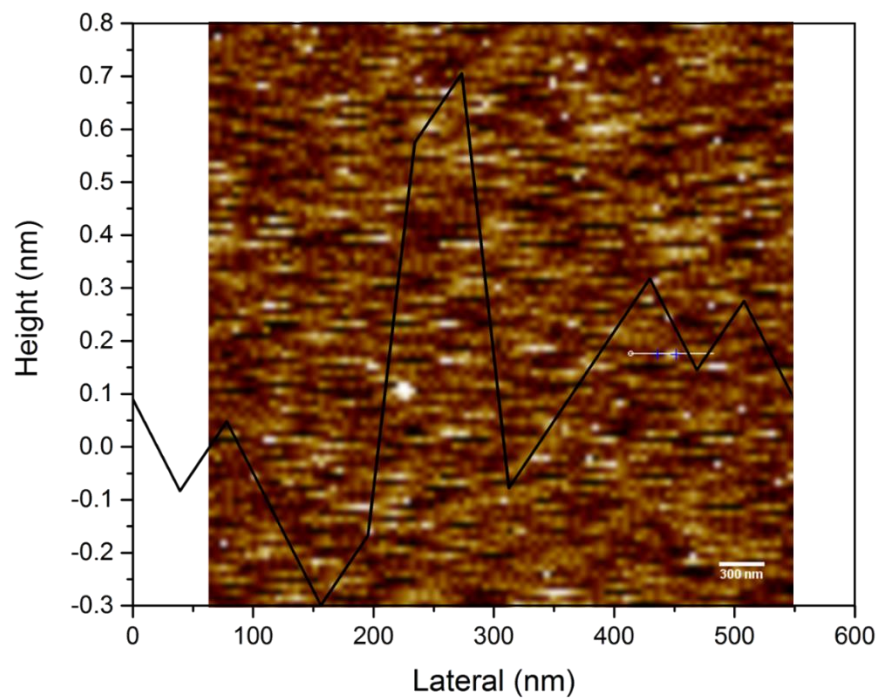
Figure 3.11 AFM height image 3.8×3.8 μm area of MoS₂ nanosheets immobilized on mica

substrate (top), blank mica sample 1×1 μm (bottom)
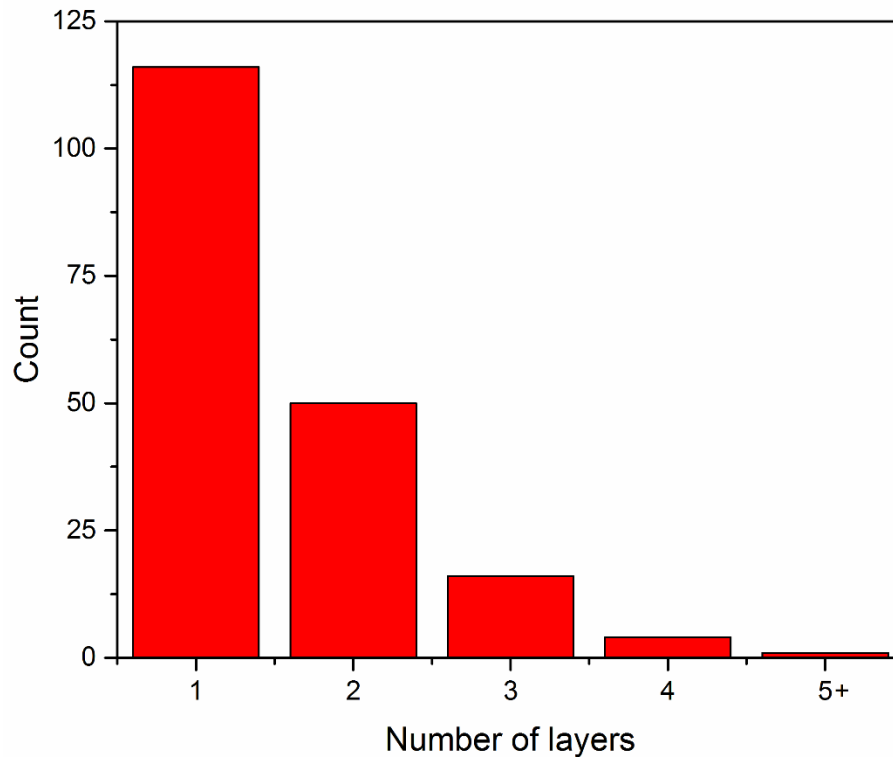
Figure 3.12 Equivalent number of MoS_2 layers obtained by manual counting

3.3.3 Transmission Electron Microscope (TEM)

Figure 3.13 and 3.14 show the TEM, HRTEM and SAED for the exfoliated MoS_2 nanosheets obtained from the supernatant at 12800G RCF. A d-spacing of 2.61 Å was obtained from the selected area electron diffraction (SAED) pattern, which matches well with the XRD pattern, particularly the family lattice plane (101). Additional images for the nanosheets are shown in Figure 3.15 with most of the nanosheets observed at around 200 nm by 200 nm. The hexagonal atomic structure of 2H MoS_2 was quite noticeable and corresponded well to previous observations[86]. The various inconsistencies in the HRTEM image (i.e. the lack of hexagonal structure in the top left corner) could be attributed to the layered structure.
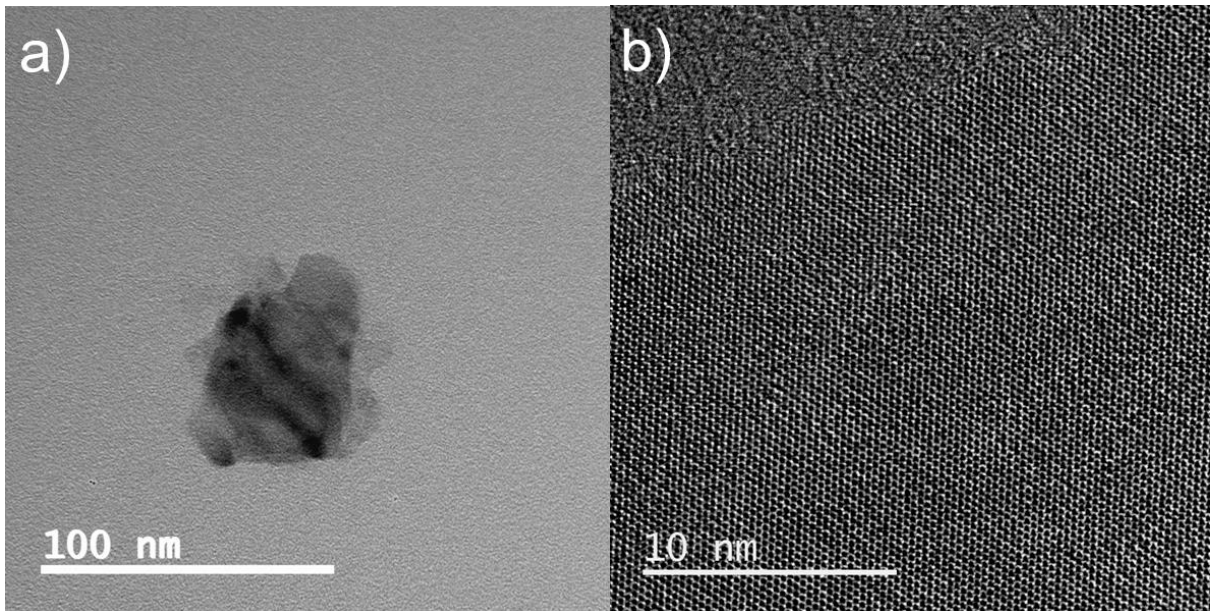
Figure 3.13 HR/TEM images of exfoliated MoS_2 nanosheets obtained from 12800G RCF

supernatant
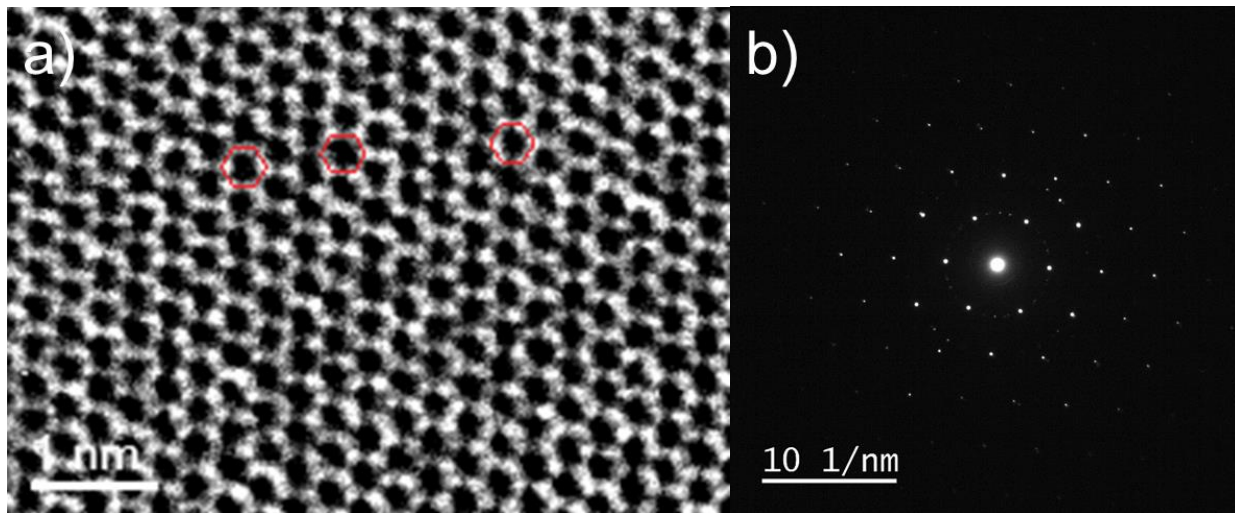
Figure 3.14 a) Zoomed-in HRTEM clearly demonstrating the hexagonal atomic structure of 2H

MoS_2 and b) SAED pattern with d-spacing of 2.61 Å corresponding to the (101) plane
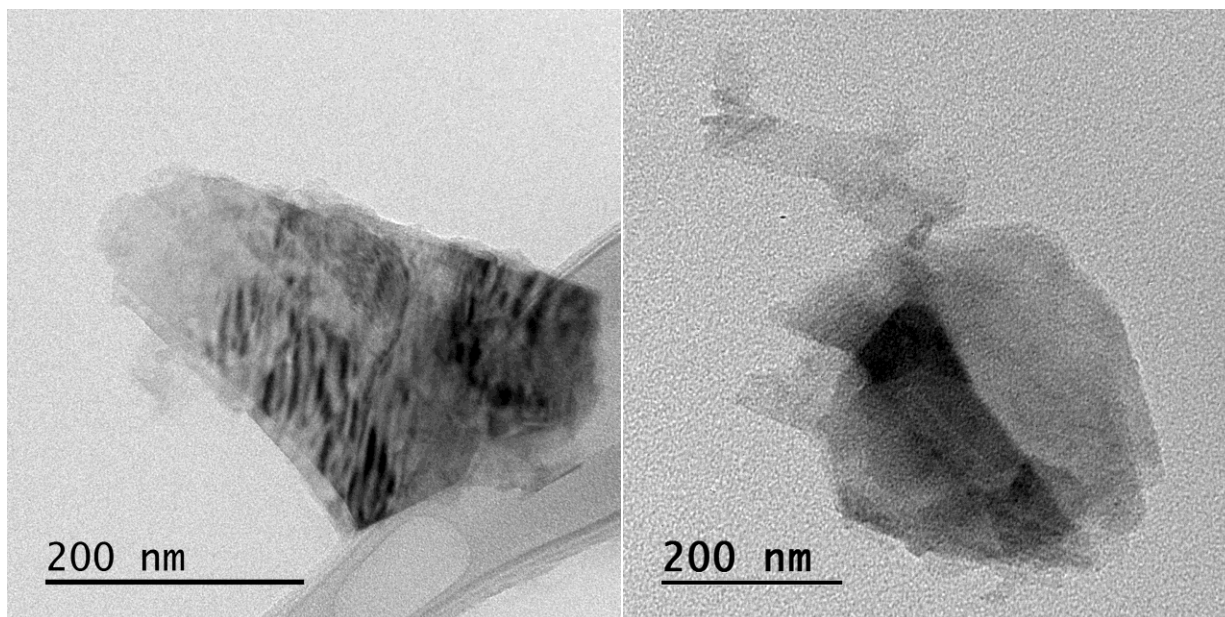
Figure 3.15 Addition TEM images of IPA/water exfoliated nanosheets

3.3.4 X-Ray Powder Diffraction (XRD)

The as-exfoliated MoS_2 nanosheets were characterized using an XRD system. Figures 3.16 and 3.17 show XRD patterns of MoS_2 mineral used for liquid sample exfoliation and XRD fingerprints collected at various stages of centrifugation (400G, 6400G, and 12800G RCFs) with the 12800G supernatant being the final product. After liquid phase exfoliation, the dried MoS_2 samples at various RCF were able to retain the reflection peaks of the family lattice planes (004), (100), (101), (102), (006) and (105) albeit with decreasing intensity in the (002) peak with higher RCF. In line with literature, the decrease in (002) peak intensity implies the successful exfoliation of MoS_2 mineral into few layers and monolayers[59,87]. Additional, with increasing RCF speeds, the XRD patterns seem to contain more noise along with peak broadening. Since increasing RCF results in smaller nanosheets, it is expected that the intensity of X-ray diffraction gets weaker in smaller crystallites as the crystal size is inversely proportional to the FWHM (full width at half maximum) according to the Scherrer's equation which is not applicable to grains larger than 0.1 μm[88].

$$D = \frac{k\lambda}{\beta \cos(\theta)} \tag{3-6}$$

Where D is average grain size, k is a shape factor constant depending on the shape of the crystallite, λ is the X-ray wavelength, β is full width half maximum and θ is the Bragg angle.
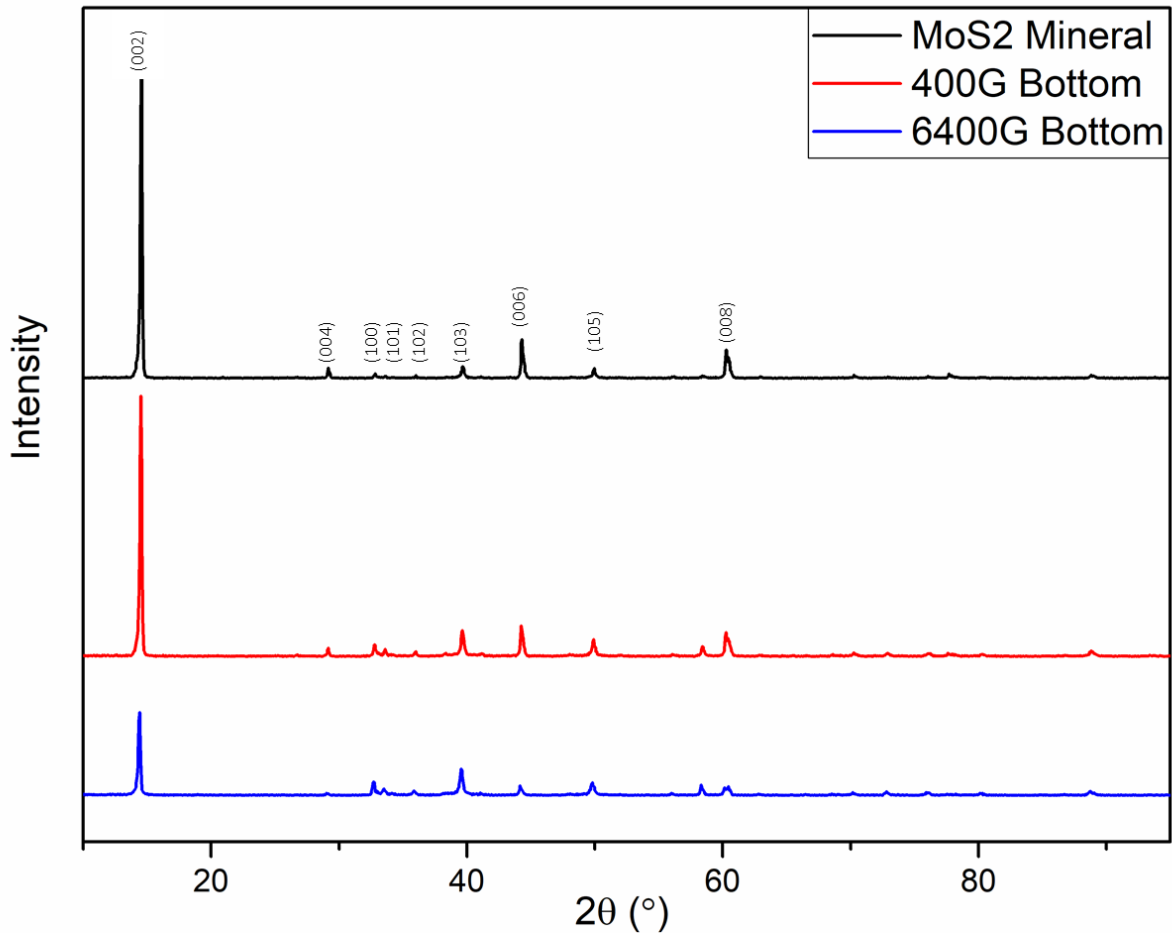
Figure 3.16 XRD patterns of MoS$_2$ mineral compared to centrifuged bottoms at 400G and 6400G
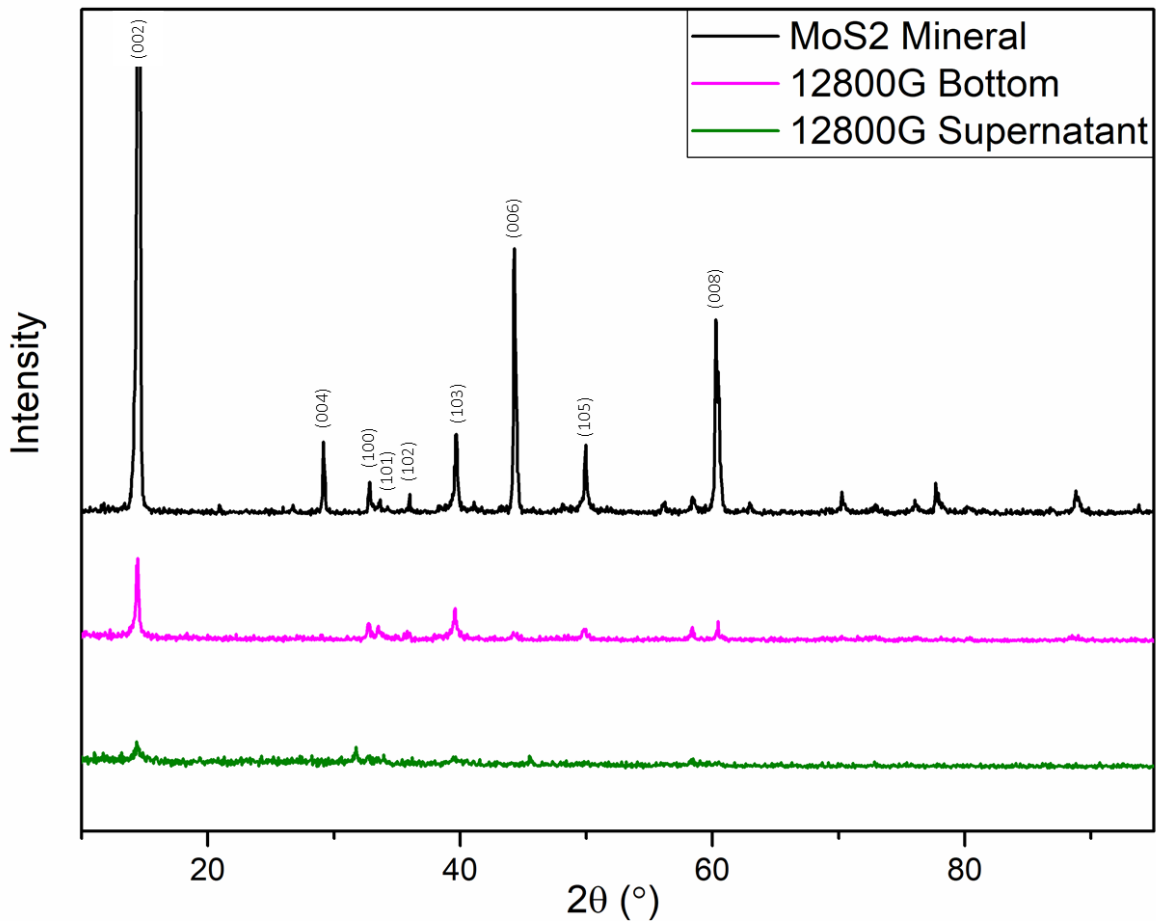
Figure 3.17 XRD patterns of MoS_2 mineral (zoomed in) compared to centrifuged 12800G RCF supernatant and bottom without any zoom

3.3.5 Scanning Electron Microscopy (SEM) with EDX

Scanning electron microscopy with EDX mapping was used to identify the composition of the liquid phase exfoliated MoS_2 nanosheets in IPA/water. Figure 3.18 shows the SEM image with the mapping of molybdenum, sulfur and silica. Table 3.3 shows the atomic and weight composition of the obtained mapping of MoS_2 nanosheets compared to the natural MoS_2 mineral. The atomic composition of silica and chlorine are much higher in the exfoliated MoS_2 nanosheets compared to the natural mineral. This resulted in a skewed S/Mo ratio of 3.97 compared to 2.06

as obtained in the natural MoS_2 mineral. The excess amount of silica could be attributed silica dioxide, commonly found in nature as quartz. If silica dioxide is indeed one of the compounds making up of the impurities, then it is expected that it will reside along with molybdenite in the supernatant as the density of the silica dioxide is lower than molybdenite. The principle behind centrifuge is the separation of materials according to density gradient, denser materials can be found in the sedimentation and vice versa. Therefore, it is expected that materials lighter than molybdenite (lower density) can be found together with molybdenite in the supernatant. This is one of the consequences associated with using natural mineral as the starting material. Oxygen wasn't shown in the elemental composition as EDX is not as accurate for elements with atomic number lower than 10[63]. For analysis purposes, it would make sense to remove as much impurities as possible in order to study the fundamentals behind the hydrogen evolution reaction mechanism. However, the removal of impurities are typically associated with higher processing cost. Thus, the hydrogen evolution reaction of the exfoliated MoS_2 nanosheets were investigated as it is despite the fact that there was unexpectedly high concentration of impurities within the MoS_2 nanosheets after exfoliation and centrifuge processing.
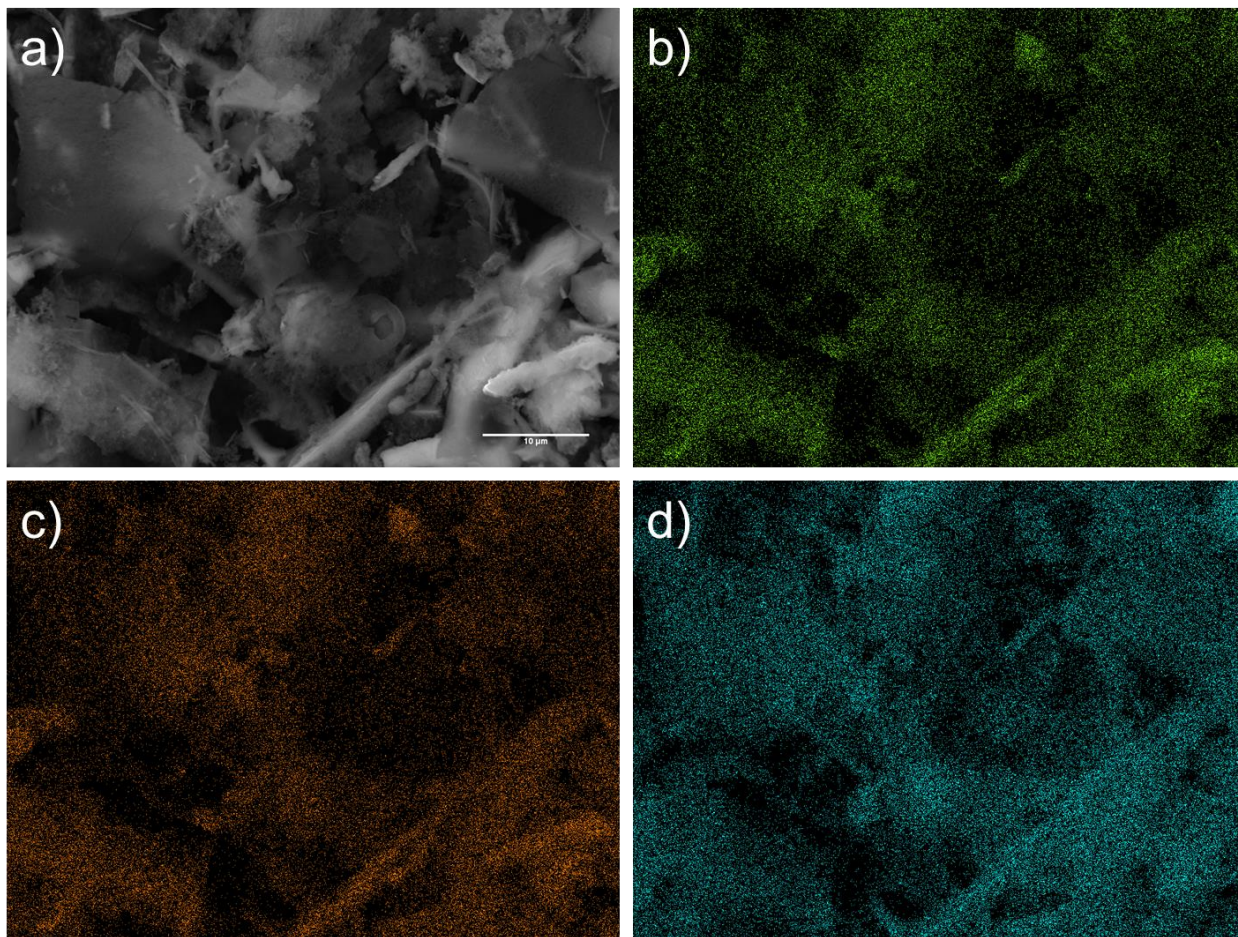
Figure 3.18 SEM of exfoliated a) MoS$_2$ nanosheets with its corresponding EDX images of b) Mo

c) S and d) Si

Table 3.3 Elemental analysis of exfoliated MoS_2 nanosheets compared to natural MoS_2 mineral

	Liquid Phase Exfoliated MoS_2 Nanosheets in IPA/water		Natural MoS_2 Mineral	
	Weight %	Atomic %	Weight %	Atomic %
Al	0.57	0.76	0.37	0.52
Si	34.12	44.29	0.74	0.87
S	27.38	31.13	39.41	65.00
Cl	10.79	11.09	0.31	0.36
K	0.35	0.33	0.11	0.10
Ca	2.15	1.95	0.04	0.10
Fe	3.99	2.60	1.88	1.49
Mo	20.65	7.85	57.14	31.56
S/Mo		**3.97**		**2.06**

3.3.6 Ultraviolet-Visible Spectroscopy (UV-Vis)

Figure 3.19 shows UV-Vis spectra for the MoS_2 nanosheets exfoliated in different volume percent of IPA in DI water with bath sonication only and a combination of bath and ultrasonic probe. DI water was used as the background for all scans. With the exception for a little bump at around the 535 nm, pure IPA did not exhibit an absorbance spectrum within the 300-700 nm range. Therefore, it is plausible to attribute any peaks found within the 300-700 nm range to MoS_2 only and ignore the 535 nm bump. For MoS_2 nanosheets exfoliated in the IPA/DI water mixture, two peaks were observed at around 610 nm and 670 nm, they arise from the K point of the Brillouin zone and are known as the A1 and B1 excitons respectively[54,89,90]. There is also a convoluted C exciton peak appearing at around the 400 nm region with not a lot of significance[91]. The A1 and B1 are prominent peaks well established in literature to be indicators of the transition

of MoS$_2$ from an indirect band gap material to a direct band gap[92]. Thus, we can conclude that bulk MoS$_2$ was successfully exfoliated into nanosheets in the IPA/DI water mixture.
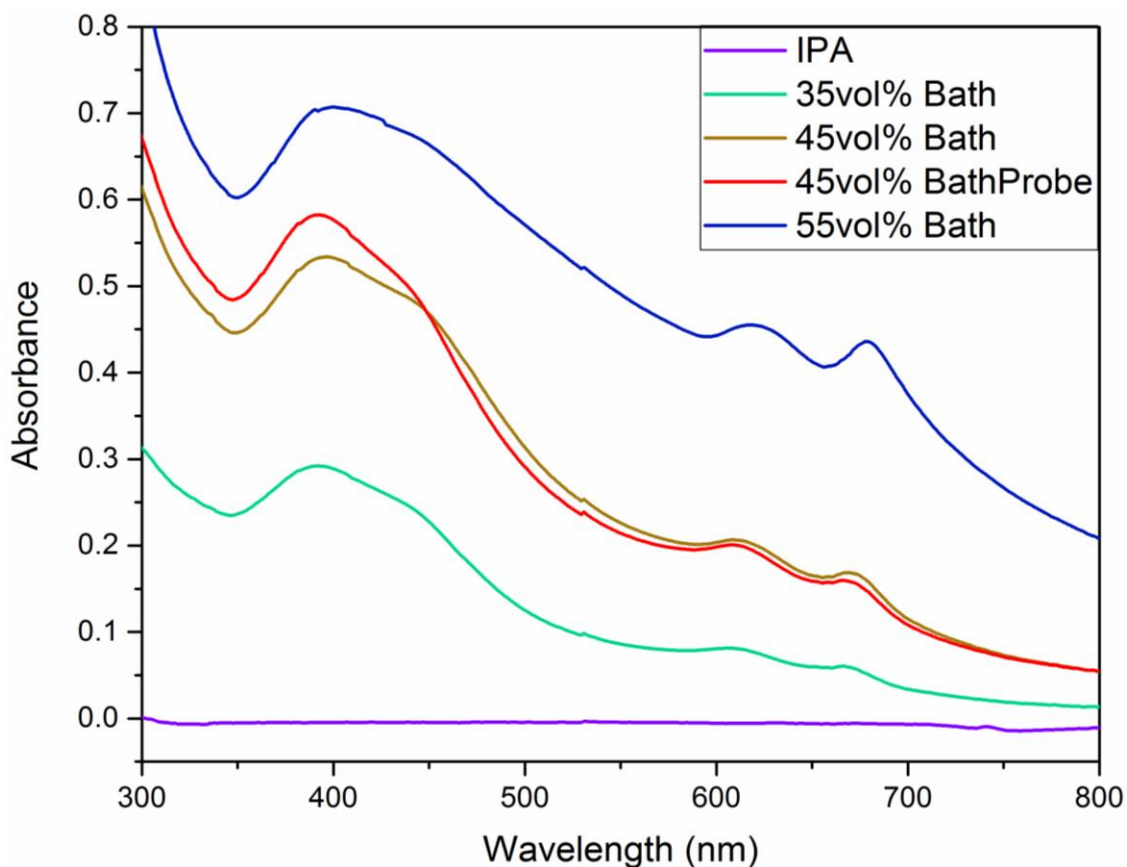
Figure 3.19 UV-Vis of MoS$_2$ nanosheets exfoliated in varying volume percent of IPA in DI water

The 55vol% (50wt%) IPA/DI water exhibited significantly stronger absorbance peaks compared to other ratio of IPA to DI water samples. It was observed that the concentration of nanosheets is increasing from 35vol% to 55vol% as absorbance is directly related to solution concentration. However, there should be an optimal ratio as MoS$_2$ was not exfoliated in 100% 2-propanol nor was it exfoliated in 100% DI water. This is in line with literature results, as Halim et al. have shown the most effective concentration to exfoliate MoS$_2$ in a co-solvent environment is 30wt% IPA in water (equivalent to 35vol% IPA)[49]. This discrepancy could be attributed to the impurities present within the natural MoS$_2$ mineral that was used for the experiments (i.e. organic

contaminants will result in a higher contact angle on hydrophilic surfaces). As evidenced by the optical spectra, the effect of using ultrasonic probe in conjunction with bath sonication on solution concentration was not significant as the absorbance intensity did not change significantly. Further study is required to understand why the ultrasonic probe did not enhance the exfoliation of MoS_2 in the co-solvent of IPA/water. Additional experiments could be performed to determine the optimal ratio of IPA to water for the best MoS_2 exfoliation.

Molybdenum disulfide natural mineral was successfully exfoliated into nanosheets mostly around 200 nm by 200 nm in the co-solvent of isopropanol and water. The natural mineral and the exfoliated nanosheets were characterized with XRD, UV-vis, TEM, AFM, SEM with EDX and tested for electrochemical response in a 3-electrode system. Despite the high concentration of contaminants in the exfoliated nanosheets as shown by SEM with EDX, the exfoliated nanosheets still exhibited an increase of more than 20% in both the onset potential and the Tafel slope compared to the unexfoliated mineral. UV-vis results demonstrated the transformation of indirect band gap MoS_2 natural mineral into a direct band gap material upon exfoliation. XRD showed that the family lattice planes associated with the natural mineral were preserved after exfoliation. High resolution TEM results showed that exfoliated nanosheets exhibited a lattice constant of 2.61 Å, which is a match to the (101) plane. AFM demonstrated mono and few layers made up most of the exfoliated nanosheets. Thus, the co-solvent of isopropanol and water was able to successfully exfoliate MoS_2 mineral into nanosheets via liquid phase exfoliation.

3.4   N-Methyl-2-Pyrrolidone Samples

This section contains the exfoliation of natural mineral MoS_2 in organic solvents, primarily NMP. Similar characterization techniques compared to the IPA/water co-solvent exfoliated MoS_2 were used.

3.4.1 Hydrogen Evolution Reaction for NMP Exfoliated Nanosheets

Monolayer of MoS_2 is known to have superior HER performance compared to the bulk phase or few-layers as each additional layer of MoS_2 decreased the catalytic activity by a factor of ~4.5[48]. For the electrochemical experiments involving NMP, a catalyst loading of 0.026 mg/cm^2 was used due to quantity constraint. Even though liquid phase exfoliation with the use of organic solvent was supposed to produce higher yields in comparison to other methods such as mechanical exfoliation, the nanosheets yield from NMP exfoliated was still extremely low after processing. In literature, lower loadings correlate with higher overpotential for non-noble element and thus makes comparison of empirical data to literature slightly difficult[78]. Therefore, an identical loading capacity shall be used in lieu of literature data in order to compare the unexfoliated to the exfoliated material. Figure 3.20 shows a comparison of NMP exfoliated nanosheets to the unexfoliated material at an identical loading capacity of 0.026 mg/cm^2, whereas Figures 3.21 and 3.22 show the polarization curves and Tafel plots for the unexfoliated MoS_2 mineral, unexfoliated mineral with trace amount of NMP (0.6 µL equivalent or 5 vol%) to simulate residual solvent, and NMP exfoliated MoS_2 nanosheets compared to platinum wire.
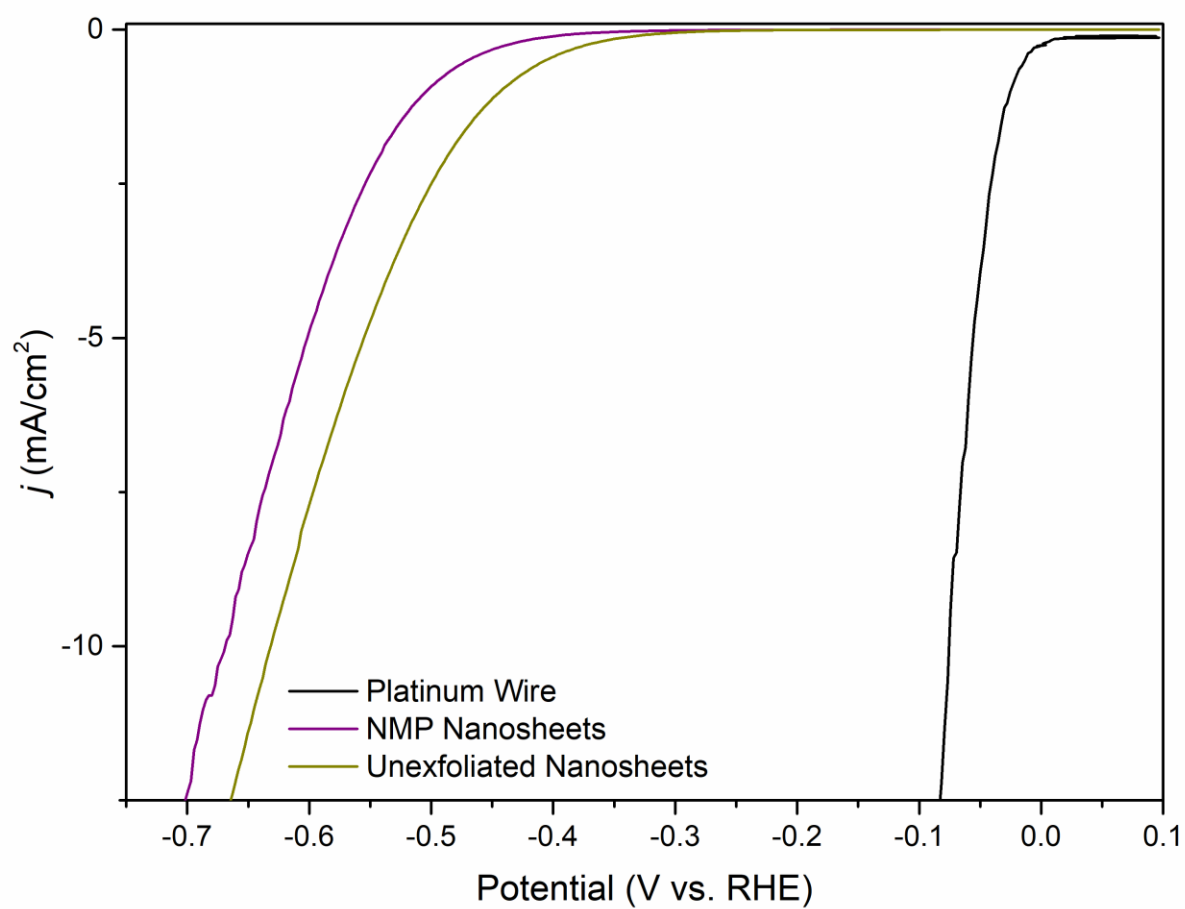
Figure 3.20 NMP exfoliated nanosheets compared to the unexfoliated material
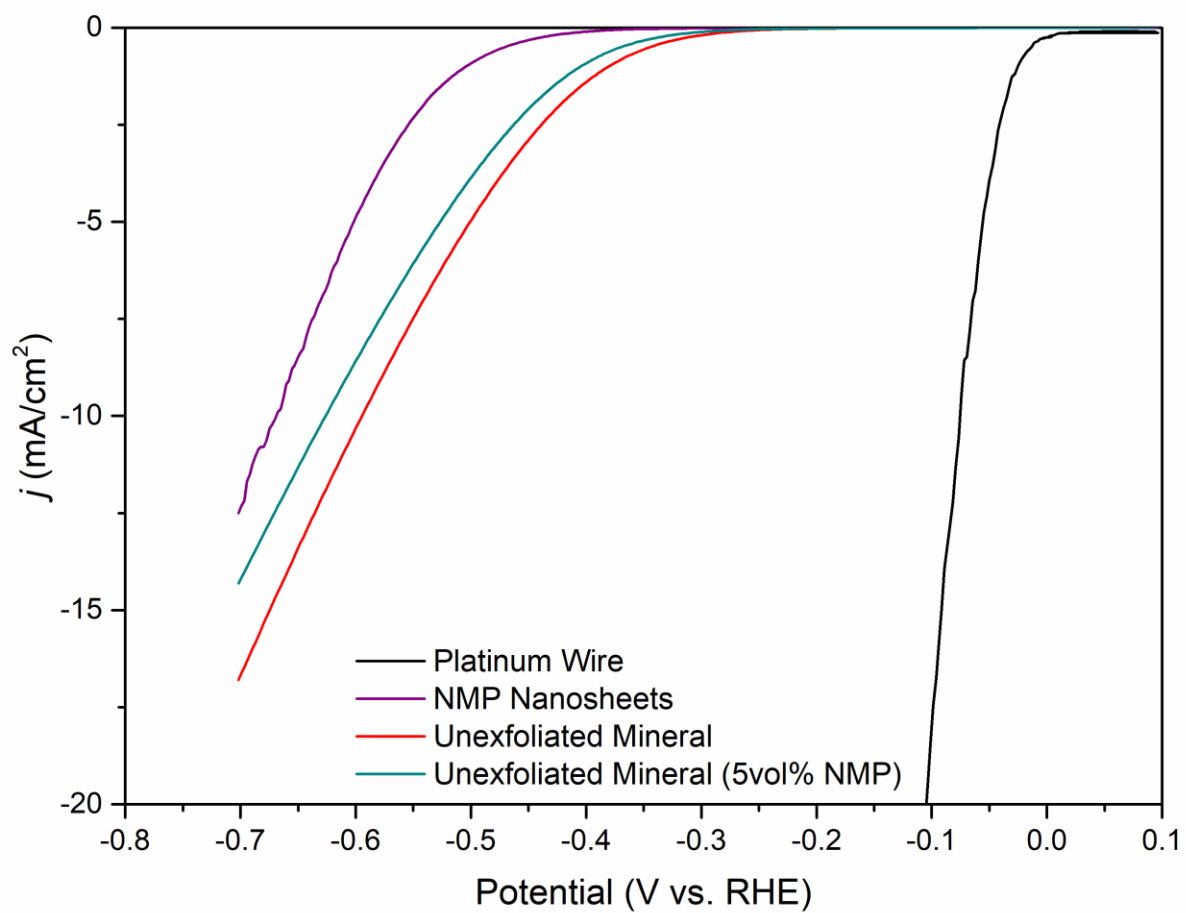
Figure 3.21 Polarization curves for comparing the unexfoliated mineral to the addition of trace amount of NMP
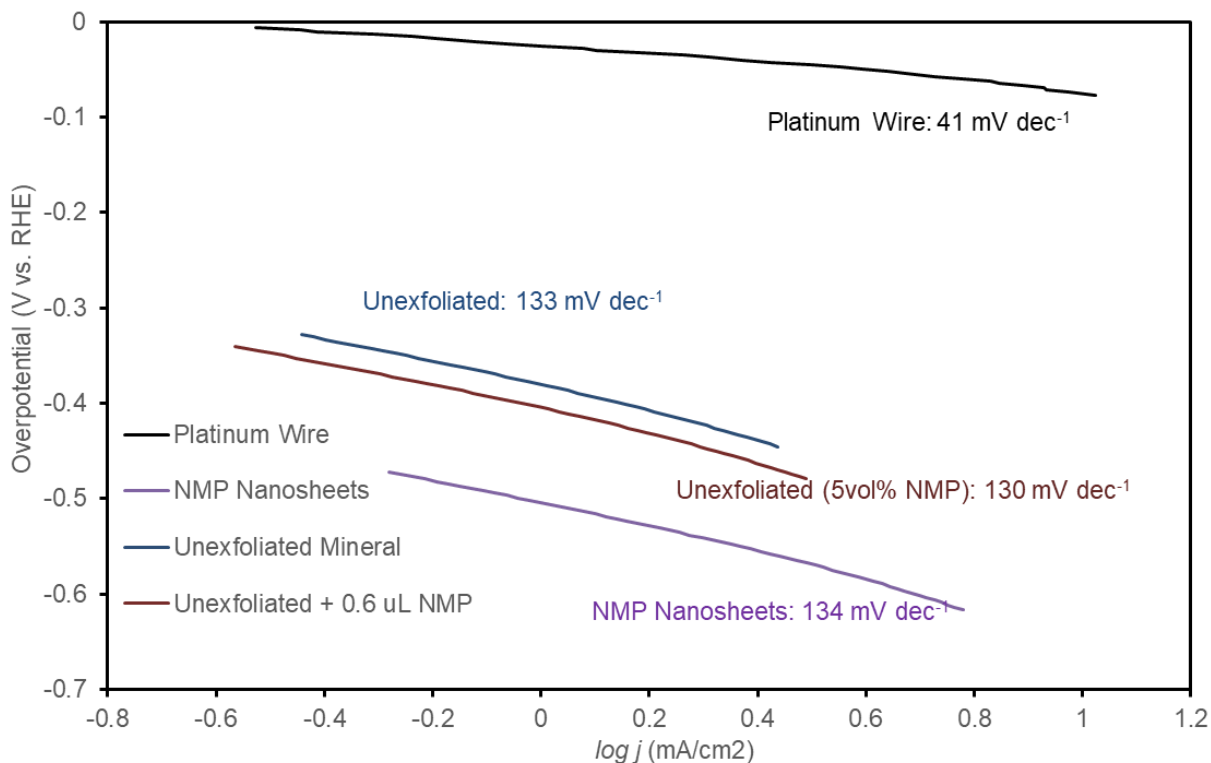
Figure 3.22 Tafel plots for NMP processed sample and the effect of trace amount of NMP

Table 3.4 shows the onset potential, overpotential (vs. RHE) and Tafel slope for the aforementioned samples. The obtained NMP exfoliated MoS_2 nanosheets electrochemical performance was on par with the unexfoliated material. This was surprising considering the exfoliated MoS_2 nanosheets should exhibit significantly better HER activity as per co-solvent exfoliated nanosheets[48]. This lack of improvement in electrochemical performance could be attributed to contaminants interference/concentration. As shown in the co-solvent exfoliated nanosheets, the selected method of processing resulted in higher concentration of contaminants in the nanosheets. Due to the nature of the MoS_2 mineral used, the contaminants may have contributed to a lower surface tension value, thus contributing to the poor exfoliation yield. Combining this with the lack of clearly defined A1 and B1 excitons peaks, the concentration of contaminants in the NMP exfoliated material may have exceeded that of the co-solvent exfoliated nanosheets. In order to investigate the effect of trace amount of organic solvent (NMP) on HER

activity, trace amount of NMP were added to the unexfoliated material. As shown in Figure 3.21 and 3.22, addition of 50 μL NMP to 1 mL of 45/55 vol% 2-Propanol/water solution (5vol% or 0.6 μL equivalent) containing the unexfoliated material resulted in almost no change to the catalyst activity. Addition of 5 vol% NMP resulted in no significance difference for the electrochemical activity of the unexfoliated material. A 5% discrepancy in the overpotential (at 10 mA/cm^2) and a 2% discrepancy in the Tafel slope are well within the error range. As shown previously, the values of Tafel Slope could very well fluctuate depending on how good of the fit of the linearized equation to the data points. What seemed like a trivial difference, 0.005 in R-squared, actually resulted in a 13% discrepancy in the Tafel slope. Thus, the results obtained for the unexfoliated material with the addition of trace amount of NMP is within the error range of the unexfoliated material. In retrospect, it would've been better to add trace amount of NMP to the nanosheets obtained from the co-solvent exfoliation as the unexfoliated material were inactive at the first place. It was very hard to conclude whether NMP contributed or not to the electrochemical activity when the unexfoliated material did not have any electrochemical activity at the first place. Further study is required to determine the root cause(s) of the lack of activity from the NMP exfoliated nanosheets.

Table 3.4 Onset potential and Overpotential (vs. RHE) comparison

	Onset potential [mV]	Overpotential (at 10 mA/cm^2) [mV]	Tafel Slope [mV/dec]
Platinum Wire	-13	-77	41
Unexfoliated	-243	-595	133
Unexfoliated (5vol% NMP)	-285	-627	130
NMP Exfoliated	-465	-668	134

3.4.2 Atomic Force Microscopy (AFM)

In order to determine the height of the MoS_2 nanosheets, tapping mode AFM was used to determine the heights of the drop-casted NMP exfoliated MoS_2 nanosheets immobilized on mica. Since there is some uncertainty surrounding the identity of the material, the statistical count of heights will be reported together with the number of layers. For comparison purposes, the height benchmark for a monolayer of MoS_2 is approximately 0.615 nm, n multiples of that signifies n layers[84,85]. Figure 3.23 shows the AFM results while Figure 3.24 shows the statistical count of the heights measurement along with its equivalent layers. A cut-off mark of 0.5 nm was used, anything below that was not part of the statistical count. Some of the height measurements does not appear to be in multiples of 0.615 nm, this could be attributed to the contaminants present on the nanosheets. Either way, the MoS_2 exfoliated in NMP are quite thin and thus could be suitable candidates for hydrogen evolution reaction despite the presence of contaminants.
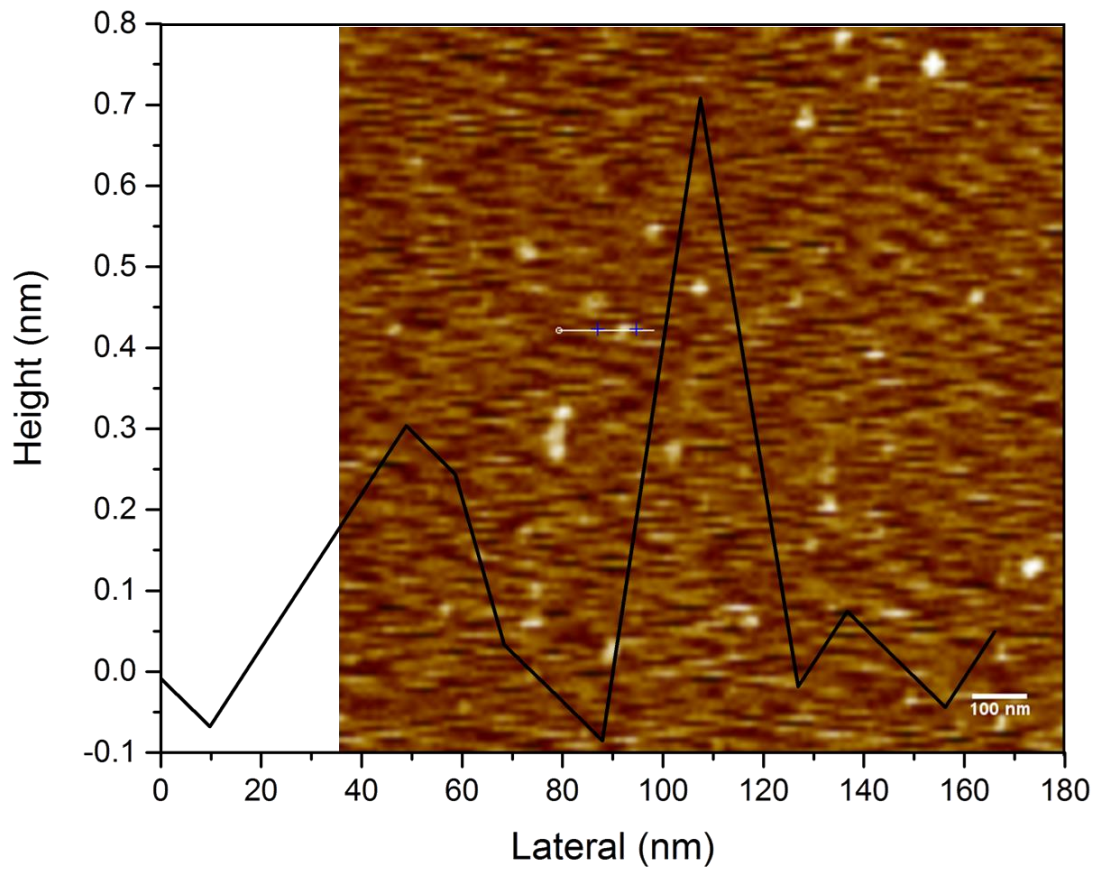
Figure 3.23 AFM scan with height overlay for NMP exfoliated MoS₂ nanosheets
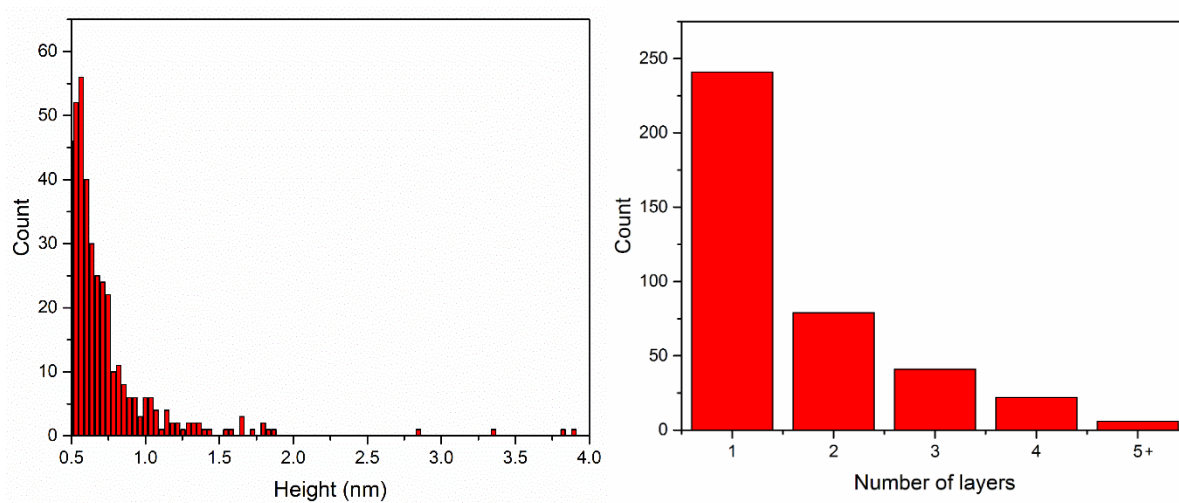
Figure 3.24 Statistical count of the absolute height of the nanosheets along with number of

layers equivalent

3.4.3 Transmission Electron Microscope (TEM)

The supernatant of liquid phase exfoliated MoS_2 mineral in NMP at 6000G were characterized under HRTEM as shown in Figure 3.25. The lattice constant, d, was 0.387 nm. Unfortunately, this value does not match up with any of the d-spacing values obtained from the XRD data. This mismatch could be attributed to either the expansion of MoS_2 layer structure as a result of intercalation or contaminants affecting the lattice constant parameter[93]. Additional TEM images of NMP exfoliated nanosheets are shown in Figure 3.26. Either way, HRTEM by itself cannot identify the material composition nor provide a quantitative result of the thickness of material. Thus, further characterization is required to identify and quantify the material composition and thickness, respectively.
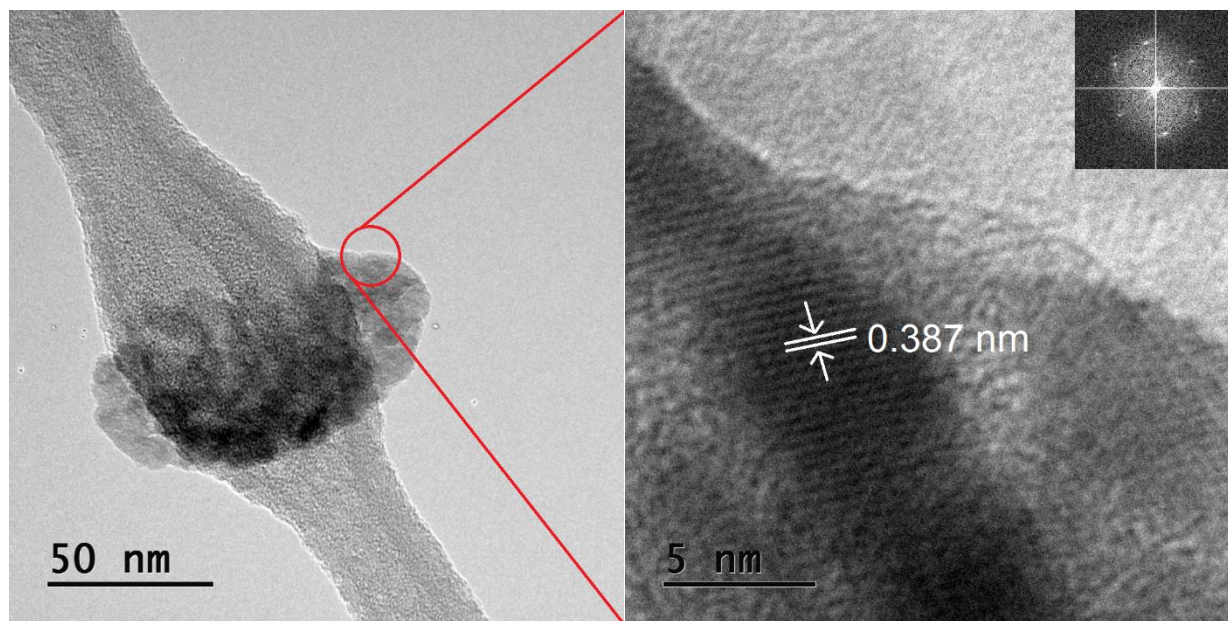
Figure 3.25 HRTEM of MoS_2 exfoliated in NMP, 6000G supernatant on lacey carbon grid

(SAED zoomed in not to scale)
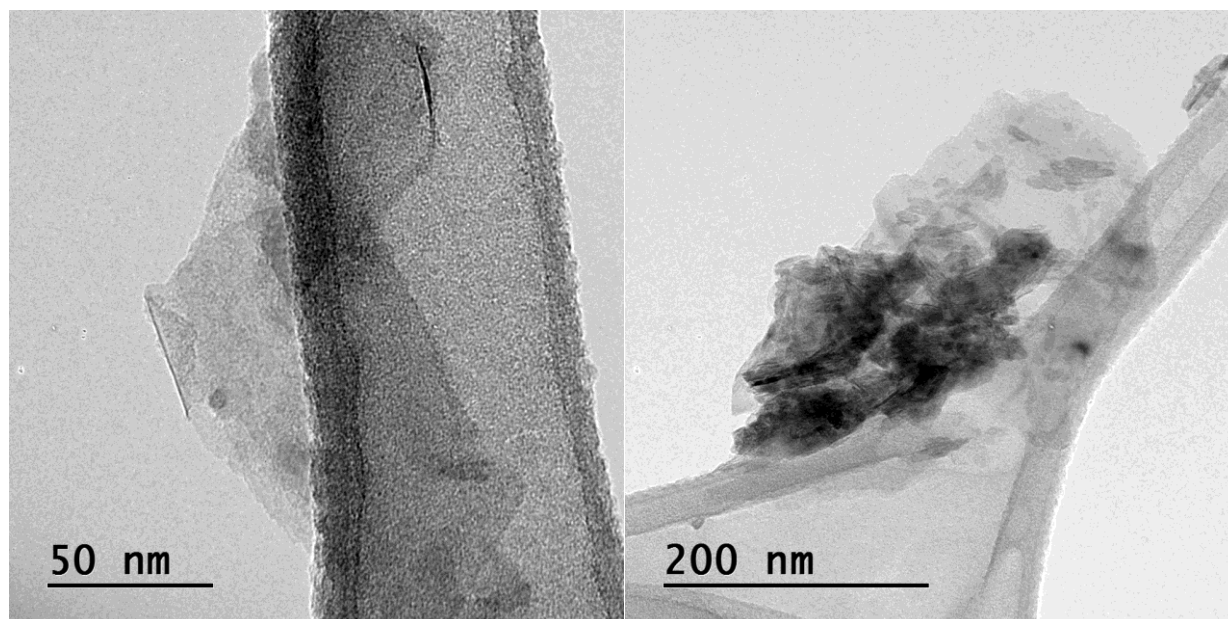
Figure 3.26 TEM images of NMP exfoliated nanosheets

Figure 3.27 shows the TEM images for the N12P and N8P exfoliated nanosheets after processing. They were not used for further characterization as the focus of organic solvent is on NMP.
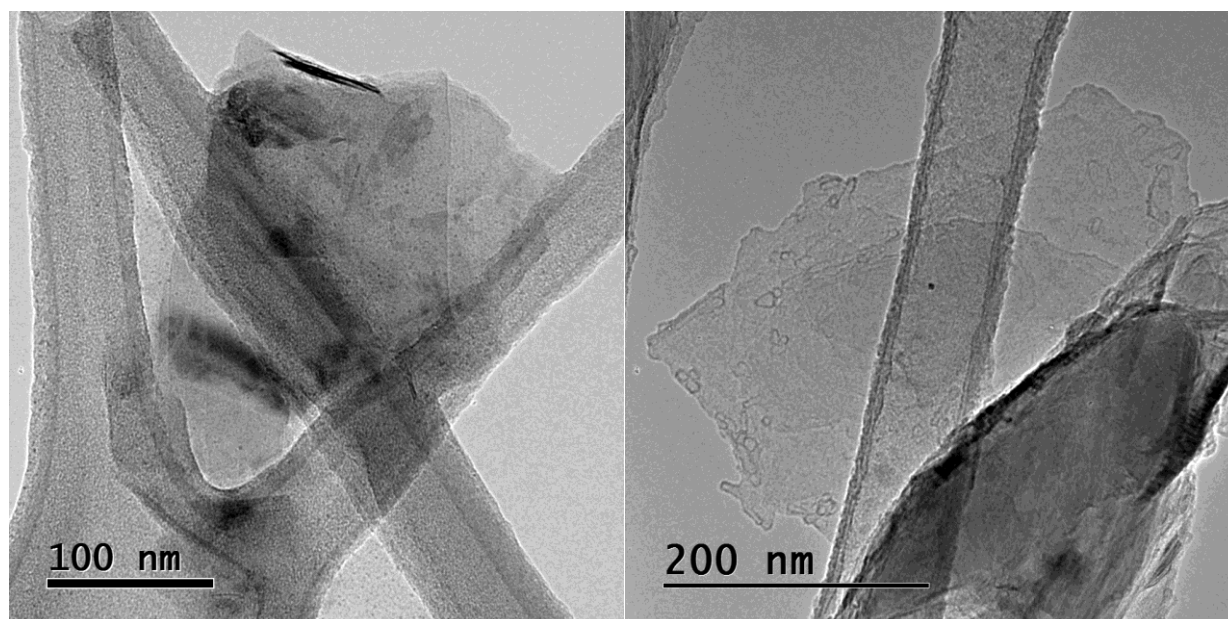
Figure 3.27 N12P (left) and N8P (right) exfoliated MoS2 nanosheets

3.4.4 Effect of Pre-Processing with Ultrasonic Bath

The effect of using ultrasonic bath as a pre-processing step before probe sonication (BP) versus probe sonication only was investigated. Concentration of the as-exfoliated MoS_2 after liquid cascade centrifuging at 6000G was used as benchmark. Figure 3.28 shows the effect of pre-processing with bath sonication followed by probe sonication versus using only probe sonication in the various organic solvents. Upon first glance, there appears to be no significant different for MoS_2 in the two pyrrolidone based organic solvents, 1-dodecyl-2-pyrrolidone (N12P) and 1-octyl-2-pyrrolidone (N8P). In NMP, there is a tiny shift in color that could be attributed to pre-processing. In order to examine this in detail, UV-Vis was performed with its respective solvent as the background.
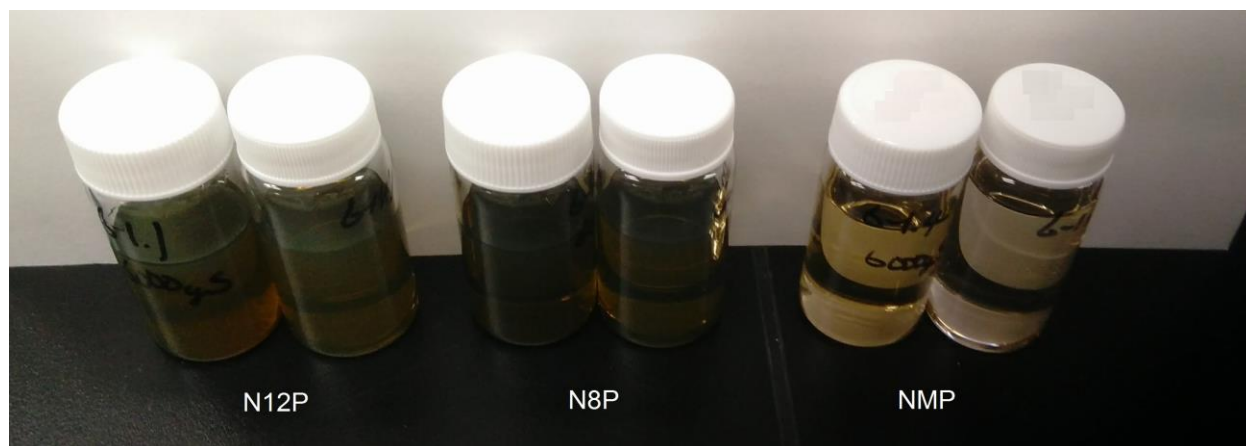
Figure 3.28 Supernatant at 6000G of MoS_2 nanosheets in various organic solvents as a
comparison of probe sonication only (right) versus pre-processing with ultrasonic
bath followed by probe sonication (left)

3.4.5 Ultraviolet-Visible Spectroscopy (UV-Vis)

Figure 3.29 shows UV-Vis spectra for the MoS_2 nanosheets immersed in various organic solvents after pre-processing with and without bath sonication followed by liquid cascade centrifugation at 6000G. The general trend is that the pre-processed samples exhibited a higher

absorbance value compared to probe sonicated only samples. However, there appears to be no shift in peaks between the two methods. The two absorption peaks for MoS_2 nanosheets in N12P bath-probe processed (BP) are located at 614 nm and 671 nm, otherwise known as the A1 and B1 excitons, respectively[54,89,90]. For N8P (BP), the A1 and B1 excitons are located at 610 nm and 670 nm, respectively. Those two prominent peaks are well established in literature to be indicators of the transition of MoS_2 from an indirect band gap to a direct band gap material, thus signaling successful exfoliation from bulk into nanosheets[92].
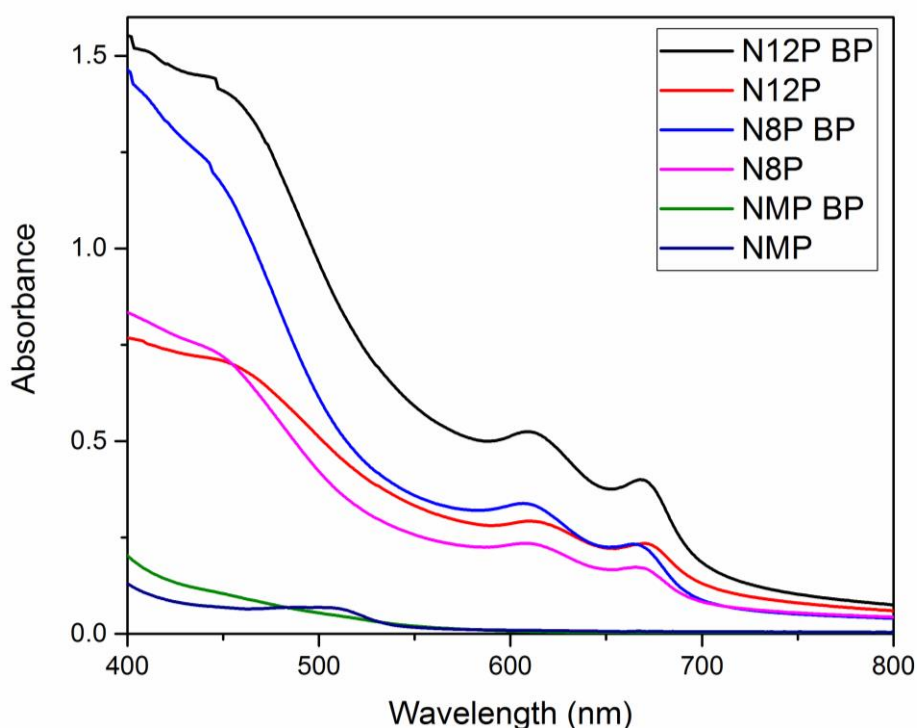
Figure 3.29 Comparison of pre-processing with bath sonication (BP) versus probe sonication

For NMP (BP), there is no discernible peaks in the 610-670 nm range. This is particularly alarming as this would either indicates that the band gap transition did not happen or the concentration of the nanosheets was simply too low. It has been reported in literatures that the lack of characteristic peaks in the 610 nm and 670 nm regions along with a peak in the near UV region ($\lambda < 300$ nm) are good indicators of MoS_2 quantum dots[94,95]. As the result of additional pre-

processing with ultrasonic bath, the A1 and B1 excitons peaks in the N12P and N8P became much more distinct, whereas it did not really matter for NMP. This further demonstrates the result of increased concentration of nanosheets through addition of ultrasonic bath processing step. Going back to the NMP solutions, TEM images showed nanosheets on the size of 100-150 nm albeit much more scattered compared to the other two solutions. Thus, the lack of excitons peaks can be attributed to the low concentration of MoS_2 nanosheets in NMP solution compared to N8P or N12P. The concentration difference was observed qualitatively during synthesis in Figure 3.30, as the supernatants of N12P and N8P solutions after centrifugation at 6000G were much darker in appearance compared to the nanosheets NMP solutions. As the absorbance of the samples are directly related to the nanosheets concentration, pre-processing with ultrasonic bath prior to probe sonication is thus able to enhance the concentration of nanosheets in solution, especially the thinner nanosheets.
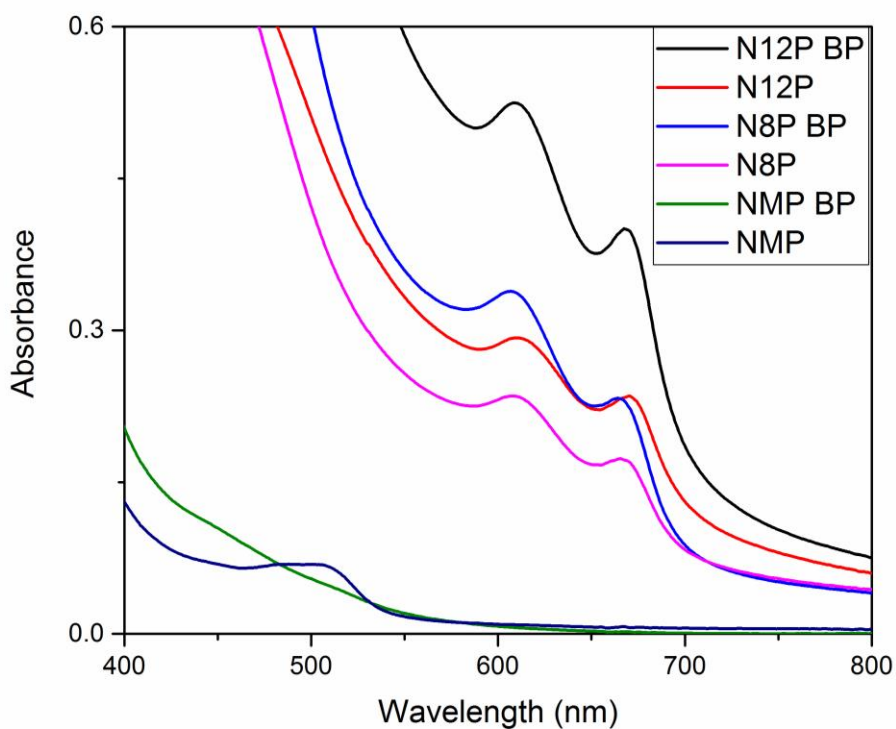
Figure 3.30 Zoomed in version of UV-vis comparing bath pre-processing with probe only

3.4.6 Importance of Matching Surface Tension

In order to reaffirm the important role of organic solvent acting as the stabilizing agent after exfoliation, MoS_2 was exfoliated in ethanol 96% grade laboratory reagent and deionized water with resistivity of 18.2 MΩ·cm. The surface tension of ethanol and deionized water at 20°C are 22.3 mN/m and 72.7 mN/m, respectively[96]. They were selected to demonstrate the effect of mismatching surface tension. Initially, MoS_2 was successfully exfoliated in both solutions, giving the solution a cloudy look similar to MoS_2 exfoliated in organic solvent. However, after leaving the solutions for a couple of days, there was significant sedimentation observed within vial and the solution is quite transparent, giving it a similar look to the washed MoS_2. Albeit both ethanol and water demonstrated a certain degree of exfoliation, the mismatch between surface tensions ultimately led to the sedimentation of MoS_2. This is in line with previous literature results where the exfoliated MoS_2 remained unstable in solvents with a mismatch in surface tension. By matching surface tension, the enthalpy of mixing could be minimized. This in turn led to minimization of the Gibbs free energy of mixing. This reaffirms the importance of matching the surface tension of the solvent and MoS_2 in order to achieve exfoliation as well as stabilization of the exfoliated material.

Being a natural mineral, the MoS_2 used in the experiments will contain some form of impurities such as Al, Si, Fe and Ca (please refer to the SEM EDX results for detail), however little in concentration. Even though they do not have a big effect on the S/Mo ratio in the MoS_2 mineral, the contaminants became concentrated upon processing. From literature, a wide range of surface tension for MoS_2 are reported. However, most of the reported data were for compounds with >99% purity, whereas the natural MoS_2 mineral used for the liquid phase exfoliation in this thesis was ~97% purity by weight (obtained by adding the weight percent of Mo and S atoms under EDX mapping). Additionally, ambient impurities can contribute to a lower surface tension value over a 20 minutes time span[97]. Therefore, there is a big possibility that impurities within the MoS_2 mineral actually contributed in a lower surface tension.

Liquid phase exfoliation of molybdenum disulfide natural mineral was achieved with the aid of organic solvent, specifically n-methyl-2-pyrrolidone. Similar to the co-solvent exfoliated nanosheets, the organic solvent exfoliated material were characterized with UV-vis, TEM, AFM and electrochemical scans. SEM with EDX and XRD were not used for the NMP exfoliated material due to the extremely low yield (approximately 1/50 yield of the co-solvent). According to UV-vis results, the use of ultrasonic probe together with ultrasonic bath for exfoliation contributed to a higher absorbance (concentration) compared to just using the ultrasonic bath. This effect was not as pronounced in NMP compared to the other two organic solvents, as the lack of A1 and B1 exciton peaks could be attributed to the low concentration in general. Electrochemistry results showed no discernible difference between the unexfoliated material, exfoliated material and the unexfoliated material with addition of 5vol% NMP. AFM results showed the materials to be primarily on the scale of mono and few-layers equivalent (~0.615 nm is the height per layer of MoS_2). High resolution TEM results showed that the NMP exfoliated material had a lattice spacing of 3.87 Å. This value did not match up with any of the lattice planes corresponding to the natural MoS_2 mineral's XRD fingerprint. At this point, it was suspected that the NMP exfoliated nanosheets contained high concentration of contaminants.

Chapter 4 Conclusion and Future Work

4.1 Conclusions

In this thesis, natural molybdenite (MoS_2) mineral was successfully exfoliated into nanosheets consisting of few layers and monolayer in co-solvent of 2-propanol (IPA) with water and in organic solvent n-methyl-2-pyrrolidone (NMP). Liquid phase exfoliation was achieved by matching surface tension between molybdenite mineral and the solvents. Centrifugation was used to separate the exfoliated MoS_2 nanosheets from the bulk and unexfoliated materials. Within the co-solvent of 2-propanol/water, few layers and monolayer of MoS_2 were observed in the 12800G RCF supernatant. Similar observation was made for the MoS_2 nanosheets obtained in the 6000G RCF supernatant exfoliated in NMP. The exfoliated MoS_2 nanosheets were characterized with UV-visible spectroscopy, X-ray diffraction, transmission electron microscopy, scanning electron microscopy, and atomic force microscopy. A demonstration of application was shown with the electrochemistry experiments using a 3-electrode cell setup in 0.5M H_2SO_4.

The MoS_2 used in the experiments were natural mineral obtained from the Wolfram mine located in Queensland, Australia. Naturally, it was not 99.9% purity as there was traces of impurities present (i.e. Si, Al, Fe, Ca etc.). The impurities were more pronounced in the top layer when MoS_2 was mixed in water. In order to investigate this matter, MoS_2 was purchased from Sigma Aldrich with 99% assay purity and the top layers were collected for both the natural mineral and the Sigma Aldrich sample. Under the optical microscope, it was clear that the mineral sample's top layer had needle-like structures (predominant impurity was calcium) in it whereas the Sigma Aldrich sample's top layer was homogenous with no impurities detected. Scanning electron microscopy (SEM) with energy diffraction X-ray (EDX) was then used to identify the elemental composition of the MoS_2 mineral's top layer. A sulfur to molybdenum (S/Mo) ratio of 2.16 was obtained for an area analysis whereas point analysis for the needle-like structures indicated an S/Mo ratio of 4.35 with 23 atomic % of calcium along with other impurities. The

needle-like structures predominantly consisted of sulfur, calcium and molybdenum. This was one of the unavoidable consequences when using natural mineral compared to MoS_2 obtained from chemical vapor deposition or hydrothermal synthesis. Instead of attempting to remove the impurities at a high cost due to low concentrations, the natural mineral was used as it was with approximately 97% purity by weight.

X-ray powder diffraction (XRD) was used to verify the crystal structure of the mineral and exfoliated nanosheets. There was a good match between of the reflection peaks with decreasing intensity at higher centrifuge speeds. This was consistent with literature results, as decreasing intensity in the (002) peak is a good indicator of successful exfoliation into few layers and monolayers[59,87]. UV-visible spectroscopy was used to identify and confirm the two characteristic peaks for MoS_2 nanosheets at the 610 nm and 670 nm region. Both peaks were observed for the co-solvent exfoliated sample whereas they were observed in other pyrrolidone based organic solvents but not in the NMP exfoliated samples. This could be attributed to the low concentration of exfoliated nanosheets in NMP. Based on HRTEM, the co-solvent exfoliated nanosheets were able to retain its trigonal prismatic (2H) structure as the UV-vis peaks were a good indicator of that along with d-spacing of 2.61 Å for the exfoliated nanosheets matching to the (101) family lattice plane. However, for the exfoliated nanosheets in n-methyl-2-pyrrolidone, had a d-spacing of 3.87 Å. This was inconsistent with the XRD pattern as the nearest d-spacing is 3.33 Å attributed to the (004) family lattice plane. It was suspected that the NMP exfoliated nanosheets predominantly consisted of impurities, which could explain the mismatch in d-spacing[98]. Albeit the atomic force microscopy imaging showed that the height of the NMP exfoliated nanosheets were within the few-layers and monolayer of MoS_2 range, they should be taken with a grain of salt as the samples may contain high concentrations of impurities. The exfoliated nanosheets in organic solvent will now take a backseat to the co-solvent exfoliated MoS_2 nanosheets due to the uncertainty surrounding the exact composition.

HRTEM was used to confirm the lattice structure for the co-solvent exfoliated MoS₂ nanosheets. A d-spacing of 2.61 Å was obtained and it was a match to the (101) family lattice plane. Atomic force microscopy was used to determine the thickness of the exfoliated nanosheets, where the majority of the nanosheets are within the few layers and monolayer region. SEM with EDX mapping was performed on the exfoliated nanosheets. The S/Mo ratio was skewed at 3.97 with silica accounting for 44% of the atomic composition followed by sulfur and molybdenum. It was expected that the natural mineral molybdenite contained impurities, but it was still a surprise to observe such high concentration of impurities within the exfoliated nanosheets. This could be attributed to the insufficient removal of impurities from centrifugation due to lower density of impurities compared to that of molybdenum disulfide.

In its bulk form, molybdenum disulfide is inert with properties that resemble of graphite and commonly used as a solid lubricant grease. On the nanoscale, molybdenum disulfide could be a good hydrogen evolution reaction (HER) catalyst due to an increase in active edge sites. The electrochemical experiments were conducted in 0.5 M H_2SO_4 electrolyte with a rotating disk electrode to assess the catalyst performance and compared to the benchmark material, platinum. Compared to the unexfoliated mineral, the nanosheets from the co-solvent exfoliation demonstrated an increase in catalytic performance across all categories with the exception of exchange current density, which remained approximately the same. At a catalyst loading of 0.13 mg/cm², the exfoliated nanosheets exhibited onset potential of 201 mV, overpotential (at 10 mA/cm²) of 407 mV and exchange current density of 3 μA/cm² compared to that of the unexfoliated mineral's onset potential and overpotential 258 mV and 595 mV, respectively. Tafel slope of 112 mV/dec suggests a Volmer-Heyrovsky mechanism where the Volmer reaction is the rate determining step with low surface hydrogen coverage due to fast consumption of adsorbed hydrogen and fast desorption process.

Electrochemistry scans was also used to evaluate the HER performance for the NMP exfoliated MoS_2 materials at a lower catalyst loading capacity of 0.026 mg/cm² due to yield constraints. Albeit its Tafel slope of 134 mV seems respectable on the surface, but the onset potential of 465 mV and overpotential (at 10 mA/cm²) of 668 mV are on par with the unexfoliated material under the same loading capacity. The NMP organic solvent did not exfoliate the mineral MoS_2 as well as the co-solvent of 2-propanol/water. This could be attributed to contaminants contributing to a lower surface tension, which resulted in a mismatch between the solvent's surface tension and the material's surface tension. Thus resulting in poor exfoliation of mineral MoS_2. Additionally, adding trace amount (0.6 μL equivalent or 5vol%) of NMP to the 1 mL solution to be drop-casted led to negligible change in catalyst activity. In retrospect, the unexfoliated material was catalytically inert in the first place, addition of trace amount of organic solvent probably would not have made a difference to an inert material. A better choice would be to add trace amount of NMP to the co-solvent exfoliated MoS_2 nanosheets that were known to be active for hydrogen evolution reaction, and then compare the electrochemical activity.

In the co-solvent system, the benefits far outweigh the disadvantages compared to organic solvents, as both the 2-propanol and water could be easily evaporated and they do not present health hazards such as toxicity, corrosiveness or poisonous commonly associated with pyrrolidone based organic solvents. In addition, the nanosheets obtained from the co-solvent system of 2-propanol and water exhibited an increase in catalytic activity (smaller Tafel slope, smaller overpotential and smaller onset potential) which could be attributed to an increase in active edge sites. Based on the electrochemical results, a Volmer-Heyrovsky mechanism was hypothesized with the Volmer reaction as the rate determining step where surface hydrogen coverage is low due to fast consumption of adsorbed hydrogen along with a fast desorption process. However, further investigation is required to elucidate the location of the edge active sites. It would be beneficial to compare the co-solvent exfoliated MoS_2 mineral nanosheets to those that were purchased from Sigma Aldrich.

4.2   Contributions to Original Knowledge

In this study, the liquid phase exfoliation of natural molybdenite mineral into nanosheets was investigated along with a demonstration of a potential catalyst application through the cathodic reduction reaction in electrolysis of water, hydrogen evolution reaction. Previous studies have focused on the possible materials preparation methods while showing little interest in the actual electrochemical performance of the liquid phase exfoliated nanosheets. The hypothesized mechanisms were investigated and the exfoliated nanosheets' thickness were consistent with previous findings. This research provides evidence that the liquid phase exfoliated nanosheets using the co-solvent of 2-propanol/water indeed provided an increase in hydrogen evolution reaction catalysis performance compared to the unexfoliated material. In comparison with organic solvent NMP, co-solvent of 2-propanol/water was preferred for the mineral MoS_2, as the impurities may have contributed to a lower surface tension. This thus resulted in better exfoliation yield for the co-solvent versus NMP. Additionally, 2-propanol has less of an environmental impact compared to pyrrolidone-based solvents which are known to be toxic and hazardous. Most importantly, the nanosheets obtained from the co-solvent method demonstrated an increase in hydrogen evolution reaction performance. Significant amount of impurities were found in the liquid phase exfoliated nanosheets which may have been concentrated in the supernatant due to the way the samples were processed. The impurities may have contributed to lowering the surface tension of MoS_2, thus rendering NMP ineffective compared to the lower surface tension of 45vol% 2-propanol/water. Albeit the exfoliated nanosheets are on the scale of few layers and monolayer, further study is required to understand if an increase in active edge sites accounted for the increase in catalysis activity or if it is something else that is at work.

4.3   Future Work

In order to determine the factors that contributed to an increase in catalysis activity, specifically whether it is the impurities at work or the active edge sites, further study is required. One possible way to accomplish this is to exfoliate synthesized MoS_2 (i.e. chemical vapor

deposition) down to the monolayer scale using the methods presented in this thesis, followed by identical characterization techniques to determine the S/Mo ratio and catalyst activity via hydrogen evolution reaction.

The co-solvent approach is based on Young's equation, where the most stable thermodynamic interaction should occur when the solid-liquid interfacial energy is minimized. Instead of taking the 30 wt% 2-propanol in water as given, contact angle measurements should be conducted to determine the optimal 2-propanol to water ratio as natural molybdenite was used in the experiments versus synthesized ones. Additionally, this will result in an increase in overall yield with a possibility of increase in monolayer yield as well. With that said, the entire process should be optimized in the future to decrease the concentration of impurities and increase monolayer yield. One suggested method to remove the impurities in an economical manner is to dissolve the natural molybdenite in water while stirring, followed by collection and removal of the top layer. Take the remaining solution as it is, then lyophilize the solution to remove the water, thus leaving behind the dried molybdenite for further processing.

As transition metal dichalcogenides (TMDs) have similar properties (i.e. the bulk material consists of monolayers bounded together through Van der Waals interaction), it is possible to exfoliate graphite into graphene within the same co-solvent solution or organic solvents. Simultaneous exfoliation of graphene and alike TMDs to create a hybrid material could be achieved with possibility of functionalization of graphene with TMDs or vice versa.

Layered molybdenum disulfide on the nanometer scale differs from the bulk material primarily due to the band gap transition from indirect value of ~1.23 eV to direct with a value of ~1.8 eV[21]. This is beneficial to photocatalysis as an energy level 1.8 eV corresponds to 690 nm wavelength, which is just within the visible spectrum. In addition to the known synergistic effect between molybdenum disulfide and photocatalysts such as titanium dioxide, heterogeneous photocatalysis using molybdenum disulfide as a co-catalyst or modification via positive or

negative doping could be beneficial in order to shift the absorption spectrum into the visible light region. Molybdenum disulfide is not used by itself due to poor stability of the molecular material in acid reduction conditions[99].

Additional electrochemical experiments such as cyclic voltammetry, chronoamperometry need to be performed to elucidate the kinetics, diffusion processes as polarization curves by itself could not provide a conclusive answer to the exact mechanism.

The stabilization of nanosheets against re-aggregation by the organic solvent is a double-edged sword. It was very hard to perform proper characterization of the sample since it is suspended in organic solvent. Organic solvents typically have high boiling points, which makes it very hard to remove without potentially damaging the material. Rotary evaporator is the only known method to be able to effectively evaporate off the organic solvents. However, there will be some degree of residual solvent left over even after processing the sample through the rotary evaporator. The residual solvent may or may not have a significant effect depending on the application. In addition, removal or substitution of organic solvents will most likely result in the collapse of the nanosheets structure. Washing of nanosheets to remove the organic solvent typically resulted in re-aggregation. Thus, a challenge remains in preserving the nanosheets structure while extracting the nanosheets from organic solvents or any solvent for that matter.

Bibliography

(1) Crabtree, G. W.; Dresselhaus, M. S.; Buchanan, M. V. The Hydrogen Economy. *Phys. Today* **2004**, *57* (12), 39–44.

(2) CHAPTER 7 - PHOTOELECTROCHEMICAL HYDROGEN PRODUCTION. In *Solar-Hydrogen Energy Systems*; Ohta, T., Ed.; Pergamon, 1979; pp 137–169.

(3) Köse, H.; Ciniviz, M. An Experimental Investigation of Effect on Diesel Engine Performance and Exhaust Emissions of Addition at Dual Fuel Mode of Hydrogen. *Fuel Process. Technol.* **2013**, *114*, 26–34.

(4) Züttel, A.; Remhof, A.; Borgschulte, A.; Friedrichs, O. Hydrogen: The Future Energy Carrier. *Philos. Trans. R. Soc. Lond. Math. Phys. Eng. Sci.* **2010**, *368* (1923), 3329–3342.

(5) Li, Z.; Cai, N.; Yang, J. Continuous Production of Hydrogen from Sorption-Enhanced Steam Methane Reforming in Two Parallel Fixed-Bed Reactors Operated in a Cyclic Manner. *Ind. Eng. Chem. Res.* **2006**, *45* (26), 8788–8793.

(6) Chung, D. Y.; Kim, H.; Chung, Y.-H.; Lee, M. J.; Yoo, S. J.; Bokare, A. D.; Choi, W.; Sung, Y.-E. Inhibition of CO Poisoning on Pt Catalyst Coupled with the Reduction of Toxic Hexavalent Chromium in a Dual-Functional Fuel Cell. *Sci. Rep.* **2014**, *4*, 7450.

(7) Colmenares, J. C.; Luque, R. Heterogeneous Photocatalytic Nanomaterials: Prospects and Challenges in Selective Transformations of Biomass-Derived Compounds. *Chem Soc Rev* **2014**, *43* (3), 765–778.

(8) Walter, M. G.; Warren, E. L.; McKone, J. R.; Boettcher, S. W.; Mi, Q.; Santori, E. A.; Lewis, N. S. Solar Water Splitting Cells. *Chem. Rev.* **2010**, *110* (11), 6446–6473.

(9) Suen, N.-T.; Hung, S.-F.; Quan, Q.; Zhang, N.; Xu, Y.-J.; Chen, H. M. Electrocatalysis for the Oxygen Evolution Reaction: Recent Development and Future Perspectives. *Chem. Soc. Rev.* **2017**, *46* (2), 337–365.

(10) McCrory, C. C. L.; Jung, S.; Ferrer, I. M.; Chatman, S. M.; Peters, J. C.; Jaramillo, T. F. Benchmarking Hydrogen Evolving Reaction and Oxygen Evolving Reaction Electrocatalysts for Solar Water Splitting Devices. *J. Am. Chem. Soc.* **2015**, *137* (13), 4347−4357.

(11) de Chialvo, M. R. G.; Chialvo, A. C. Hydrogen Evolution Reaction: Analysis of the Volmer-Heyrovsky-Tafel Mechanism with a Generalized Adsorption Model. *J. Electroanal. Chem.* **1994**, *372* (1), 209−223.

(12) Parsons, R. Volcano Curves in Electrochemistry. In *Catalysis in Electrochemistry*; Santos, E., Schmickler, W., Eds.; John Wiley & Sons, Inc., 2011; pp 1−15.

(13) Benck, J. D.; Hellstern, T. R.; Kibsgaard, J.; Chakthranont, P.; Jaramillo, T. F. Catalyzing the Hydrogen Evolution Reaction (HER) with Molybdenum Sulfide Nanomaterials. *ACS Catal.* **2014**, *4* (11), 3957−3971.

(14) Tang, Q.; Jiang, D. Mechanism of Hydrogen Evolution Reaction on 1T-MoS2 from First Principles. *ACS Catal.* **2016**, *6* (8), 4953−4961.

(15) Shinagawa, T.; Garcia-Esparza, A. T.; Takanabe, K. Insight on Tafel Slopes from a Microkinetic Analysis of Aqueous Electrocatalysis for Energy Conversion. *Sci. Rep.* **2015**, *5*, 13801.

(16) Salvadori, M. C.; Teixeira, F. S.; Cattani, M.; Brown, I. G. Electrical Conductivity of Platinum-Implanted Polymethylmethacrylate Nanocomposite. *J. Appl. Phys.* **2011**, *110* (11), 114905.

(17) El Beqqali, O.; Zorkani, I.; Rogemond, F.; Chermette, H.; Chaabane, R. B.; Gamoudi, M.; Guillaud, G. Electrical Properties of Molybdenum Disulfide MoS2. Experimental Study and Density Functional Calculation Results. *Synth. Met.* **1997**, *90* (3), 165−172.

(18) Shi, Y.; Wang, J.; Wang, C.; Zhai, T.-T.; Bao, W.-J.; Xu, J.-J.; Xia, X.-H.; Chen, H.-Y. Hot Electron of Au Nanorods Activates the Electrocatalysis of Hydrogen Evolution on MoS2 Nanosheets. *J. Am. Chem. Soc.* **2015**, *137* (23), 7365−7370.

(19) Winer, W. O. Molybdenum Disulfide as a Lubricant: A Review of the Fundamental Knowledge. *Wear* **1967**, *10* (6), 422−452.

(20) Kumar, N.; Seminario, J. M. Computational Chemistry Analysis of Hydrodesulfurization Reactions Catalyzed by Molybdenum Disulfide Nanoparticles. *J. Phys. Chem. C* **2015**, *119* (52), 29157–29170.

(21) Li, X.; Zhu, H. Two-Dimensional MoS2: Properties, Preparation, and Applications. *J. Materiomics* **2015**, *1* (1), 33–44.

(22) Voiry, D.; Salehi, M.; Silva, R.; Fujita, T.; Chen, M.; Asefa, T.; Shenoy, V. B.; Eda, G.; Chhowalla, M. Conducting MoS2 Nanosheets as Catalysts for Hydrogen Evolution Reaction. *Nano Lett.* **2013**, *13* (12), 6222–6227.

(23) Huang, H.; Chen, L.; Liu, C.; Liu, X.; Fang, S.; Liu, W.; Liu, Y. Hierarchically Nanostructured MoS2 with Rich In-Plane Edges as a High-Performance Electrocatalyst for Hydrogen Evolution Reaction. *J. Mater. Chem. A* **2016**, *4* (38), 14577–14585.

(24) Li, G.; Zhang, D.; Qiao, Q.; Yu, Y.; Peterson, D.; Zafar, A.; Kumar, R.; Curtarolo, S.; Hunte, F.; Shannon, S.; et al. All The Catalytic Active Sites of MoS2 for Hydrogen Evolution. *J. Am. Chem. Soc.* **2016**, *138* (51), 16632–16638.

(25) Miao, H.; Hu, X.; Sun, Q.; Hao, Y.; Wu, H.; Zhang, D.; Bai, J.; Liu, E.; Fan, J.; Hou, X. Hydrothermal Synthesis of MoS2 Nanosheets Films: Microstructure and Formation Mechanism Research. *Mater. Lett.* **2016**, *166*, 121–124.

(26) Li, H.; Wu, J.; Yin, Z.; Zhang, H. Preparation and Applications of Mechanically Exfoliated Single-Layer and Multilayer MoS2 and WSe2 Nanosheets. *Acc. Chem. Res.* **2014**, *47* (4), 1067–1075.

(27) Sun, J.; Li, X.; Guo, W.; Zhao, M.; Fan, X.; Dong, Y.; Xu, C.; Deng, J.; Fu, Y. Synthesis Methods of Two-Dimensional MoS2: A Brief Review. *Crystals* **2017**, *7* (7), 198.

(28) Zhao, Y.; Zhang, Y.; Yang, Z.; Yan, Y.; Sun, K. Synthesis of MoS 2 and MoO 2 for Their Applications in H 2 Generation and Lithium Ion Batteries: A Review. *Sci. Technol. Adv. Mater.* **2013**, *14* (4), 43501.

(29) Coleman, J. N.; Lotya, M.; O'Neill, A.; Bergin, S. D.; King, P. J.; Khan, U.; Young, K.; Gaucher, A.; De, S.; Smith, R. J.; et al. Two-Dimensional Nanosheets Produced by Liquid Exfoliation of Layered Materials. *Science* **2011**, *331* (6017), 568–571.

(30) Lukowski, M. A.; Daniel, A. S.; Meng, F.; Forticaux, A.; Li, L.; Jin, S. Enhanced Hydrogen Evolution Catalysis from Chemically Exfoliated Metallic MoS2 Nanosheets. *J. Am. Chem. Soc.* **2013**, *135* (28), 10274–10277.

(31) Geng, X.; Sun, W.; Wu, W.; Chen, B.; Al-Hilo, A.; Benamara, M.; Zhu, H.; Watanabe, F.; Cui, J.; Chen, T. Pure and Stable Metallic Phase Molybdenum Disulfide Nanosheets for Hydrogen Evolution Reaction. *Nat. Commun.* **2016**, *7*, 10672.

(32) Seo, B.; Joo, S. H. Recent Advances in Unveiling Active Sites in Molybdenum Sulfide-Based Electrocatalysts for the Hydrogen Evolution Reaction. *Nano Converg.* **2017**, *4*, 19.

(33) Tributsch, H.; Bennett, J. C. Electrochemistry and Photochemistry of MoS2 Layer Crystals. I. *J. Electroanal. Chem. Interfacial Electrochem.* **1977**, *81* (1), 97–111.

(34) Laursen, A. B.; Kegnæs, S.; Dahl, S.; Chorkendorff, I. Molybdenum Sulfides—efficient and Viable Materials for Electro - and Photoelectrocatalytic Hydrogen Evolution. *Energy Environ. Sci.* **2012**, *5* (2), 5577–5591.

(35) Shi, S.; Gao, D.; Xia, B.; Liu, P.; Xue, D. Enhanced Hydrogen Evolution Catalysis in MoS2 Nanosheets by Incorporation of a Metal Phase. *J. Mater. Chem. A* **2015**, *3* (48), 24414–24421.

(36) Liu, D.; Xu, W.; Liu, Q.; He, Q.; Haleem, Y. A.; Wang, C.; Xiang, T.; Zou, C.; Chu, W.; Zhong, J.; et al. Unsaturated-Sulfur-Rich MoS2 Nanosheets Decorated on Free-Standing SWNT Film: Synthesis, Characterization and Electrocatalytic Application. *Nano Res.* **2016**, *9* (7), 2079–2087.

(37) Nicolosi, V.; Chhowalla, M.; Kanatzidis, M. G.; Strano, M. S.; Coleman, J. N. Liquid Exfoliation of Layered Materials. *Science* **2013**, *340* (6139), 1226419.

(38) Ojha, K.; Saha, S.; Banerjee, S.; Ganguli, A. K. Efficient Electrocatalytic Hydrogen Evolution from MoS2-Functionalized Mo2N Nanostructures. *ACS Appl. Mater. Interfaces* **2017**, *9* (23), 19455–19461.

(39) Kappera, R.; Voiry, D.; Yalcin, S. E.; Branch, B.; Gupta, G.; Mohite, A. D.; Chhowalla, M. Phase-Engineered Low-Resistance Contacts for Ultrathin MoS2 Transistors. *Nat. Mater.* **2014**, *13* (12), 1128–1134.

(40) Novoselov, K. S.; Geim, A. K.; Morozov, S. V.; Jiang, D.; Zhang, Y.; Dubonos, S. V.; Grigorieva, I. V.; Firsov, A. A. Electric Field Effect in Atomically Thin Carbon Films. *Science* **2004**, *306* (5696), 666–669.

(41) Parzinger, E.; Miller, B.; Blaschke, B.; Garrido, J. A.; Ager, J. W.; Holleitner, A.; Wurstbauer, U. Photocatalytic Stability of Single- and Few-Layer MoS2. *ACS Nano* **2015**, *9* (11), 11302–11309.

(42) Xie, Y.; Wang, Z.; Zhan, Y.; Zhang, P.; Wu, R.; Jiang, T.; Wu, S.; Wang, H.; Zhao, Y.; Tang Nan; et al. Controllable Growth of Monolayer MoS 2 by Chemical Vapor Deposition via Close MoO 2 Precursor for Electrical and Optical Applications. *Nanotechnology* **2017**, *28* (8), 84001.

(43) Bergeron, H.; Sangwan, V. K.; McMorrow, J. J.; Campbell, G. P.; Balla, I.; Liu, X.; Bedzyk, M. J.; Marks, T. J.; Hersam, M. C. Chemical Vapor Deposition of Monolayer MoS2 Directly on Ultrathin Al2O3 for Low-Power Electronics. *Appl. Phys. Lett.* **2017**, *110* (5), 53101.

(44) Zhang, W.; Zhang, P.; Su, Z.; Wei, G. Synthesis and Sensor Applications of MoS2-Based Nanocomposites. *Nanoscale* **2015**, *7* (44), 18364–18378.

(45) Hernandez, Y.; Nicolosi, V.; Lotya, M.; Blighe, F. M.; Sun, Z.; De, S.; McGovern, I. T.; Holland, B.; Byrne, M.; Gun'Ko, Y. K.; et al. High-Yield Production of Graphene by Liquid-Phase Exfoliation of Graphite. *Nat. Nanotechnol.* **2008**, *3* (9), 563–568.

(46) Mukhopadhyay, T. K.; Datta, A. Deciphering the Role of Solvents in the Liquid Phase Exfoliation of Hexagonal Boron Nitride: A Molecular Dynamics Simulation Study. *J. Phys. Chem. C* **2017**, *121* (1), 811–822.

(47) Shen, J.; He, Y.; Wu, J.; Gao, C.; Keyshar, K.; Zhang, X.; Yang, Y.; Ye, M.; Vajtai, R.; Lou, J.; et al. Liquid Phase Exfoliation of Two-Dimensional Materials by Directly Probing and Matching Surface Tension Components. *Nano Lett.* **2015**, *15* (8), 5449–5454.

(48) Yu, Y.; Huang, S.-Y.; Li, Y.; Steinmann, S. N.; Yang, W.; Cao, L. Layer-Dependent Electrocatalysis of MoS2 for Hydrogen Evolution. *Nano Lett.* **2014**, *14* (2), 553–558.

(49) Halim, U.; Zheng, C. R.; Chen, Y.; Lin, Z.; Jiang, S.; Cheng, R.; Huang, Y.; Duan, X. A Rational Design of Cosolvent Exfoliation of Layered Materials by Directly Probing Liquid–solid Interaction. *Nat. Commun.* **2013**, *4*, 2213.

(50) Chen, X.; Boulos, R. A.; Eggers, P. K.; Raston, C. L. P-Phosphonic Acid calix[8]arene Assisted Exfoliation and Stabilization of 2D Materials in Water. *Chem. Commun.* **2012**, *48* (93), 11407–11409.

(51) Gaur, A. P. S.; Sahoo, S.; Ahmadi, M.; Dash, S. P.; Guinel, M. J.-F.; Katiyar, R. S. Surface Energy Engineering for Tunable Wettability through Controlled Synthesis of MoS2. *Nano Lett.* **2014**, *14* (8), 4314–4321.

(52) Wang, S.; Zhang, Y.; Abidi, N.; Cabrales, L. Wettability and Surface Free Energy of Graphene Films. *Langmuir* **2009**, *25* (18), 11078–11081.

(53) Bang, G. S.; Nam, K. W.; Kim, J. Y.; Shin, J.; Choi, J. W.; Choi, S.-Y. Effective Liquid-Phase Exfoliation and Sodium Ion Battery Application of MoS2 Nanosheets. *ACS Appl. Mater. Interfaces* **2014**, *6* (10), 7084–7089.

(54) Jawaid, A.; Nepal, D.; Park, K.; Jespersen, M.; Qualley, A.; Mirau, P.; Drummy, L. F.; Vaia, R. A. Mechanism for Liquid Phase Exfoliation of MoS2. *Chem. Mater.* **2016**, *28* (1), 337–348.

(55) Backes, C.; Higgins, T. M.; Kelly, A.; Boland, C.; Harvey, A.; Hanlon, D.; Coleman, J. N. Guidelines for Exfoliation, Characterization and Processing of Layered Materials Produced by Liquid Exfoliation. *Chem. Mater.* **2016**, *29* (1), 243–255.

(56) Backes, C.; Szydłowska, B. M.; Harvey, A.; Yuan, S.; Vega-Mayoral, V.; Davies, B. R.; Zhao, P.; Hanlon, D.; Santos, E. J. G.; Katsnelson, M. I.; et al. Production of Highly Monolayer Enriched Dispersions of Liquid-Exfoliated Nanosheets by Liquid Cascade Centrifugation. *ACS Nano* **2016**, *10* (1), 1589–1601.

(57) O'Neill, A.; Khan, U.; Coleman, J. N. Preparation of High Concentration Dispersions of Exfoliated MoS2 with Increased Flake Size. *Chem. Mater.* **2012**, *24* (12), 2414–2421.

(58) Sun, H.; Biedermann, L.; Bond, T. C. Color of Brown Carbon: A Model for Ultraviolet and Visible Light Absorption by Organic Carbon Aerosol. *Geophys. Res. Lett.* **2007**, *34* (17), L17813.

(59) Altavilla, C.; Sarno, M.; Ciambelli, P. A Novel Wet Chemistry Approach for the Synthesis of Hybrid 2D Free-Floating Single or Multilayer Nanosheets of MS2@oleylamine (M=Mo, W). *Chem. Mater.* **2011**, *23* (17), 3879–3885.

(60) *UV-VIS and Photoluminescence Spectroscopy for Nanomaterials Characterization*; Kumar, C., Ed.; Springer Berlin Heidelberg: Berlin, Heidelberg, 2013.

(61) Stanjek, H.; Häusler, W. Basics of X-Ray Diffraction. *Hyperfine Interact.* **2004**, *154* (1–4), 107–119.

(62) Ishikawa, K.; Ducheyne, P.; Radin, S. Determination of the Ca/P Ratio in Calcium-Deficient Hydroxyapatite Using X-Ray Diffraction Analysis. *J. Mater. Sci. Mater. Med.* **1993**, *4* (2), 165–168.

(63) Marshall, J. L. Scanning Electron Microscopy and Energy Dispersive X-Ray (SEM/EDX) Characterization of Solder Solderability and Reliability. In *Solder Joint Reliability*; Springer, Boston, MA, 1991; pp 173–224.

(64) Williams, D. B. *Transmission Electron Microscopy a Textbook for Materials Science /*, 2nd ed.; Springer,: New York ;, 2008.

(65) Johnson, D.; Hilal, N.; Bowen, W. R. Chapter 1 - Basic Principles of Atomic Force Microscopy. In *Atomic Force Microscopy in Process Engineering*; Butterworth-Heinemann: Oxford, 2009; pp 1–30.

(66) Bowen, W. R.; Hilal, N. *Atomic Force Microscopy in Process Engineering: An Introduction to AFM for Improved Processes and Products*; Butterworth-Heinemann, 2009.

(67) Binnig, G.; Quate, C. F.; Gerber, C. Atomic Force Microscope. *Phys. Rev. Lett.* **1986**, *56* (9), 930–933.

(68) Hilal, N.; Johnson, D.; Bowen, W. R.; Williams, P. M. Chapter 2 - Measurement of Particle and Surface Interactions Using Force Microscopy. In *Atomic Force Microscopy in Process Engineering*; Butterworth-Heinemann: Oxford, 2009; pp 31–80.

(69) Hilal, N.; Johnson, D. Chapter 3 - Quantification of Particle–Bubble Interactions Using Atomic Force Microscopy. In *Atomic Force Microscopy in Process Engineering*; Butterworth-Heinemann: Oxford, 2009; pp 81–105.

(70) Fleming, A. J. A Method for Reducing Piezoelectric Non-Linearity in Scanning Probe Microscope Images. In *Proceedings of the 2011 American Control Conference*; 2011; pp 2861–2866.

(71) Braga, P. C.; Ricci, D. *Atomic Force Microscopy : Biomedical Methods and Applications*; Methods in Molecular Biology; Humana Press: Totowa, N.J., 2004.

(72) Lee, Y.-H.; Zhang, X.-Q.; Zhang, W.; Chang, M.-T.; Lin, C.-T.; Chang, K.-D.; Yu, Y.-C.; Wang, J. T.-W.; Chang, C.-S.; Li, L.-J.; et al. Synthesis of Large-Area MoS2 Atomic Layers with Chemical Vapor Deposition. *Adv. Mater.* **2012**, *24* (17), 2320–2325.

(73) Zhang, H.; Ma, Y.; Wan, Y.; Rong, X.; Xie, Z.; Wang, W.; Dai, L. Measuring the Refractive Index of Highly Crystalline Monolayer MoS2 with High Confidence. *Sci. Rep.* **2015**, *5*, 8440.

(74) Lu, J.; Xiong, T.; Zhou, W.; Yang, L.; Tang, Z.; Chen, S. Metal Nickel Foam as an Efficient and Stable Electrode for Hydrogen Evolution Reaction in Acidic Electrolyte under Reasonable Overpotentials. *ACS Appl. Mater. Interfaces* **2016**, *8* (8), 5065–5069.

(75) Joensen, P.; Crozier, E. D.; Alberding, N.; Frindt, R. F. A Study of Single-Layer and Restacked MoS 2 by X-Ray Diffraction and X-Ray Absorption Spectroscopy. *J. Phys. C Solid State Phys.* **1987**, *20* (26), 4043.

(76) Dong, H.; Chen, D.; Wang, K.; Zhang, R. High-Yield Preparation and Electrochemical Properties of Few-Layer MoS2 Nanosheets by Exfoliating Natural Molybdenite Powders Directly via a Coupled Ultrasonication-Milling Process. *Nanoscale Res. Lett.* **2016**, *11* (1).

(77) Hou, D.; Zhou, W.; Liu, X.; Zhou, K.; Xie, J.; Li, G.; Chen, S. Pt nanoparticles/MoS2 Nanosheets/carbon Fibers as Efficient Catalyst for the Hydrogen Evolution Reaction. *Electrochimica Acta* **2015**, *166* (Supplement C), 26–31.

(78) Kemppainen, E.; Bodin, A.; Sebok, B.; Pedersen, T.; Seger, B.; Mei, B.; Bae, D.; K. Vesborg, P. C.; Halme, J.; Hansen, O.; et al. Scalability and Feasibility of Photoelectrochemical H 2 Evolution: The Ultimate Limit of Pt Nanoparticle as an HER Catalyst. *Energy Environ. Sci.* **2015**, *8* (10), 2991–2999.

(79) B. Laursen, A.; Kegnæs, S.; Dahl, S.; Chorkendorff, I. Molybdenum Sulfides—efficient and Viable Materials for Electro - and Photoelectrocatalytic Hydrogen Evolution. *Energy Environ. Sci.* **2012**, *5* (2), 5577–5591.

(80) Rheinländer, P. J.; Herranz, J.; Durst, J.; Gasteiger, H. A. Kinetics of the Hydrogen Oxidation/Evolution Reaction on Polycrystalline Platinum in Alkaline Electrolyte Reaction Order with Respect to Hydrogen Pressure. *J. Electrochem. Soc.* **2014**, *161* (14), F1448–F1457.

(81) Chen, W.-F.; Iyer, S.; Iyer, S.; Sasaki, K.; Wang, C.-H.; Zhu, Y.; Muckerman, J. T.; Fujita, E. Biomass-Derived Electrocatalytic Composites for Hydrogen Evolution. *Energy Environ. Sci.* **2013**, *6* (6), 1818–1826.

(82) Hinnemann, B.; Moses, P. G.; Bonde, J.; Jørgensen, K. P.; Nielsen, J. H.; Horch, S.; Chorkendorff, I.; Nørskov, J. K. Biomimetic Hydrogen Evolution: MoS2 Nanoparticles as Catalyst for Hydrogen Evolution. *J. Am. Chem. Soc.* **2005**, *127* (15), 5308–5309.

(83) Bian, X.; Zhu, J.; Liao, L.; Scanlon, M. D.; Ge, P.; Ji, C.; Girault, H. H.; Liu, B. Nanocomposite of MoS2 on Ordered Mesoporous Carbon Nanospheres: A Highly Active Catalyst for Electrochemical Hydrogen Evolution. *Electrochem. Commun.* **2012**, *22* (Supplement C), 128–132.

(84) Addou, R.; Colombo, L.; Wallace, R. M. Surface Defects on Natural MoS2. *ACS Appl. Mater. Interfaces* **2015**, *7* (22), 11921–11929.

(85) Li, H.; Zhang, Q.; Yap, C. C. R.; Tay, B. K.; Edwin, T. H. T.; Olivier, A.; Baillargeat, D. From Bulk to Monolayer MoS2: Evolution of Raman Scattering. *Adv. Funct. Mater.* **2012**, *22* (7), 1385–1390.

(86) Fernando Castro-Guerrero, C.; Leonard Deepak, F.; Ponce, A.; Cruz-Reyes, J.; Del Valle-Granados, M.; Fuentes-Moyado, S.; H. Galván, D.; José-Yacamán, M. Structure and Catalytic Properties of Hexagonal Molybdenum Disulfide Nanoplates. *Catal. Sci. Technol.* **2011**, *1* (6), 1024–1031.

(87) Gao, D.; Si, M.; Li, J.; Zhang, J.; Zhang, Z.; Yang, Z.; Xue, D. Ferromagnetism in Freestanding MoS2 Nanosheets. *Nanoscale Res. Lett.* **2013**, *8*, 129.

(88) Stokes, A. R.; Wilson, A. J. C. A Method of Calculating the Integral Breadths of Debye-Scherrer Lines. *Math. Proc. Camb. Philos. Soc.* **1942**, *38* (3), 313–322.

(89) Shen, J.; He, Y.; Wu, J.; Gao, C.; Keyshar, K.; Zhang, X.; Yang, Y.; Ye, M.; Vajtai, R.; Lou, J.; et al. Liquid Phase Exfoliation of Two-Dimensional Materials by Directly Probing and Matching Surface Tension Components. *Nano Lett.* **2015**, *15* (8), 5449–5454.

(90) Owen, T. *Fundamentals of Modern UV-Visible Spectroscopy: Primer*; Agilent Technologies, 2000.

(91) Eda, G.; Yamaguchi, H.; Voiry, D.; Fujita, T.; Chen, M.; Chhowalla, M. Photoluminescence from Chemically Exfoliated MoS2. *Nano Lett.* **2011**, *11* (12), 5111−5116.

(92) Splendiani, A.; Sun, L.; Zhang, Y.; Li, T.; Kim, J.; Chim, C.-Y.; Galli, G.; Wang, F. Emerging Photoluminescence in Monolayer MoS2. *Nano Lett.* **2010**, *10* (4), 1271−1275.

(93) Andersen, A.; Kathmann, S. M.; Lilga, M. A.; Albrecht, K. O.; Hallen, R. T.; Mei, D. First-Principles Characterization of Potassium Intercalation in Hexagonal 2H-MoS2. *J. Phys. Chem. C* **2012**, *116* (2), 1826−1832.

(94) Gopalakrishnan, D.; Damien, D.; Shaijumon, M. M. MoS2 Quantum Dot-Interspersed Exfoliated MoS2 Nanosheets. *ACS Nano* **2014**, *8* (5), 5297−5303.

(95) Li, F.; Li, J.; Cao, Z.; Lin, X.; Li, X.; Fang, Y.; An, X.; Fu, Y.; Jin, J.; Li, R. MoS2 Quantum Dot Decorated RGO: A Designed Electrocatalyst with High Active Site Density for the Hydrogen Evolution Reaction. *J. Mater. Chem. A* **2015**, *3* (43), 21772−21778.

(96) Vazquez, G.; Alvarez, E.; Navaza, J. M. Surface Tension of Alcohol Water + Water from 20 to 50 .degree.C. *J. Chem. Eng. Data* **1995**, *40* (3), 611−614.

(97) Ponce-Torres, A.; Vega, E. J. The Effects of Ambient Impurities on the Surface Tension. *EPJ Web Conf.* **2016**, *114*, 2098.

(98) Xu, Y.; Wang, L.; Liu, X.; Zhang, S.; Liu, C.; Yan, D.; Zeng, Y.; Pei, Y.; Liu, Y.; Luo, S. Monolayer MoS2 with S Vacancies from Interlayer Spacing Expanded Counterparts for Highly Efficient Electrochemical Hydrogen Production. *J. Mater. Chem. A* **2016**, *4* (42), 16524−16530.

(99) Berardi, S.; Drouet, S.; Francàs, L.; Gimbert-Suriñach, C.; Guttentag, M.; Richmond, C.; Stoll, T.; Llobet, A. Molecular Artificial Photosynthesis. *Chem. Soc. Rev.* **2014**, *43* (22), 7501−7519.